Università degli Studi di Padova

DIPARTIMENTO DI FISICA E ASTRONOMIA "GALILEO GALILEI"
Corso di Laurea Magistrale in Astronomia

Tesi di laurea magistrale

Testing Large Angle Cosmic Microwave Background Anomalies

Candidato:
Caterina Chiocchetta
Matricola 1126593

Relatore:
Dr. Michele Liguori

Correlatori:
Prof. Nicola Bartolo
Dr. Filippo Oppizzi

Anno Accademico 2017-2018

Non val saper
a chi ha fortuna contra

Contents

Sommario

La scoperta della radiazione cosmica di fondo (Cosmic Microwave Background, CMB) nel 1965 ha rivelato che la gran parte dei fotoni nell'universo fanno parte di una radiazione termica altamente isotropa ad una temperatura di circa 2.7K. Deviazioni dall'isotropia furono identificate sotto forma di un'anisotropia di dipolo dell'ordine di $10^{-3}mK$. Tale dipolo è stato interpretato come l'effetto Doppler dovuto al moto proprio del sistema solare rispetto ad un sistema di riferimento cosmologico. L'osservazione di una radiazione di fondo isotropa costituisce un argomento a favore del Principio Cosmologico, il quale afferma che l'universo è statisticamente omogeneo e isotropo e restringe la nostra attenzione alla classe di modelli cosmologici di Friedmann. In ogni caso, l'esistenza di strutture come galassie, vuoti e ammassi implica che il CMB non può essere completamente isotropo. Il primo strumento a rilevare le anisotropie in temperatura previste fu il COsmic Background Explorer che confermò come queste fossero consistenti con uno spettro scale-invariant di fluttuazioni iniziali. Negli ultimi vent'anni due nuove survey (WMAP e Planck) hanno investigato scale angolari sempre più piccole raggiungendo, nel caso di Planck, una risoluzione di 5 arcmin. Si ritiene che queste anisotropie in temperatura si siano generate da fluttuazioni quantistiche verificatesi in epoche primordiali e, in particolare, durante una fase di espansione accelerata dell'universo denominata Inflazione. L'inflazione predice un campo di fluttuazioni in temperatura: i) statisticamente isotropo, ii) gaussiano, iii) circa indipendente dalla scala spaziale. L'importanza dello studio delle anisotropie del CMB risiede nel fatto che esse permettono di vincolare i parametri cosmologici e costituiscono un test delle assunzioni del modello cosmologico utilizzato. Nell'ultimo caso comunque è importante notare che più l'assunzione è fondamentale maggiore sarà la difficoltà di testarla. In questo lavoro ci siamo concentrati su una delle evidenze sperimentali che apparentemente sembrano violare l'assunzione di isotropia statistica su grandi scale angolari. I satelliti WMAP e Planck infatti hanno rilevato la presenza di anomalie nel cielo di microonde. Con anomalie in questo caso intendiamo dei risultati nelle misure che deviano a 2 o 3 σ rispetto alle previsioni del modello

cosmologico standard. I principali esempi di queste anomalie sono: un basso valore della funzione di correlazione a due punti, allineamento di quadrupolo e ottupolo tra loro e con il moto del sistema solare, un' assimmetria emisferica nell'intensità dello spettro di potenza delle anisotropie e una grande macchia fredda nella mappa del CMB nell'emisfero meridionale (rispetto all'eclittica). Quando queste anomalie sono state rilevate si è aperto il dibattito rispetto alla loro rilevanza statistica e al loro possibile impatto sul nostro modello cosmologico. Nel nostro lavoro ci concentriamo su una di queste anomalie: il basso valore della funzione di correlazione angolare a due punti su grandi scale angolari. Vogliamo creare un test a priori per l'ipotesi che il modello cosmologico standard sia valido ma che la presenza dell'anomalia indichi che il nostro universo è una realizzazione rara di quello scenario. Per sviluppare questo test sfruttiamo la correlazione tra temperatura e polarizzazione dei fotoni del CMB che permette di fare previsioni sul comportamento della funzione di correlazione angolare a due punti tra temperatura e polarizzazione. Nel primo capitolo presentiamo gli aspetti principali del modello cosmologico standard. Nel secondo capitolo approfondiamo la fisica della CMB e l'origine delle anisotropie in temperatura che osserviamo. Illustriamo anche la correlazione tra la temperatura e la polarizzazione e gli strumenti statistici che vengono usati per studiare le anisotropie del fondo cosmico. Nel terzo capitolo presentiamo una descrizione dell'anomalia che stiamo studiando e degli stimatori statistici usati per misurarla. Descriviamo inoltre come abbiamo costruito il test delle ipotesi e i codici che abbiamo utilizzato per svilupparlo. Nell'ultimo capitolo presentiamo i nostri risultati e qualche possibile sviluppo del nostro lavoro.

Abstract

The discovery of the Cosmic Microwave Background (CMB) in the 1965 [38] revealed that most of the photons in the Universe belong to a highly isotropic thermal radiation at a temperature of $\sim 2.7K$. Deviations from isotropy were first found in the form of a temperature dipole of the order of $10^{-3}K$. This dipole has been interpreted as the effect of Doppler shift due to the proper motion of the Solar System with respect to a cosmological rest frame. The observation of an isotropic CMB provides strong support for the cosmological principle. This states that the Universe is statistically isotropic and homogeneous, and restricts our attention to the Friedmann class of cosmological models. Nevertheless the existence of structures like galaxies, voids and clusters implies that the CMB cannot be perfectly isotropic. The first to reveal the expected temperature anisotropies was the COsmic Background Explorer which confirmed that they are consistent with an almost scale-invariant power spectrum of temperature fluctuations. During the last two decades two following surveys, WMAP and Planck space missions, enabled us to investigate a large range of angular scales, reaching a resolution of 5 arcmin for Planck. These temperature fluctuations are believed to have been generated from quantum fluctuations in the very early Universe by a primordial phase of accelerated expansion called Inflation. Inflation predicts that the CMB temperature fluctuations should be: (i) statistically isotropic, (ii) Gaussian, and (iii) almost scale invariant. The importance of the study of CMB anisotropies stands in the fact that they allow both to constrain cosmological parameters and to test the underlying assumptions of a cosmological model. As regards the second aspect however we have to stress that the more fundamental is the assumption, the harder it is to test. In this work we focused on one feature in the microwave sky that apparently violate statistical isotropy on the largest angular scales. WMAP and Planck satellites indeed revealed the presence of anomalous feature in the CMB sky (a lack of correlation on the largest angular scales, alignment of the lowest multipole moments with one another and with the motion of the Solar System, an hemispherical power asymmetry or dipolar power modulation, a preference for odd parity modes

and an unexpectedly large cold spot in the Southern hemisphere). These features are anomalous at $2-3\sigma$ level with respect to the standard model and when they have been revealed the debate on their statistical relevance was open. In this work we focused on one of these anomalies: the lack of power in the two point angular correlation function on large scales. We propose an a priori test for the hypothesis that our universe is the one describe by the standard inflationary cosmological scenario and that the presence of the anomaly implies that we are a very rare realization of that cosmology. To develop the test we exploited the correlation between temperature and polarization of CMB photons that allows us to make predictions on the behaviour of the temperature - polarization two point angular correlation function. In the first chapter we present the main points of the standard cosmological scenario. In the second chapter we explore the physics of the CMB radiation formation and the origin of the anisotropies. We also illustrate the correlation between temperature and polarization and the statistical tools that are used to study CMB anisotropies. In the third chapter we present a precise description of the anomaly we are working on and the statistical estimators used to quantify it. We also describe how we built the test and the codes we used in it. In the last chapter we present our results, the predictions we can make on the future release of Planck data and some possible development of this work.

Chapter 1

The Standard Cosmological Scenario

1.1 Friedmann Lemaitre Robertson Walker model

The Standard Cosmological Scenario [15] is based on a theory of the twenties called Hot Big Bang. It assumes an isotropic and homogeneous universe starting from a very hot and dense phase and gradually expanding and cooling. This standard model is based on a fundamental assumption: the Cosmological Principle, which is an extension of the Copernican Principle stating that the Earth is not in a particular position in the space. This, together with the observed isotropy, leads to the homogeneity. The validity of this principle is confirmed only on large scales (more than 200 parsec) so we can say that the assumption of isotropy and homogeneity is a good zero order approximation. Both homogeneity and isotropy have to be interpreted from a statistical point of view and they imply that the properties of the universe are invariant under rotations and translations in space. In the standard scenario we base our theory of gravity on General Relativity. In this framework the geometric properties of space-time are described by the tensor $g_{\mu\nu}$ which allows for the measure of distance in a curved manifold. For a generic space-time with maximally symmetric spatial hypersurfaces the metric tensor assumes the form

$$g_{\mu\nu} = \begin{bmatrix} -1 & 0 & 0 & 0 \\ 0 & a^2(t) & 0 & 0 \\ 0 & 0 & a(t) & 0 \\ 0 & 0 & 0 & a(t) \end{bmatrix} \tag{1.1}$$

The line element is the one of *Freedman Robertson Walker* metric:

$$\mathbf{d}s^{\mathbf{2}} = -\mathbf{c}^{\mathbf{2}}\mathbf{d}t^{\mathbf{2}} + a^{\mathbf{2}}(\mathbf{t})\left[\frac{\mathbf{d}r^{\mathbf{2}}}{\mathbf{1}-\mathbf{kr}^{\mathbf{2}}} + \mathbf{r}^{\mathbf{2}}\left(\mathbf{d}\theta^{\mathbf{2}} + \sin^{\mathbf{2}}\theta\mathbf{d}\phi^{\mathbf{2}}\right)\right] \tag{1.2}$$

Here we adopted the signature (-,+,+,+). The factor $a(t)$ is the scale factor and it gives the measure of the expansion rate of the universe. It should be noted that it depends only on time in agreement with the symmetry of the space-like hypersurface. The scale factor is linked to the definition of the *comoving distance*. The comoving frame is a reference frame which follows the expansion of the universe, also known as Hubble flow. For this reason the coordinates and the distances in this frame are fixed while the proper distances are stretched because of expansion. In the definition of the line element we use comoving coordinates. In the FRW metric it appears also the factor k. The constant k describes the curvature of the space-like hypersurfaces. The case k = 0 corresponds to a flat space with no curvature; k = 1 corresponds to a positive curvature, or to a closed space; $k = -1$ corresponds to a negative curvature and to an open space.

With the metric we can compute the Ricci tensor $R_{\mu\nu}$ and the Ricci scalar R and then write down the right hand of Einstein equation:

$$G_{\mu\nu} = R_{\mu\nu} - \frac{1}{2}Rg_{\mu\nu} \tag{1.3}$$

The curvature is related to energy content of the universe and this requires the introduction of the *energy momentum tensor* $T_{\mu\nu}$. From the Cosmological Principle results that the universe is filled by a perfect fluid, whose energy momentum tensor is:

$$T_{\mu\nu} = \begin{bmatrix} -\rho & 0 & 0 & 0 \\ 0 & P & 0 & 0 \\ 0 & 0 & P & 0 \\ 0 & 0 & 0 & P \end{bmatrix} \tag{1.4}$$

The left hand of the field equation, which rules the geometry of space-time, is driven by the evolution of scale factor. The right side gives information about the content of energy and pressure of universe. In this scenario the energy density ρ and the pressure density P are referred to the fluid that dominates a particular cosmological era. This leads to the mention of the components of universe and to their evolution during the thermal history of universe.

To elucidate this question we need to solve for the complete field equations

$$G_{\mu\nu} = R_{\mu\nu} - \frac{1}{2}Rg_{\mu\nu} = 8\pi T_{\mu\nu} \tag{1.5}$$

These equations is non linear and complicated but the assumption to live in a universe described by the metric of FRW simplifies the equation allowing to find an analytic solution. These solutions are called *Friedmann equations*:

$$\left(\frac{\dot{a}}{a}\right)^2 = \frac{8G\pi\rho}{3} - \frac{k}{a^2} \tag{1.6}$$

$$\left(\frac{\ddot{a}}{a}\right) = -\frac{4G\pi}{3}(\rho + 3p) \tag{1.7}$$

These equations describe the dynamical evolution of the universe relating the scale factor $a(t)$ to pressure and energy density $P(t)$, $\rho(t)$. These equations allow for the building of three fundamental quantities:

$$H(t) \equiv \left(\frac{\dot{a}}{a}\right) \tag{1.8}$$

This is the *Hubble expansion rate*. It measures how rapidly the scale factor changes. The other two quantities are linked to each other:

$$\rho_c = \frac{3H^2}{8G\pi} \tag{1.9}$$

It is the *critical density*, that defines the energy content of the universe in the case in which it is spatially flat. And then:

$$\Omega = \frac{\rho}{\rho_c} \tag{1.10}$$

$$\Omega - 1 = \frac{k}{H^2 a^2} \tag{1.11}$$

where Ω is the *density parameter* which establishes the relation between energy content and curvature. The most significant cases are three:

$$k = -1 \Leftrightarrow \Omega < 1 \Leftrightarrow \rho < \rho_c \quad \text{(Open)} \tag{1.12}$$

$$k = 0 \Leftrightarrow \Omega = 1 \Leftrightarrow \rho = \rho_c \quad \text{(Flat)} \tag{1.13}$$

$$k = 1 \Leftrightarrow \Omega > 1 \Leftrightarrow \rho > \rho_c \quad \text{(Close)} \tag{1.14}$$

Focusing on the right term of (1.5), from the Bianchi identity $\nabla_\mu T^\mu_\nu$ we derive the Continuity equation:

$$\dot{\rho} = -3H\,(\rho + p) \tag{1.15}$$

The continuity equation and the two Friedmann equations are not independent so we have at the end only two equations and three unknowns parameter $a(t)$, $P(t)$, $\rho(t)$. We need to add a new constrain which is the *equation of state* of the fluid. As already mentioned we consider the case of a perfect fluid in which long range forces are absent. For this fluid the equation of state is a very simple and linear one:

$$\rho = \omega p \tag{1.16}$$

Combining the equation of state with the continuity equation we can find the law of the evolution of the energy density in terms of scale factor.

$$\rho \propto a^{-3(\omega+1)} \tag{1.17}$$

This relation is valid simultaneously for all the component present in the universe on the condition of changing the value of ω. The three main component of universe can be summed up as follows:

- non relativistic matter: is composed by baryonic matter and dark matter. This matter is pressureless, which means that its pressure is negligible with respect to its energy $K_B T \ll mc^2$. In particular dark matter interacts only gravitationally with the other components. The equation of state of this component requires a $\omega = 0$. This means that $\rho \propto a^{-3}$ while $a \propto t^{\frac{2}{3}}$

- relativistic matter: it is radiation, composed by photons and relativistic neutrinos which exert a non negligible pressure. The equation of state for relativistic matter in thermal equilibrium is $\rho = \frac{1}{3}p$. From this descends the two relations $\rho \propto a^{-4}$ and $a \propto t^{\frac{1}{2}}$

- dark energy : it is the responsible of the accelerated expansion of the Universe on large scales. It is interpreted in the standard cosmological framework as a cosmological constant, but there is also the possibility of a dynamical solution of the problem passing through modifications of General Relativity. The equation of state of this component requires $\omega = -1$. In this case : $a \propto \exp(Ht)$ and $\rho = const$

These three fluids dominated the energy density of the universe in different epochs, according to their evolution law as shown in figure 1.1.
Using these results we can write an expression of the Hubble parameter as function of the cosmological density parameter of the three components. This equation is important because it shows explicitly the relation between the density parameter and the expansion rate of the universe.

$$H^2 = \left(\Omega_{rad}^{(0)} a^{-4} + \Omega_m^{(0)} a^{-3} + \left(1 - \Omega^{(0)}\right) a^{-2} + \Omega_\Lambda^{(0)}\right) \tag{1.18}$$

$$\Omega^{(0)} = \Omega_{rad}^{(0)} + \Omega_m^{(0)} + \Omega_\Lambda^{(0)} \tag{1.19}$$

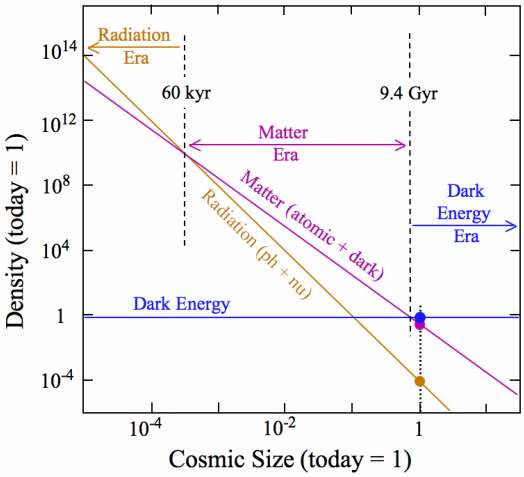

Figure 1.1: Evolution of the different components of universe with the scale factor $a(t)$

Going back with time we can see that the universe become more dense and hot, until the density diverges. This singularity is nothing more than the Big Bang. After the Big Bang the universe always expanded and, to respect the isotropy assumption, the expansion has to be adiabatic. The very high density in the primordial universe ensures that the rate of interactions between particles was higher than the expansion rate and we can assume thermal equilibrium. It is interesting to mention two of the main evidence of the Hot Big Bang Model: primordial nucleosynthesis and the Cosmic Microwave Background radiation. The first is the process responsible of the chemical abundances of the light elements in the universe. These elements (mainly Hydrogen, Helium and Lithium) formed when the expansion led the temperature to drop to $0.1 MeV$. At that time protons and neutrons glued together forming nuclei. The condition of nuclear statistical equilibrium allows us to calculate the abundances of baryons in general and of the light elements produced which are in good agreement with the observations. As regards the Cosmic Microwave Background it will be largely discussed later, for the present purpose it is enough to say that the condition of thermal equilibrium between matter and radiation allows us to predict the existence and the features of CMB.

1.2 Distance measurement in cosmology

Before going further it is important to address more in detail the issue of measurement of the distance in Cosmology. The geometry of universe, and the consequences it has on the distances we measure, is a key point in the determination of the scale on which some physical processes happened with respect to the present epoch. In 1929 Edwin Hubble observed that the nearby galaxies seemed to move away from us. He discovered a relation between the distance of a galaxy and its luminosity known as *Hubble Law*:

$$v = H_0 d \tag{1.20}$$

The distance is measured in Megaparsec (Mpc) and the velocity is a spectroscopical measure which refers to the shift of the line of emission of the sources: the *redshift*.

$$v = cz \tag{1.21}$$

$$z = \frac{\Delta\lambda}{\lambda} = \frac{\lambda_o}{\lambda_e} - 1 = \sqrt{\frac{1+\frac{v}{c}}{1-\frac{v}{c}}} \simeq \frac{v}{c} \tag{1.22}$$

The last equality is valid in the limit of non relativistic sources. H_0 is a constant only in the nearby universe because it represents the expansion rate at the present epoch.

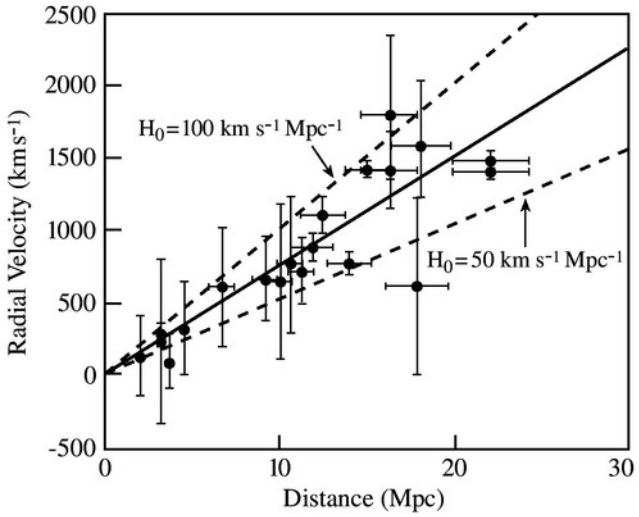

Figure 1.2: The Hubble diagram

The redshift of a light source should be interpreted as an effect of relativistic temporal dilation, which acts on the frequencies of photons traveling through an expanding space-time. Indeed it can be shown that there is a relation between redshift and the scale factor. Starting from the definition of the line element for a photon traveling from the source to the observer:

$$-c^2\mathbf{d}t^2 + a^2(\mathbf{t})\left[\frac{\mathbf{d}r^2}{\mathbf{1}-\mathbf{k}r^2}\right] = \mathbf{0} \tag{1.23}$$

with some calculation we can derive:

$$z + 1 = \frac{a\left(t_0\right)}{a\left(t\right)} \tag{1.24}$$

Redshift represents the value of the inverse of scale factor at the moment of the emission of the photon. The result of Hubble showed that our universe is not an Euclidean one. For these reason an observer should pay attention to how to measure distances. Below we sum up the main definitions of distances used in cosmology:

Comoving distance: constant in space and time, is the integral of the g_{rr} element of the metric between the comoving coordinate of the source, conventionally zero, and the observer.

$$d = \int_0^r \frac{\mathbf{d}r^2}{1-kr^2} \tag{1.25}$$

Proper distance: related to the comoving distance by the scale factor $x = a\left(t\right)d$. The proper distance is not useful because the velocity of photon is finite. For this reason we can't take simultaneous measures (with respect to comoving time) of the position of objects in the space -time but just see them along our past light cone.

Luminosity distance: important from an operationally point of view. It is directly measurable because it is based on the flux emitted by a source.

$$L = 4\pi d_L^2 F \tag{1.26}$$

where L and F are the luminosity and the flux of the source and d_L is its luminosity distance. The relation with the comoving distance $d_L = d$ is valid only if the space is a Minkowsky one. In an FRW metric in expansion the relation becomes:

$$d_L = d\left(1 + z\right) \tag{1.27}$$

Hence the relation between the flux of the source and the intrinsic luminosity is

$$F = \frac{L}{4\pi d^2 (1+z)^2} \tag{1.28}$$

the factor $(1+z)^2$ is related both to the energy reduction due to wavelength stretching of the emitted light and to the increasing time interval in photons arrival.
Using the measure of luminosity distance it is possible to infer information about the geometry of universe and the expansion rate. Indeed studies on the luminosity distance of type Ia supernovae allowed Perlmutter, Riess and Schimdt to extended the results of Hubble, showing that universe is not just expanding but this expansion is accelerating.
Supernovae type Ia represent the violent death of a withe carbon - oxygen dwarf in a binary system. The dwarf accretes mass from the companion star. This mass that settles on the surface of the dwarf cause her to overcome the mass of Chandrasekhar. It represents the limit of stability for an object supported by electron degeneracy pressure and is equal to $1.4 M_{\odot}$. This excess of mass causes a thermonuclear runaway that convert oxygen in silicon (from this the typical spectra of the supernovae Ia) and disrupt the star.
Because of this particular process of explosion that involves always the same quantity of mass, the absolute magnitude is the same (with some calibrations) for all this kind of stars and it is equal to -19.4 Mag . This, coupled with the fact that supernovae are point sources, make them excellent standard candle for the measure of distances. The observations showed substantial deviation from the condition of a matter dominated Universe, as indicated by the fact that the measured luminosities were on the average considerably fainter than what expected. See fig 1.3
This led to the conclusion that universe was dominated by an unknown component, which is the cosmological constant already mentioned.

.

Angular diameter distance: of great importance for the study of CMB. It is the ratio between the proper size of the object l and the apparent angular size from which it is seen from the Earth (θ).

$$d_A \equiv \frac{l}{\theta} \tag{1.29}$$

It is related with the quantities defined before by the relations below:

$$d_A = \frac{d_L}{(1+z^2)} = \frac{d}{(1+z)} \tag{1.30}$$

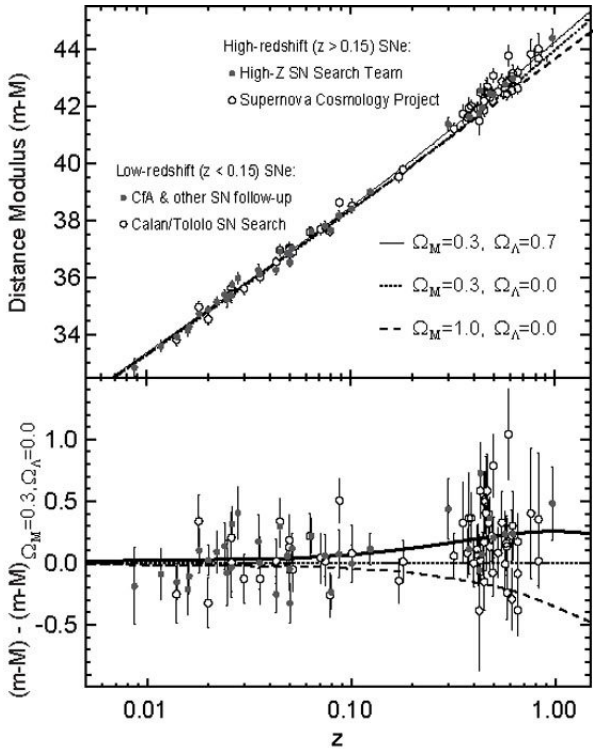

Figure 1.3: The measured distance modulus as function of redshift shows a reduction of the flux received with respect to the expectation of a constant expansion

1.3 Inflation

Inflation is a period of accelerated expansion of the universe. It is not our purpose to enter in the details of this mechanism but it is necessary to introduce it to understand the process of birth and growth of the cosmological perturbations that left their print in the Cosmic Microwave Background and in the Large Scale Structure of the Universe. First of all let's introduce the definition of horizon. There are two main types of horizons: the particle horizon and the Hubble horizon.
The *Hubble Horizon* contains all the regions that are in causal contact inside a Hubble characteristic time, calculated in equation (1.31), which is the characteristic time of expansion in a particular epoch.

$$\tau_h = \frac{1}{H(t)} \tag{1.31}$$

$$R_c = \frac{c}{H(t)} = \frac{c}{\tau(t)} \tag{1.32}$$

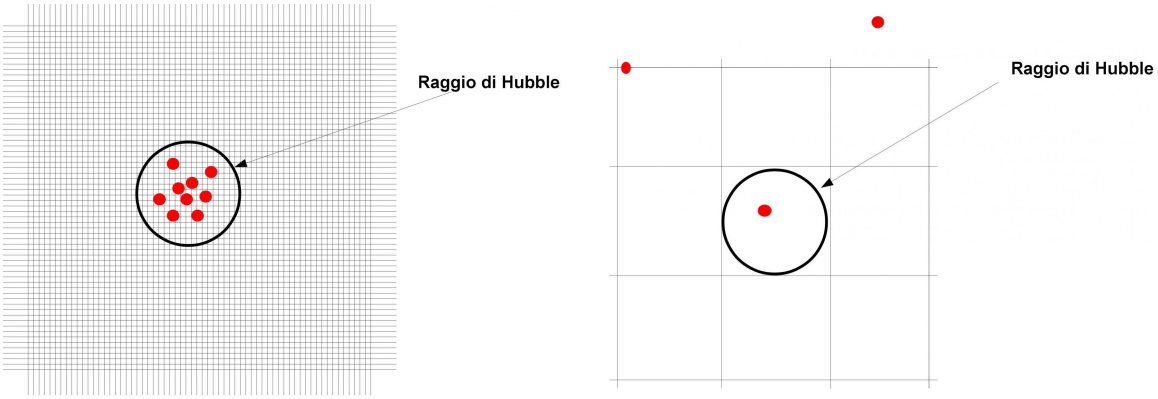

Figure 1.4: Expansion of the universe and consequent decrease of Hubble horizon

The *particle horizon* contains all the regions that have been in causal contact since the beginning of time. The comoving particle horizon is defined as:

$$d_h = \int_0^t \frac{c\mathbf{d}t}{a\left(t'\right)} \tag{1.33}$$

It is actually the integral over time of Hubble horizon and keeps into account of all the past story of the observer. The ratio between these two horizons depends from the expansion rate of Universe. Inflation started 10^{-37} second after the Big Bang and made universe expand of a factor e^{60}. While the comoving particle horizon increased enormously due to the accelerated expansion, the Hubble horizon dropped and regions which were in causal contact before inflation were ejected out of Hubble sphere as shown in figure 1.4

When inflation ended and the comoving Hubble Horizon started to grow again, gradually included regions which had come out the horizon during the accelerated expansion phase. This process is called **reentering** in the horizon of the regions of space-time. The most interesting reentering event is that of different scales of cosmological perturbations.

Observations of the Cosmic Microwave Background showed a high degree of homogeneity even on very large spatial scales, according with the Cosmological Principle. This result is difficult to explain if we consider that the information derived by CMB anisotropies (that will be extensively discuss in the next chapter) and the theory allow us to precisely fix the epoch of the formation of CMB radiation and the corresponding size of the horizon. CMB

formed 380000 years after the Big Bang when the size of the comoving Hubble Horizon today is seen under a angular scale of 2° in the sky. This opens the problem of the uniformity of CMB on scales larger than two degrees. This is called the *horizon problem*. Inflation allows to solve this problem. Within this theory, indeed, we are not observing the first entering of spatial scales in the horizon but only the re-entering, as shown in figure 1.5 . These scales have already been in causal contact before the accelerated expansion made the Hubble horizon drop. For this reason we observe a high uniformity on large scales.

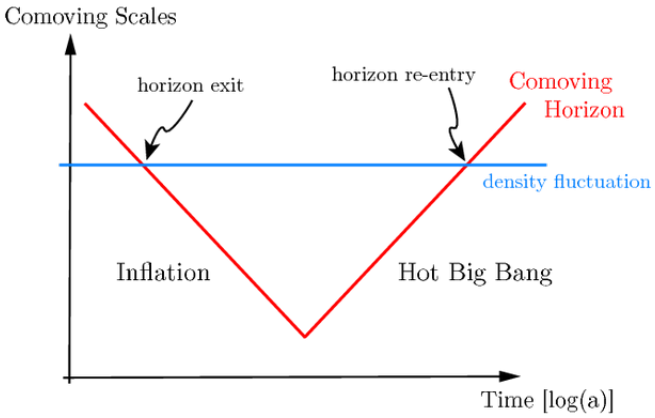

Figure 1.5: The re-entering of a particular spatial scale ejected out from the Hubble horizon during inflation

.

Another remarkable result that can be obtained studying CMB anisotropies is that the Universe has to be flat, in the sense that the total density parameter has to be approximately one. From the definition of density parameter we get:

$$\Omega(t) = \frac{\rho}{\rho_c} = \frac{8\pi G\rho}{3H^2} \tag{1.34}$$

Following the first Freedman equations (1.6) we find:

$$\Omega - 1 = \frac{k}{a^2H^2} = kR_h(t)^2 \tag{1.35}$$

This result shows that a small deviation from the flatness would led the density parameter to diverge from unity more and more in time. This constitutes a *fine tuning problem* relative to the initial conditions. Planck data fixed the current density parameter:

$$\mid 1 - \Omega\left(t_0\right) \mid < 0.005 \tag{1.36}$$

at 95% confidence level. To have this value the original density parameter should have been near 1 for a part in 10^{62}, which represents a really particular initial condition. Inflation solves this problem because it acts as an *attractor mechanism* towards the flat universe independently from the initial conditions.

To solve the flatness and horizon problems inflation has to have a minimal duration. For the horizon problem it is fixed by the largest scale observable at the present day, that must have been inside the horizon before the start of inflation. Usually the time of inflation is measured in terms of *number of e-folds*:

$$N = \ln\left(\frac{a_f}{a_i}\right) = \int_{t_i}^{t_f} H\left(t\right) \mathbf{d}t \tag{1.37}$$

where a_f and a_i are the scale factors at the end and the beginning of inflation. The second equality stands only if the acceleration is exponential, which is an assumption often used and is called *De Sitter expansion.* The minimum number of e - folds needed to solve the problems aforementioned is between 60 and 70, even if the most part of inflationary models predict a number of e-folds much more high.

The study of the candidate for driving inflation and its dynamic are very large. Here it is given a very simplified version aimed to our purpose. From the second Freedman equation it is easy to derive that to have accelerated expansion $\ddot{a}\left(t\right) > 0$ it is necessary a negative pressure

$$\ddot{a}\left(t\right) > 0 \rightarrow \left(\rho + 3P\right) < 0 \rightarrow P < -\frac{1}{3}\rho \tag{1.38}$$

because the energy density ρ has to be positive. We don't know a field with this property but we suppose it could arise at the very high energy scale of primordial universe. The simplest models of inflation assume that inflaton was a scalar field static and homogeneous with energy - momentum tensor:

$$T_{\mu\nu}^{\psi} = \partial_\mu \psi \partial_\nu \psi + \mathcal{L}_\psi g_{\mu\nu} \tag{1.39}$$

where:

$$\mathcal{L}_\psi = -\frac{1}{2} g^{\mu\nu} \partial_\mu \psi \partial_\nu \psi + V\left(\psi\right) \tag{1.40}$$

The $0 - 0$, $i - j$ components are:

$$T_0^0 = -\frac{1}{2}\dot{\psi}^2 - V(\psi) = -\rho \tag{1.41}$$

$$T_j^i = \left(\frac{1}{2}\dot{\psi}^2 - V(\psi)\right)\delta_j^i = p\delta_j^i \tag{1.42}$$

Imposing the so-called *slow-roll condition* $\frac{1}{2}\dot{\psi}^2 \ll V(\psi)$ we obtain the equation of state of the inflaton fluid that respect the condition to have a negative pressure

$$p \simeq -\rho \tag{1.43}$$

The equation of motion of the inflaton in the unperturbed background space-time is given by Klein Gordon equation in a FRW metric, in which we can neglect the spatial derivative thanks to the fact that the field is supposed to be static:

$$\ddot{\psi} + 3H\dot{\psi} - \cancel{\frac{\nabla^2\psi}{a^2}} = -V'(\psi) \tag{1.44}$$

Such primordial field underwent to quantistic perturbations, which are unavoidable given the Heisenberg's Uncertainty Principle. These perturbations were stochastic and this implies their distribution to be gaussian. Since they were very small with respect to the background we can treat these perturbations with linear theory. The field takes the form:

$$\psi(x,t) = \psi(t) + \delta\psi(x,t) \tag{1.45}$$

The zeroth order part is responsible for the accelerated expansion, while the first order part induces perturbations on the metric. The question is how perturbations evolve from quantistic oscillations to cosmological perturbation. The dynamic of perturbations follows again the Klein Gordon equation, where we assume for simplicity a massless field ($V'' = \frac{\partial V^2}{\partial^2\psi} = 0$).

$$\ddot{\delta\psi}(x,t) + 3H\dot{\delta\psi}(x,t) - \frac{\nabla^2\delta\psi}{a^2} = 0 \tag{1.46}$$

Moving to harmonic space the equation becomes:

$$\ddot{\delta\psi}_k + 3H\dot{\delta\psi}_k + \frac{k^2\delta\psi}{a^2} = 0 \tag{1.47}$$

To study the evolution of the perturbation two main cases can be distinguished: the perturbations on scales smaller than the Horizon and the perturbations on scales larger than the horizon.

- *sub-horizon scales*: scale of the perturbation $\lambda \ll H^{-1} \rightarrow \frac{k}{aH} \gg 1$. The equation is reduced to:

$$\ddot{\delta\psi}_k + 3H\dot{\delta\psi}_k \simeq 0 \tag{1.48}$$

  The solution is an harmonic oscillator with an amplitude decreasing with time. It implies that the perturbation will decay over time.

- *super-horizon scales*: scale of the perturbation $\lambda \gg H^{-1} \rightarrow \frac{k}{aH} \ll 1$. The equation is reduced to:

$$\ddot{\delta\psi}_k - \frac{k^2\delta\psi}{a^2} \simeq 0 \tag{1.49}$$

  This equation (assuming constant H) has two solutions: a decreasing one and a constant one. This means that outside the horizon the perturbations freeze, because the micro-physics can't act and dump it, and preserve the primordial features until the re-entering of the horizon.

The remaining question is how the perturbations of the inflaton are related the features we see now in CMB and in the Large Scale Structure of the Universe. Perturbations in the inflaton field are strictly bound to perturbation in the metric and in the expansion rate. Indeed fluctuations cause variations in the expansion rate in different regions of universe on large scales. In particular the temporal shift can be written as:

$$\delta t = \frac{-\delta\psi}{\dot{\psi}} \tag{1.50}$$

This temporal shift is reflected in fluctuations of the number of e-folds:

$$\delta N = H\delta t = -H\frac{\delta\psi}{\dot{\psi}} \tag{1.51}$$

Now define Z, which is a Gauge invariant [1] quantity called *curvature perturbation on uniform energy density surface*

$$Z = -\Phi \ + \delta N \tag{1.52}$$

[1] A gauge transformation is not a simple change of coordinates. In cosmology a gauge is a map that links points of the background space-time and of the perturbed space-time. It is necessary because it is impossible to compare a tensor before and after perturbation cause they refer to different space-time, unless choosing a one-to-one relationship between the two spaces. A gauge transformation is a change of map that keeps fixed the coordinates in the background space-time.

where Φ is the scalar perturbation of the spatial component of the metric. The factor Φ can be put equal to zero with a proper choice of gauge (*spatial flat gauge*) and what remains is:

$$Z = \delta N = -H\frac{\delta\psi}{\dot{\psi}} = -H\frac{\delta\rho}{\dot{\rho}} \tag{1.53}$$

The last equation is easily explained using the equations (1.41), combined with the Klein Gordon equation for the background (1.44) and the continuity equation (1.15):

$$\cancel{\frac{1}{2}}\cancel{\dot{\psi}^2} + V(\psi) = \rho \rightarrow \delta\rho = V^{'}\delta\psi \tag{1.54}$$

$$\cancel{\ddot{\psi}} + 3H\dot{\psi} = -V^{'} \tag{1.55}$$

$$-H\frac{\delta\rho}{\dot{\rho}} = \frac{-HV^{'}\delta\psi}{-3H\left(\rho + p\right)} = \frac{-3H^2\dot{\psi}\delta\psi}{3H\dot{\psi}^2} = -H\frac{\delta\psi}{\dot{\psi}} \tag{1.56}$$

In this way we can see how the perturbation of the inflaton field is linked to the perturbation of the energy density. The perturbation indeed is freezed at the horizon exit during inflation and at the reentering it is turned in a perturbation of density and temperature of the cosmic fluid.

$$Z|_{t_{exit}} \simeq -H\frac{\delta\psi}{\dot{\psi}} = Z|_{t_{entering}} \simeq -H\frac{\delta\rho}{\dot{\rho}} = \frac{1}{4}\frac{\delta\rho}{\rho} = \frac{\Delta T}{T} \tag{1.57}$$

where it has been used $\rho \propto a^{-4} \propto T^4$. This is a simplified model in which only the radiation fluid has been considered, but it clearly shows how the perturbations of the primordial field can leave their prints in photon and matter fluids giving rise to the features that we observe in the Large Scale Structure and in the CMB sky. While it is not our purpose to study the LSS of Universe, in the next chapter we will see the details of the *anisotropies* in Cosmic Microwave Background radiation field.

Chapter 2

Cosmic Microwave Background

Cosmic Microwave Background was theorized in the ′40 by Gamow as a consequence of a Hot Big Bang model with an expanding universe. CMB has been discovered in 1965 by Penzias and Wilson as a noise in telecommunications and from that moment its study has become fundamental for precision cosmology. Following the standard model if we go back with time universe becomes hotter and denser. In the primordial era the temperature was so high that matter was fully ionized and free electrons interacted with photons through Thomson scattering. The rate of interactions was high enough to ensure thermal equilibrium between the fluid of baryons and photons. As the universe expanded temperature dropped, protons and electrons combined forming hydrogen and the universe became transparent to radiation. From that epoch, called the *recombination era*, photon and baryons fluids decoupled and photon reached us preserving the features they had at the moment of the decoupling. Recombination happened 380000 years after the Big Bang when the cosmic fluid had a temperature of 3000 K. Due to the coupling of baryons and photons before recombination the energy distribution of the CMB photons was expected to be a black body distribution, and this is right what has been observed by the COBE spacecraft in the 90s:

$$I_\nu = \frac{2h\nu^3}{c^2}\left[\exp\left(\frac{h\nu}{k_B T}\right) - 1\right]^{-1} \tag{2.1}$$

The peak of this distribution is now in the range of the microwaves $\lambda \approx$ 2mm which, according to Wien's law imply a temperature of

$$\lambda_{peak} T = const \rightarrow T = 2.728 \pm 0.0002K \tag{2.2}$$

The energy density of the black body distribution is given by the Stephan - Boltzmann law:

$$\rho_{rad} = \int \frac{I_\nu d\nu}{h\nu} = 2 \int \frac{dp^3}{(2\pi)^3} \frac{1}{e^{\frac{p}{k_B T}} - 1} = \frac{\pi^2}{15} T^4 \tag{2.3}$$

which gives $\rho_{rad} \propto T^4$ while the continuity equation (1.15) gives $\rho_{rad} \propto a^{-4}$. We can therefore obtain the redshift of recombination:

$$T(a) = \frac{1}{a} T_0 \rightarrow T(a) = (1+z) T_0 \tag{2.4}$$

Known the temperature of CMB photons at the present epoch and at recombination we can derive the redshift of the decoupling, which is $z \simeq 1100$. Of course the decoupling process is gradual and it occurred in a range of redshift of $z_{rec} \pm 80$. But the higher temperature of the photons which decoupled before is entirely compensated by the higher redshift they suffers and consequently the CMB photons seem to arrive all from a very thin surface called *last scattering surface*. Observations of CMB sky remark its high level of homogeneity. As already mentioned, from the theory of inflation also a stochastic field of small anisotropies was predicted. It was actually observed by WMAP and Planck satellites which revealed a pattern of anisotropies of the order of tens of μK in the CMB sky.

2.1 Boltzmann equation

Before recombination the cosmic fluid was in thermal equilibrium. When the temperature dropped and the atoms started to form, the cosmic fluid momentarily came out from a condition of equilibrium. The most important tool used to study processes out of equilibrium is Boltzmann equation. It links the distribution function of a species with the collisional term, that takes into account the interactions of the species itself.

$$\hat{\mathbf{L}}(f) \equiv \frac{\mathbf{d}f}{\mathbf{d}t} = \hat{\mathbf{C}}(f) \tag{2.5}$$

Where $\hat{\mathbf{L}}$ is called Liouville operator and $\hat{\mathbf{C}}$ is the collisional term. $\mathbf{d}$ is the total derivative of the distribution function of the particles $f = f(x, v)$. In the classic theory this operator assumes the form:

$$\frac{\mathbf{d}f}{\mathbf{d}t} = \frac{\partial f}{\partial t} + \nabla_x f \frac{\partial x}{\partial t} + \nabla_v f \frac{\partial v}{\partial x} \tag{2.6}$$

In a relativistic space-time $f = f(x^\mu, p^\mu)$ with $p^\mu \equiv dx^\mu / d\lambda$. The equation assumes the form:

$$\frac{\mathbf{d}f}{\mathbf{d}t} = p^{\mu}\frac{\partial f}{\partial x^{\mu}} - \Gamma^{\mu}_{\alpha\beta}p^{\alpha}p^{\beta}\frac{\partial f}{\partial p^{\mu}} \tag{2.7}$$

where $\Gamma^{\mu}_{\alpha\beta}$ is the Christoffel symbol. This form can be simplified considering a Friedman Robertson Walker metric:

$$f\left(p^{\mu}, x^{\mu}\right) = f\left(E, |p|, \vec{p}, \vec{x}, t\right) = f\left(E, t\right) \tag{2.8}$$

In the last equality we use the relation between energy and momentum $E = \sqrt{p^2 + m^2}$. In this space-time only three Christoffel symbols differ from zero:

$$\Gamma^{0}_{jj} = \delta_{ij}\dot{a}a \tag{2.9}$$

$$\Gamma^{i}_{0j} = \Gamma^{i}_{j0} = \delta^{i}_{j}\frac{\dot{a}}{a} \tag{2.10}$$

and the Liouville operator becomes:

$$\hat{\mathbf{L}} = E\frac{\partial f}{\partial t} - \frac{\dot{a}}{a}p^2\frac{\partial f}{\partial E} \tag{2.11}$$

We need now to obtain the Liouville operator in a perturbed FRW metric. We consider the case of a slight perturbation of the metric tensor

$$\tilde{g}_{\mu\nu} = g_{\mu\nu} + h_{\mu\nu} \tag{2.12}$$

where $h_{\mu\nu} \ll g_{\mu\nu}$. Combining a general expression for a perturbed FRW metric

$$ds^2 = -\left(1 + 2\Phi\right)dt^2 + a^2(t)[\left(1 - 2\Psi\right)\delta_{ij}dx^i dx^j] \tag{2.13}$$

and the expression for the distribution of photons

$$f\left(\bar{x}, p, \bar{p}, t\right) = \left[exp\left[\frac{p}{T\left(t\right)\left[1 + \Theta(\bar{x}, p, \bar{p}, t)\right]}\right] - 1\right]^{-1} \tag{2.14}$$

we obtain the expression of Liouville operator at the first order:

$$\frac{df}{dt}\Big|_{(1)} = -p\frac{\partial f^0}{\partial p}\left[\frac{\partial\Theta}{\partial t} + \frac{\hat{p}^i}{a}\frac{\partial\Theta}{\partial x^i} - \frac{\partial\Psi}{\partial t} + \frac{\hat{p}^i}{a}\frac{\partial\Phi}{\partial x^i}\right] \tag{2.15}$$

We denoted with Θ the temperature perturbation, with Φ and Ψ the scalar perturbation respectively of the g_{00} and the g_{ij} component of the metric.

Focus now on the collisional operator $\hat{\mathbf{C}}$. Photons at last scattering surface mainly interacted through Thomson scattering:

$$\gamma(p) + e^{-}(q) \Leftrightarrow \gamma(p') + e^{-}(q') \tag{2.16}$$

The collisional operator for this interaction is:

$$\begin{aligned} \bar{\mathbf{C}}[f(p)] = \frac{(2\pi)^4}{p} \int \frac{d^3q}{(2\pi)^3 2E(q)} \int \frac{d^3q'}{(2\pi)^3 2E(q')} \\ \int \frac{d^3p'}{(2\pi)^3 2E(p')} |\mathcal{M}|^2 \delta^3(\bar{p} + \bar{q} - \bar{p'} - \bar{q'}) \\ \delta(p + E(q) - p' - E(q'))[f_e(q') f(p') - f_e(q) f(p)] \end{aligned} \tag{2.17}$$

Introducing the amplitude of Thomson scattering process

$$|\mathbf{M}|^2 = 6\pi\sigma_T m_e^2 \left(1 + \hat{p} \cdot \hat{p'}\right) \tag{2.18}$$

and, doing some calculations, the operators becomes:

$$\hat{\mathbf{C}}(f(t)) = n_e \sigma_T [\Theta_0 - \Theta(\bar{p}) + \bar{p} \cdot \bar{v}_b] \tag{2.19}$$

We have introduced the term Θ_0 which represents the *monopole* of the perturbation:

$$\Theta_0(\bar{x}, t) \equiv \frac{1}{4\pi} \int d\Omega \Theta(\bar{p}, \bar{x}, t) \tag{2.20}$$

If we introduce the conformal time η from this change of variable:

$$d\eta = \frac{dt}{a(t)} \tag{2.21}$$

and pass in Fourier space

$$\Theta(\bar{x}, \eta) = \int \frac{d^3k}{(2\pi)^3} e^{i\bar{k}\cdot\bar{x}} \tilde{\Theta}(\bar{k}, \eta) \tag{2.22}$$

we can write the equation of Boltzmann for photons in Fourier space:

$$\dot{\tilde{\Theta}} + ik\mu\tilde{\Theta} - \dot{\tilde{\Psi}} + ik\mu\tilde{\Phi} = -\dot{\tau}\left[\tilde{\Theta}_0 - \tilde{\Theta} + \mu\tilde{v}_b\right] \tag{2.23}$$

where v_b is the velocity of baryons and:

$$\mu \equiv \hat{k} \cdot \hat{p} \tag{2.24}$$

τ is the optic thickness which is defined as:

$$\tau(\eta) \equiv \int_{\eta}^{\eta_0} d\eta' n_e \sigma_T a(\eta) \tag{2.25}$$

Expression (2.23) allows us to describe the formation of anisotropies at recombination era and their evolution to the present epoch. Together with a proper definition of the *initial conditions* the formula just obtained gives a very complete description of the process of interest, even if, to avoid many calculation, we will use a simpler treatment for CMB anisotropies in the following chapters.

2.2 Anisotropies

2.2.1 Acoustic peaks

This section is dedicated to the description of the pattern of anisotropies that is produced by a perturbation in the cosmic fluid. Inflation gave rise to scale invariant perturbations which entered the expanding horizon at different epochs. The pattern of anisotropies that each of this perturbations generated entering the horizon is mainly due to its monopole an dipole, being the higher order terms negligible with respect to them. The monopole and dipole can be associated to the mean temperature and to the velocity of the perturbed fluid [25]. Consider the decomposition in Fourier space of the monopole term:

$$\Theta_{l=0,m=0}(\mathbf{x}) = \int \frac{d^3k}{(2\pi)^3} e^{i\bar{k}\cdot\bar{x}} \tilde{\Theta}\left(\bar{k},\eta\right) \tag{2.26}$$

Since perturbations are small and the treatment is linear, different Fourier modes evolve independently. Therefore instead of partial differential equations for the field $\Theta(\mathbf{x})$, we have ordinary differential equations in $\Theta(\mathbf{k})$. Indeed due to rotational symmetry, all $\Theta(\mathbf{k})$ for a given k follow the same equations.
From the *continuity equation* in Fourier space we have:

$$\dot{\Theta} = -\frac{1}{3} k v_\gamma \tag{2.27}$$

where v_γ is the dipole of the perturbation. It has been written as a scalar instead of a vector. This because the only important component of velocity is that parallel to the wavevector $\mathbf{k}$ so v_γ represents a dipole moment directed along $\mathbf{k}$. The factor $1/3$ derives from the fact that continuity equation conserves the number density of photons and not temperature and $n_\gamma \propto T^3$.

The *Euler equation* for the photon fluid is the expression of momentum conservation. The momentum density of the photon is $(\rho_\gamma + p_\gamma)\, v_\gamma$. Standing the equation of state for photons $p_\gamma = \rho_\gamma/3$ and $\rho_\gamma \propto T^4$, the pressure gradient $\nabla p_\gamma = \nabla \rho_\gamma/3$ becomes $k\Theta\rho_\gamma/3$ in Fourier space. The Euler equation becomes:

$$\dot{v}_\gamma = k\Theta \tag{2.28}$$

Differentiating the continuity equation ad inserting the Euler equation we obtain:

$$\ddot{\Theta} + c_s^2 k^2 \Theta = 0 \tag{2.29}$$

where $c_s \equiv \sqrt{\frac{\dot{p}}{\dot{\rho}}} = \frac{1}{\sqrt{3}}$ is the *sound speed* in the fluid. The physical interpretation of this phenomena is that in the approximation of a perfect fluid the pressure of photons acts as restoring force on the perturbation making it to oscillate at the speed of sound. These temperature oscillations represents the heating and the cooling of a fluid compressed and rarefied by an acoustic wave. Until recombination all the perturbation scales that reentered the horizon where subjected to these oscillations. At the epoch of decouplig the solution of the (2.29) is

$$\Theta(\eta_*) = \Theta(0)\cos(k s_*) \tag{2.30}$$

where s is the sound horizon and the $*$ denotes the recombination epoch. The scales of perturbations larger than the horizon at the recombination didn't undergo to this process and are frozen into their initial conditions.

2.2.2 Initial conditions and gravitational forcing

The aim of this chapter is to describe the initial condition that we observe on large scales. As already said inflation gave rise to a stochastic field of scale invariant perturbations. Those fluctuations perturbed the metric. In particular the $0-0$ and the $i-j$ components of perturbations are:

$$\delta g_{tt} = 2\Phi \tag{2.31}$$

$$\delta g_{ij} = 2a^2 \Psi \delta_{ij} \tag{2.32}$$

The perturbation of the zero component of the metric is hence a temporal shift:

$$\frac{\delta t}{t} = \Phi \tag{2.33}$$

considering a radiation dominated era $a \propto t^{2/3\left(1+\frac{p}{\rho}\right)}$ the change in photons temperature is:

$$\Theta = -\frac{\delta a}{a} = -\frac{2}{3}\left(1+\frac{p}{\rho}\right)^{-1}\frac{\delta t}{t} \tag{2.34}$$

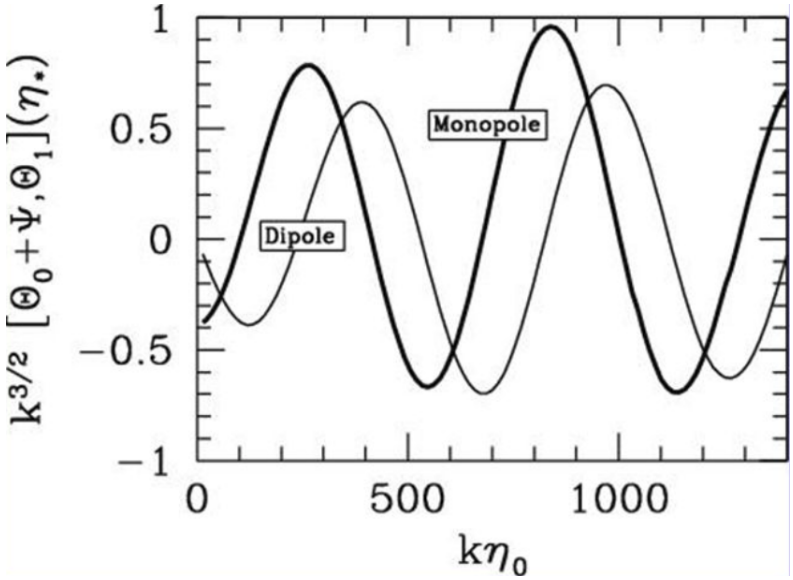

Figure 2.1: Acoustic oscillation of monopole and dipole. As seen by deriving both side of equation (2.30) the two multipoles are in opposition of phase one with the other

Thus a metric perturbation produces a temperature fluctuation of $-\frac{\Phi}{2}$ in radiation dominated era $\left(p=\frac{\rho}{3}\right)$ and of $-\frac{2\Phi}{3}$ in matter dominated epoch $(p=0)$ Perturbations in the metric and gravitational potential alter the acoustic oscillations by providing a gravitational force on the oscillator. The oscillations under gravity become a competition between pressure gradient $k\Theta$ and potential gradient $k\Psi$ with an equilibrium when $\Theta+\Psi=0$. Continuity and Euler equations become:

$$\dot{\Theta}=-\frac{1}{3}kv_\gamma-\dot{\Psi} \tag{2.35}$$

$$\dot{v}=k\left(\Theta+\Phi\right) \tag{2.36}$$

The $\dot{\Psi}$ in continuity equation is due to the fact that curvature fluctuations generate a perturbation of the scale factor that produces a temperature perturbation in analogy to cosmological redshift $\delta\Theta=-\delta\Phi$. Equation (2.29) assumes the form:

$$\ddot{\Theta}+c_s^2k^2\Theta=-\frac{k^2}{3}\Phi-\ddot{\Psi} \tag{2.37}$$

where Φ and Ψ are constant in a flat universe. Equation (2.37) is identical to (2.29) with Θ replaced with $\Theta+\Phi$.The solution of the equation is:

$$\left[\Theta+\Phi\right](\eta)=\left[\Theta+\Phi\right](\eta_{md})\cos\left(ks\right) \tag{2.38}$$

where η_{md} stands for the conformal time of matter dominated era. Indeed gravitational perturbations acquire importance when matter starts to dominate on radiation after the equivalence epoch. The quantity $[\Theta + \Phi]$ can be thought as an *effective temperature*: after recombination photons must climb the potential wells to the observer and suffer a gravitational redshift $\frac{\Delta T}{T} = \Psi$. The effective temperature fluctuation is therefore the observed temperature fluctuation. By inserting the initial condition in (2.37) in a matter dominated era we recover:

$$[\Theta + \Phi](\eta) = \frac{1}{3}\Psi(\eta_{md})\cos(ks) \tag{2.39}$$

The large scale limit of this equation is the *Sachs-Wolfe* result which states that observed temperature perturbation is $\Psi/3$ and overdense regions corresponds to cold spots in the sky, cause when $\Psi < 0$, although Θ is positive, the effective temperature $\Theta + \Phi$ is negative.

2.2.3 Baryon loading

Baryons' effect on acoustic peaks can be included thinking that they give an extra inertia to the potential gradient. All the terms, but the pressure gradient, in the Euler equation are multiplied by a factor $1 + R$ leading to the new equation:

$$c_s^2 \frac{d}{d\eta}\left(c_s^{-2}\dot{\Theta}\right) + c_s^2 k^2 \Theta = -\frac{k^2}{3}\Phi - c_s^2 \frac{d}{d\eta}\left(c_s^{-2}\dot{\Psi}\right) \tag{2.40}$$

Where the sound speed is reduced by the baryons to $c_s = 1/\sqrt{3(1+R)}$. Consider the limit of constant R, Φ, Ψ. The solution becomes:

$$[\Theta + (1+R)\Phi](\eta) = [\Theta + (1+R)\Phi](\eta_{md})\cos(ks) \tag{2.41}$$

where the new effective temperature is $\Theta \to [\Theta + (1+R)\Phi]$. The main effects of the baryon loading are three: the decrease of sound speed and consequently the sound horizon, the enhancement of the peaks due to extra gravitational force provided and the shift of the equilibrium point to $\Theta = -(1+R)\Phi$. Because the observed temperature is still $\Theta + \Phi$ the changing of the effective temperature breaks the symmetry enhancing only the compression i.e. only odd peaks.

2.2.4 Radiation driving

The amplitude of the acoustic peaks is dependent from the ratio of dark matter to radiation. Because the amount of radiation is known from the

measured temperature of the CMB and the thermal history, acoustic peaks are sensitive to the dark matter density in the universe. If the energy density of the radiation dominates the matter density, we can no longer consider the photon-baryon fluid to be oscillating in a fixed gravitational potential well. In fact, the potential decays away at just the right time to drive the amplitude of the oscillations up. In radiation dominated regime the photon density is also what is making the gravitational potential in the first place. As pressure stops the radiation from further compression, the density fluctuation stabilizes leaving the gravitational potential to decay with the expansion of the universe. The decay happens when the fluid is in its most compressed state. The fluid now sees no gravitational potential to fight against as it bounces back and the amplitude of the oscillations goes way up.
This driving effect does not come into play once the density of the universe is dominated by the dark matter, hence it is the small scale modes, which entered the horizon in radiation dominated epoch, that feel this driving effect.

2.2.5 Damping

Photon and baryons fluid, assumed till now a perfect fluid, has instead slight imperfections corresponding to viscosity and heat conduction. Taking into account of these effects has no consequences on the continuity equations:

$$\dot{\Theta} = -\frac{k}{3}v_\gamma - \dot{\Psi} \tag{2.42}$$

$$\dot{\delta}_b = -kv_b - 3\dot{\Phi} \tag{2.43}$$

while the Euler equations gain new terms:

$$\dot{v_\gamma} = k\left(\Theta + \Phi\right) - \frac{k}{6}\pi_\gamma - \dot{\tau}\left(v_\gamma - v_b\right) \tag{2.44}$$

$$\dot{v_b} = -\frac{\dot{a}}{a}v_b + k\Phi + \frac{\dot{\tau}}{R}\left(v_\gamma - v_b\right) \tag{2.45}$$

For the baryons the first term on the right accounts for cosmological expansion, the third term is related to Thomson scattering between photons and electrons with $\dot{\tau} \equiv n_e\sigma_T a$ (obviously the opposite of this term is present in the photon equation). In equation (2.44) π_γ is the anisotropic stress proportional to the quadrupole moment of the perturbation hence to the gradient of v_γ Viscosity and heat conduction led to a suppression of perturbations. The damping scale k_d is of the order $\sqrt{\dot{\tau}/\eta}$ the numerator corresponding to the mean free path and the denominator to the horizon. Damping can be interpreted as the result of random walk in the baryons that takes photons

from hot regions to cold one and vice-versa. Since it is related to random walk damping mainly affects small scales of perturbation which amplitudes are decreased by this process as seen in figure (2.2)

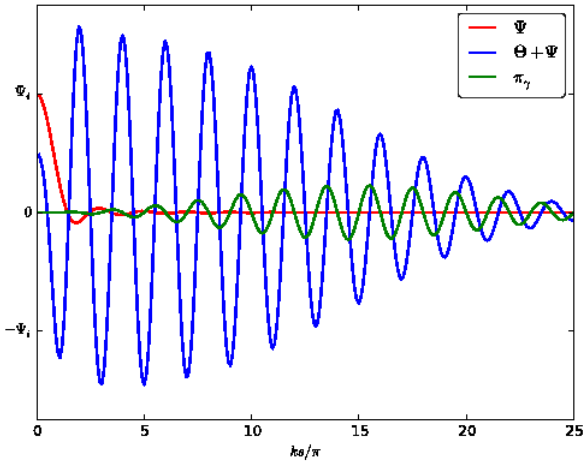

Figure 2.2: Radiation driving of acoustic oscillations and the following damping. As shown by the red line the potential decays during radiation domination. The quadropule or viscosity, which drives the damping effect is indicated with π_γ

2.2.6 Secondary anisotropies

The pattern of anisotropies described till now is referred to what happens at the last scattering surface. In this paragraph we mention effects that occur after recombination during the travel of the photon to us. These are mainly of two type: gravitational effects and scattering effects.

Integrated Sachs - Wolfe effect: it is related to the decay of the potential between the time a photon falls in a potential well and when it climbs out. It gets a boost in temperature of $\delta\Phi$ due to the differential gravitational redshift. As already mentioned since redshift $z \approx 0.3$ the equation of state and the dynamic of universe started to be dominated by the cosmological constant. The potential carried by the perturbation, which was frozen during the matter dominated era, started to decay giving rise to the ISW effect. It affects only very large scales of perturbation, those entered in the horizon at very low redshifts when the accelerated expansion became dominant. The smallest scale traverses many wavelengths during the decay and suffers

alternating red and blueshifts from crests and troughs. The result is a cancellation of contributions. The importance of this effect is related to the fact that it is a tracer for the potential decay caused by accelerated expansion and hence it allows to discriminate between different models of dark energy. To be precise we should mention the *Early Integrated Sachs - Wolfe effect*, which occurs at early epochs. It is due to the decay of the potential of perturbation caused by the pressure of radiation and concerns the modes that enter the horizon during the transition between radiation dominated and matter dominated epoch. Beyond the framework of the linear theory the potential evolves also during matter domination giving rise to the *Rees-Sciama effect*, which is negligible with respect to the linear one.

Thermal Sunyaev-Zel'dovich effect: it is caused by internal motion of the gas in dark matter halos which gives rise to Doppler shift in CMB photons. Shifts at the first order in the velocity are as photons scattered off of electrons moving in different directions, but at second order in velocity there is a residual effect. The second order effect is a net transfer of energy between the hot electron of gas and the cooler CMB. It causes a spectral distortion in the CMB because photons of the Rayleigh-Jeans side are transferred to the Wien tail. The SZ effect from clusters provides the main contribution to temperature anisotropies beyond the damping tail. The importance of SZ is related to the determination of clusters features. The net effect is of order of $n_e T_e$ hence it is a proof of the gas pressure in the cluster. Moreover SZ, combined with X-observations, allows the determination of cluster distance.

2.3 Projected anisotropies

In this section we try to match perturbations at recombination epoch to the pattern of anisotropies that we observe today. Consider a flat universe and the path of photons from the last scattering surface to us d_L:

$$ds^2 = 0 = -dt^2 + a^2 dl^2 \rightarrow dl^2 = \frac{dt^2}{a^2} \tag{2.46}$$

$$dl^2 = d\eta^2 \rightarrow d_L = \int_{\eta_*}^{\eta_0} d\eta = \eta_0 - \eta_* \tag{2.47}$$

where d_L is actually the comoving angular diameter distance defined in equation (1.29). It follows that if we consider two CMB photons, one hot and one cold, separated by a comoving distance $\lambda \sim k^{-1}$, they travel from recombi-

nation to the present epoch starting from an angular separation θ.

$$d_L\theta \sim k^{-1} \rightarrow \theta \sim \frac{k^{-1}}{\eta_0 - \eta_*} \rightarrow \theta \simeq \frac{k^{-1}}{\eta_0} \tag{2.48}$$

where the linear distance between photons is approximated with the angular distance between the two and it has been used $\eta_0 \gg \eta_*$. To better under-

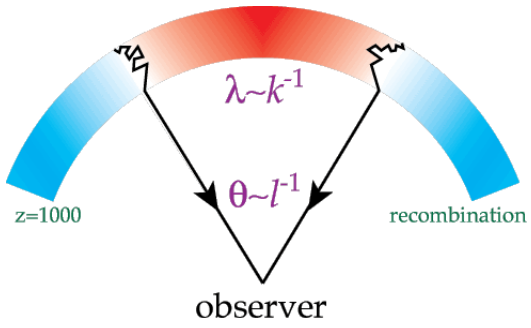

Figure 2.3: Projection of the last scattering surface anisotropies in a flat universe

stand the mechanism and define which multipoles act more to generate the anisotropies we see today let's go back to Boltzmann equation for photons (2.23) (in which we omit the tilde). Defining the source term S

$$\dot{\Theta} + (ik\mu - \dot{\tau})\Theta = e^{-ik\mu\eta+\tau(\eta)}\frac{d}{d\eta}\left[\Theta e^{+ik\mu\eta-\tau(\eta)}\right] = S \tag{2.49}$$

$$S \equiv +\dot{\Psi} - ik\mu\Phi - \dot{\tau}\left[\Theta_0 + \mu v_b\right] \tag{2.50}$$

Integrating (2.49) between an initial time (before the recombination) $\eta_{ini} \approx 0$ and today η_0 we obtain

$$\Theta\left(k,\mu,\eta_0\right)e^{ik\mu\eta_0-\tau(\eta_0)} = \Theta\left(k,\mu,\eta_i\right)e^{ik\mu\eta_i-\tau(\eta_i)} + \int_{\eta_i}^{\eta_0} d\eta S\left(k,\mu,\eta\right)e^{ik\mu(\eta)-\tau(\eta)} \tag{2.51}$$

We make the assumption that the universe is completely opaque at early epochs $\tau\left(\eta_{ini}\right) \rightarrow \infty$ while is transparent now $\tau\left(\eta_0\right) = 0$ and get:

$$\Theta\left(k,\mu,\eta_0\right) = \int_0^{\eta_0} d\eta S\left(k,\mu,\eta\right)e^{ik\mu(\eta-\eta_0)-\tau(\eta)} \tag{2.52}$$

Now we can multiply both the side for $\mathcal{P}_l/2$ and integrate on μ. On the left side we have

$$\int_{-1}^{1}\frac{d\mu}{2}\mathcal{P}_l\left(\mu\right)\Theta\left(k,\mu,\eta_0\right) = \left(-i\right)^l\Theta_l\left(k,\eta_0\right) \tag{2.53}$$

while on the right side:

$$\begin{aligned}&\int_0^{\eta_0} d\eta \int_{-1}^{1} \frac{d\mu}{2} \mathcal{P}_l(\mu)\, S(k,\mu,\eta)\, e^{ik\mu(\eta-\eta_0)-\tau(\eta)} \\ =&\int_0^{\eta_0} d\eta \int_{-1}^{1} \frac{d\mu}{2} \mathcal{P}_l(\mu)\, S\left(k, \frac{1}{ik}\frac{d}{d\eta}, \eta\right) e^{ik\mu(\eta-\eta_0)-\tau(\eta)}\end{aligned} \tag{2.54}$$

in the second line it has been use the variable change:

$$\mu \to \frac{1}{ik}\frac{d}{d\eta} \tag{2.55}$$

to suppress the μ dependence of S. The integral in η becomes:

$$\begin{aligned}&\int_0^{\eta_0} d\eta S\left(k, \frac{1}{ik}\frac{d}{d\eta}, \eta\right) e^{ik\mu(\eta-\eta_0)-\tau(\eta)} \\ \simeq&\int_0^{\eta_0} d\eta \left[\dot{\Psi} - \Phi\frac{d}{d\eta} - \dot{\tau}\left(\Theta_0 + \frac{1}{ik}\frac{d}{d\eta}v_b\right)\right] e^{ik\mu(\eta-\eta_0)-\tau(\eta)} \\ =&\int_0^{\eta_0} d\eta \left[\left(\dot{\Psi} - \dot{\tau}\Theta_0\right)e^{-\tau} + \frac{d}{d\eta}\left[e^{-\tau}\left(\Phi - \frac{iv_b\dot{\tau}}{k}\right)\right]\right] e^{ik\mu(\eta-\eta_0)} \\ =&\int_0^{\eta_0} d\eta \left[\dot{\Psi}e^{-\tau} + g(\eta)\Theta_0 + \frac{d}{d\eta}\left[e^{-\tau}\left(\Phi - \frac{iv_b\dot{\tau}}{k}\right)\right]\right] e^{ik\mu(\eta-\eta_0)} \\ =&\int_0^{\eta_0} d\eta S(k,\eta)\, e^{ik\mu(\eta-\eta_0)}\end{aligned} \tag{2.56}$$

In the last line we have introduced the visibility function

$$g(\eta) \equiv \dot{\tau} e^{-\tau} \tag{2.57}$$

which has the property:

$$\int_0^{\eta_0} d\eta g(\eta) = 1 \tag{2.58}$$

in this way $g(\eta)$ can be interpreted as the probability for a photon to have the last scatter at the conformal time η. Using the following equality:

$$\int_{-1}^{1} \frac{d\mu}{2} \mathcal{P}_l e^{ik\mu(\eta-\eta_0)} = \frac{1}{(-i)^l} j_l\left[k(\eta-\eta_0)\right] \tag{2.59}$$

where j_l is a spherical Bessel function, we can write the expression of the perturbation Θ_l:

$$\Theta_l(k,\eta_0) = (-1)^l \int_0^{\eta_0} d\eta S(k,\eta)\, j_l\left[k(\eta-\eta_0)\right] \tag{2.60}$$

To simplify the expression we do some assumptions on the visibility function. τ was very high in the epochs before recombination and the exponential $e^{-\tau}$ brought g to zero. After recombination $\dot{\tau}$ dropped suddenly bringing again the visibility function to zero. We can hence consider the visibility function as a Dirac Delta peaked on $\eta = \eta_*$. Introducing this assumption and integrating on the dirac delta we can derive a new expression for Θ_l

$$\begin{aligned}\Theta_l(k,\eta_0) \simeq [\Theta_0+\Phi](k,\eta_*)\, j_l[k(\eta_0-\eta_*)] - \frac{iv_b(\eta_*)}{k}\frac{d}{d\eta}j_l[k(\eta_0-\eta_*)] \\ + \int_0^{\eta_0} d\eta \left[\dot{\Psi}+\dot{\Phi}\right] j_l[k(\eta_0-\eta)]\end{aligned} \tag{2.61}$$

Using the relationship between baryon velocity and the dipole $v_b(\eta_*) = -3i\Theta_1(\eta_*)$ and the properties of Bessel function:

$$\frac{d}{dx}j_l(x) = j_{l-1}(x) - \frac{l+1}{x}j_l(x) \tag{2.62}$$

we obtain the important final result

$$\begin{aligned}\Theta_l(k,\eta_0) \simeq [\Theta_0+\Phi](k,\eta_*)\, j_l[k(\eta_0-\eta_*)] \\ +3\Theta_1(k,\eta_*)\left(j_{l-1}[k(\eta_0-\eta_*)] - \frac{l+1}{k(\eta_0-\eta_*)}j_l[k(\eta_0-\eta_*)]\right) \\ + \int_0^{\eta_0} d\eta \left[\dot{\Phi}+\dot{\Psi}\right] j_l[k(\eta_0-\eta)]\end{aligned} \tag{2.63}$$

This relation shows that the anisotropy we see today is due mainly to three contribution: Sachs - Wolfe, Doppler effect and Integrated Sachs - Wolfe. The first term is dominant and as we have seen in the previous section, is related to an effective temperature given by the monopole of the distribution plus a gravitational contribution. The second term is originated by the motion of the fluid at epoch of decoupling. If the regions that we observe had a positive velocity in our direction photons would have a slight higher frequency and they will seem hotter, the opposite happens in the regions in which fluid had negative velocity with respect to us. This term is subdominant compared to Sachs - Wolfe. The last term is Integrated Sachs - Wolfe and, as we already mentioned, it is proportional to the first derivative of the gravitational potential.

2.4 Polarization of CMB photons

Observations of CMB shows that the signal is polarized. The origin of CMB photon polarization lies right in Thomson scattering. Consider a photon

moving towards an electron along the x axis. If the photon is polarized e.g. on the z axis the electron will start to oscillate in the z directions and the photon emitted is polarized in the plane parallel to the axis z. The situation at the last scattering surface was fairly different because radiation arrived on electrons from every direction and wasn't polarized. Polarization originated by Thomson scattering vanished because the contributes of different photons cancel each other. To derive the condition under which Thomson scattering produces polarization we characterize the intensity of the incident wave introducing Stokes' parameters. Consider a monochromatic electromagnetic wave that propagates along the direction z. It is characterized by the electric filed with components:

$$E_x = a_x \cos(\omega t - \xi_x) \tag{2.64}$$

$$E_y = a_y \cos(\omega t - \xi_y) \tag{2.65}$$

We associated the following parameters to the wave:

$$I = a_x^2 + a_y^2 \tag{2.66}$$

$$Q = a_x^2 - a_y^2 \tag{2.67}$$

$$U = 2a_x a_y \cos(\xi_x - \xi_y) \tag{2.68}$$

$$V = 2a_x a_y \sin(\xi_x - \xi_y) \tag{2.69}$$

These are the Stokes' parameter: I is called *intensity*, Q *polarization in the xy plane*, U *polarization in the xy plane but tilted of* $45°$ and V *circular polarization*. We can neglect V because Thomson scattering doesn't produce circular polarization. It can be shown the following relation:

$$I^2 = Q^2 + U^2 \tag{2.70}$$

Polarization can be also represented as a complex number:

$$P = |P| e^{i2\phi} = \sqrt{Q^2 + U^2} e^{i2\phi} = Q \pm iU \tag{2.71}$$

Under reflection on the x axis Q and U parameters transform as $\begin{cases} Q \to Q \\ U \to -U \end{cases}$

Consider now the case in which the incident wave arrives from a direction $\hat{n'}$. $\hat{\epsilon'}_1$ and $\hat{\epsilon'}_2$ are axes perpendicular to the directions $\hat{n'}$ and $z(= \hat{n})$ the propagation direction of the wave generated by the scattering with $\hat{\epsilon}_1 = x$ and $\hat{\epsilon}_2 = y$. The differential cross section of Thomson scattering can be written as:

$$\frac{d\sigma}{d\Omega} = \frac{3\sigma_T}{8\pi} \sum_{i,j=1}^{2} |\hat{\epsilon'}_j \left(\hat{n'}\right) \cdot \hat{\epsilon}_i (\hat{n}) |^2 \tag{2.72}$$

where $d\Omega$ is the solid angle covered by the versor $\hat{n}'$ e σ_T is the Thomson cross section. From the previous formula we derive that Q is proportional to:

$$\sum_{j=1}^{2} |\hat{\epsilon'}_j \cdot \hat{x}|^2 - \sum_{j=1}^{2} |\hat{\epsilon'}_j \cdot \hat{y}|^2 \tag{2.73}$$

this relation must be integrated on all possible directions of the incident wave in the solid angle $d\Omega$. We define the projection of $\hat{\epsilon'}_1$ and $\hat{\epsilon'}_2$ on the axes $\hat{y}$ and $\hat{x}$:

$$\hat{\epsilon}_1 \equiv (\cos\theta' \cos\phi', \cos\theta' \sin\phi', -\sin\theta') \tag{2.74}$$

$$\hat{\epsilon}_2 \equiv (-\sin\phi', \cos\phi', 0) \tag{2.75}$$

These definitions introduced in Q and integrated on the solid angle gives the expression:

$$Q(\hat{z}) = \frac{3\sigma_T}{16\pi\sigma_B} \int d\Omega' I'(\Omega') \sin^2\theta' \cos 2\phi' \tag{2.76}$$

where σ_B has the dimension of a cross section and I is the intensity of the incident wave. With similar calculation we find the expression for U

$$U(\hat{z}) = -\frac{3\sigma_T}{16\pi\sigma_B} \int d\Omega' I'(\Omega') \sin^2\theta' \sin 2\phi' \tag{2.77}$$

Combining (2.76) and (2.77) the polarization on $\hat{z}$ axis becomes:

$$Q(\hat{z}) - iU(\hat{z}) = \frac{3\sigma_T}{16\pi\sigma_B} \int d\Omega' I'(\Omega') \sin^2\theta' e^{i2\phi'} \tag{2.78}$$

Starting from this expression we can state the proportionality between polarization with the spherical harmonic Y_2^m. Now let us expand the incident wave in multipoles

$$I'(\Omega') = \sum_{l=0}^{\infty} \sum_{m=-l}^{l} a_{lm} Y_l^m(\theta', \phi') \tag{2.79}$$

and insert it in (2.78). Using the orthogonality property of spherical harmonics we get:

$$Q(\hat{z}) - iU(\hat{z}) = \frac{3\sigma_T}{4\pi\sigma_B} \sqrt{\frac{2\pi}{15}} a_{22} \tag{2.80}$$

This means that the condition for the generation of a net polarization in the cosmic fluid at recombination is the presence of a quadrupole perturbations as shown in figure (2.4). In general the polarization produced by a wave moving

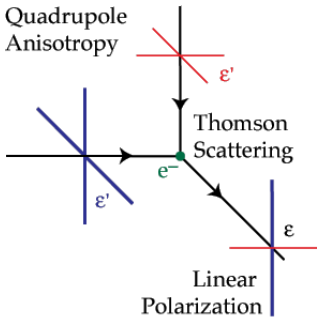

Figure 2.4: Linear polarization generated by Thomson scattering in presence of quadrupole anisotropy

along a generic direction forming an angle β with the z axis, supposing such incident radiation to be independent from the ϕ' angle, is:

$$Q(\hat{z}) - iU(\hat{z}) = -\frac{3\sigma_T}{16\pi\sigma_B}\sqrt{\frac{4\pi}{5}}a_{20}\sin^2\beta \tag{2.81}$$

The orthogonality of spherical harmonics ensures that only the quadrupole moment can generate a polarization through Thomson scattering. For $l = 2$ we have five possible values of $m = 0, \pm 1, \pm 2$ which represent *scalar, vector* and *tensor* perturbations. See figure (2.5) and (2.6).

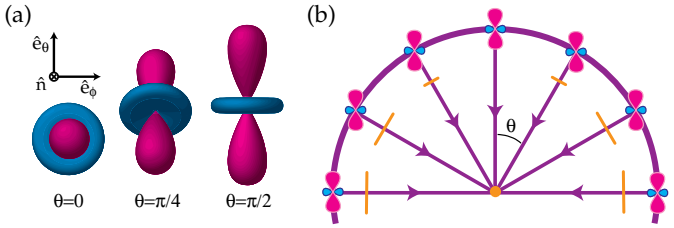

Figure 2.5: (a) Scalar perturbation $l = 2$ and $m = 0$ (b) polarization dependence from the angle under which the quadrupole is seen

2.4.1 Polarization patterns

The polarization we see in CMB sky is the result of the sum over many waves. For this reason we can't separate all the modes but just see the global 'pattern' of the polarization. Fortunately some properties of the polarization patterns survive to the overlap of all waves, such as the perturbation parity

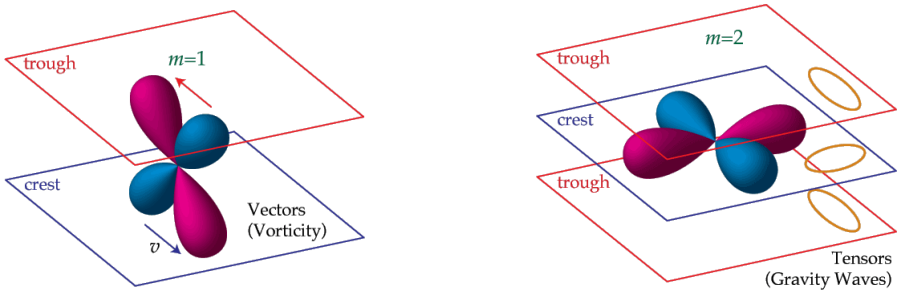

Figure 2.6: Vector perturbation $l = 2$ and $m = 1$ and tensor perturbation $l = 2$ and $m = 2$

(figure 2.7).

Polarization pattern can be decomposed in *electric component* E which has

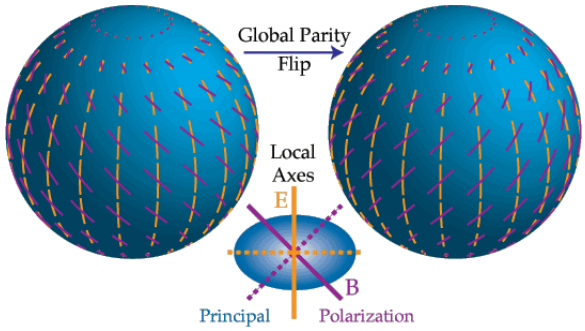

Figure 2.7: The behaviour of E and B modes under change of parity

parity $\pi = (-1)^l$ and the *magnetic component* B with parity $\pi = (-1)^{l+1}$. These means that for even l, such as $l = 2$, under transformations $\hat{n} \to -\hat{n}$ E modes remain unchanged while B modes change sign. Because these properties don't depend from the wave number k, it follows that the overlap of many waves with different modes k conserves parity.

It is possible to relate E and B with the second derivative of the stokes parameters. In tensor notation we define:

$$2P_{ij} = \begin{bmatrix} Q & U \\ U & -Q \end{bmatrix} \tag{2.82}$$

and the relations become:

$$\nabla^2 P_E = \partial^a \partial^b P_{ab} \tag{2.83}$$

$$\nabla^2 P_B = \epsilon_{ac} \partial^b \partial^c P^a_b \tag{2.84}$$

where ϵ_{ac} is an anti-symmetric tensor. The introduction of B and E modes is important mainly for two reasons: it allows to pass from a tensor field in Q and U to two new scalar fields (E and B). For these scalar fields we can define the power spectrum in analogy to what we have done for temperature:

$$C_l^{EE} = \frac{1}{2l+1}\sum_m \langle a^*_{E,lm} a_{E,lm}\rangle \tag{2.85}$$

$$C_l^{BB} = \frac{1}{2l+1}\sum_m \langle a^*_{B,lm} a_{B,lm}\rangle \tag{2.86}$$

Moreover the scalar perturbations can't produce B modes of polarization. They are only generated by metric perturbation i.e. gravitational waves. Their discovery would be very important because it could be a trace of a stochastic field of primordial gravitational waves originating directly from inflation.
Polarization patterns for different values of m are shown in figure (2.8), (2.9) and (2.11)

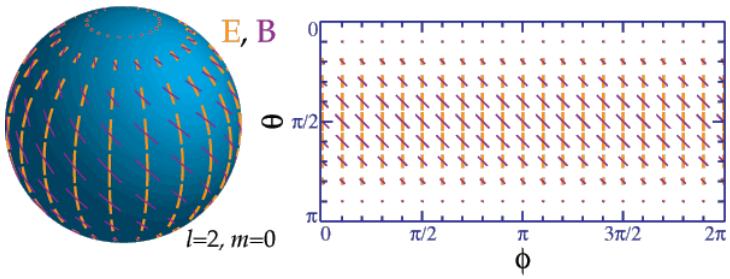

Figure 2.8: The polarization pattern for $l = 2$ and $m = 0$

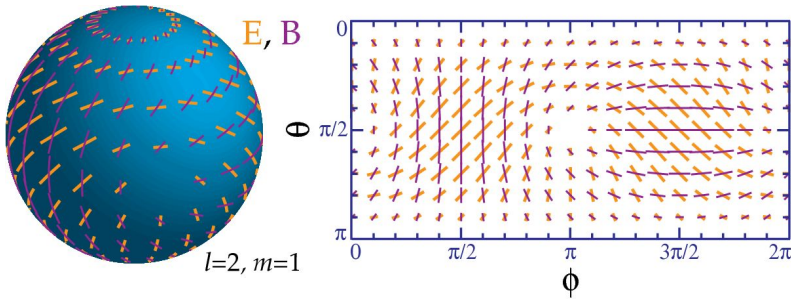

Figure 2.9: The polarization pattern for $l = 2$ and $m = 1$

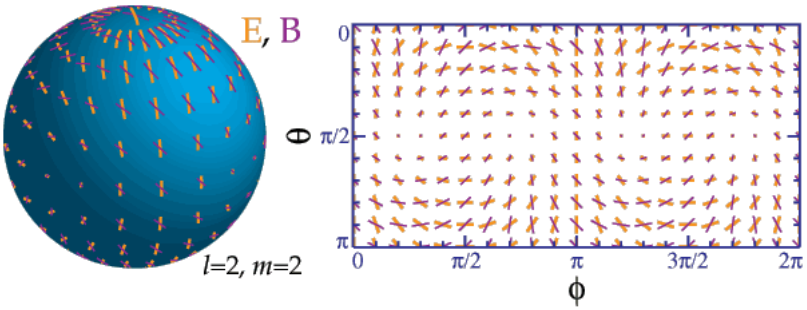

Figure 2.10: The polarization pattern for $l = 2$ and $m = 2$

2.5 CMB power spectrum

In this section we try to connect the observed pattern of temperature to the multipoles $\Theta_l(k, \eta_0)$. The temperature field can be characterized in this way:

$$T(\bar{x}, \bar{p}, \eta) = T(\eta)\left[1 + \Theta(\bar{x}, \bar{p}, \eta)\right] \tag{2.87}$$

Although this field is defined at every point in space and time, we can observe it only here (x_0) and now (η_0). Our sample is made up of the different directions of the incoming photons, $\bar{p}$. As we will see in the next section, the information we have from CMB is often held in maps wherein the temperature is reported at a number of incoming directions, or 'spots in the sky'. The spots in the sky are labeled by polar coordinates θ and ϕ . We can expand the field in spherical harmonics:

$$\Theta(\bar{x}, \bar{p}, \eta) = \sum_{l=0}^{\infty} \sum_{m=-l}^{l} a_{lm}(\bar{x}, \bar{p}) Y_l^m(\bar{p}) \tag{2.88}$$

l and m are conjugate to the real space unit vector $\hat{p}$, while the variable $\bar{k}$ is conjugate through a Fourier transform to the variable $\bar{x}$. This expansion is similar to the Fourier expansion of plane waves. The eigenfunctions of this transformation are the spherical harmonics $Y_l^m(\hat{p})$. Since the spherical harmonics are orthogonal, all the information is carried by the a_{lm} coefficients. Using the properties of spherical harmonics:

$$\int d\Omega Y_{lm}(\bar{p}) Y^*_{l'm'}(\bar{p}) = \delta_{ll'}\delta_{mm'} \tag{2.89}$$

It is possible to invert the relation and write a_{lm} as function of the observed anisotropy Θ_l:

$$a_{lm}(\bar{x}, \eta) = \int \frac{d^3k}{(2\pi)^3} e^{i\bar{k}\cdot\bar{x}} \int d\Omega Y^*_{l'm'}(\bar{p})\, \Theta\left(\bar{k}, \bar{p}, \eta\right) \tag{2.90}$$

Of course no cosmological models can predict the specific value of the a_{lm} that will be observed, but just their distribution. If the cosmological model involves the standard theory of inflation it will predict a random temperature field of anisotropies and, consequently, a_{lm} will be drawn from a gaussian distribution. The a_{lm} distribution has a zero mean. For this reason all the information is carried by the variance of the distribution which is called C_l.

$$\langle a_{lm} \rangle = 0 \tag{2.91}$$

$$\langle a_{lm} a^*_{l'm'} \rangle = \delta_{ll'} \delta_{mm'} C_l \tag{2.92}$$

For a given l the a_{lm} have their own variance. Since for a given l the distribution of the a_{lm} is sampled $2l + 1$ times, the number of a_{lm} on which calculate the variance is fixed. Because such a sample can be drawn from the distribution in a infinite number of ways, the value of C_l is given by an *estimator* defined as:

$$C_l = \frac{1}{2l+1} \sum_{m=-l}^{l} |a_{lm}|^2 \tag{2.93}$$

C_l takes for this reason the name of *pseudo-C_l*. This estimator follows a χ^2 distribution, which has a variance called *cosmic variance* and is calculated as:

$$\left(\frac{\Delta C_l}{C_l} \right) = \sqrt{\frac{2}{2l+1}} \tag{2.94}$$

The physical meaning of the cosmic variance is related to the connection of the harmonic l, m indices to the physical quantities. l is related to the scale of the perturbation $|k|$ while the information on the direction, $\bar{k}$, is given by the m index. Therefore, since we fix l we have just $2l + 1$ independent way of setting the spherical harmonic and this imposes a lower limit on the precision with which we can know the C_l. Of course this problematic affects more the large scales, where our uncertainties on the determination of the C_l are inevitably larger.

The counterpart of the angular power spectrum in real space is the angular two-point correlation function of the temperature field. They are related by:

$$C(\theta) \equiv \langle \Theta(\hat{n_1}) \Theta(\hat{n_2}) \rangle = \frac{1}{4\pi} \sum_{l=0}^{\infty} (2l+1) C_l \mathcal{P}_l (\hat{n_1} \cdot \hat{n_2}) \tag{2.95}$$

where $\hat{n_1} \cdot \hat{n_2} = \cos(\theta)$. This quantity contains the same information of the power spectrum, with the assumption of statistical isotropy.

We need an expression for C_l in terms of $\Theta_l(k)$. We begin squaring the equation (2.90) and taking the expectation value of the distribution. We now need $\langle \Theta\left(\bar{k},\hat{p}\right)\Theta^*\left(\bar{k}',\hat{p'}\right)\rangle$. This calculation is complex because it depends on two factors, *i*) the amplitude of the initial perturbation generated by inflation, *ii*) the evolution of the perturbation at the horizon entering already seen in the previous chapter. To overcome this problem we factorize the anisotropy in this way $\delta * \left(\frac{\Theta}{\delta}\right)$ where δ is the initial amplitude of the perturbation (independent from the direction) and the ratio $\left(\frac{\Theta}{\delta}\right)$ describes the evolution of the perturbation at the horizon entering. Therefore we have:

$$\langle \Theta\left(\bar{k},\hat{p}\right)\Theta^*\left(\bar{k}',\hat{p'}\right)\rangle = \langle \delta\left(\bar{k}\right)\delta^*\left(\bar{k}'\right)\rangle \frac{\Theta\left(\bar{k},\hat{p}\right)}{\delta\left(\bar{k}\right)}\frac{\Theta^*\left(\bar{k}',\hat{p}\right)}{\delta^*\left(\bar{k}'\right)} \tag{2.96}$$

Now we define the *primordial power spectrum*:

$$\langle \delta\left(\bar{k}\right)\delta^*\left(\bar{k}'\right)\rangle = (2\pi)^3\,\delta^3\left(\bar{k}-\bar{k}'\right)P(k) \tag{2.97}$$

and get:

$$\langle \Theta\left(\bar{k},\hat{p}\right)\Theta^*\left(\bar{k}',\hat{p'}\right)\rangle = (2\pi)^3\,\delta^3\left(\bar{k}-\bar{k}'\right)P(k)\,\frac{\Theta\left(k,\hat{k}\cdot\hat{p}\right)}{\delta(k)}\frac{\Theta^*\left(k,\hat{k}\cdot\hat{p'}\right)}{\delta^*(k)} \tag{2.98}$$

Recalling equation (2.90), we obtain the anisotropy power spectrum:

$$C_l = \int \frac{d^3k}{(2\pi)^3}P(k)\int d\Omega Y^*_{lm}(\bar{p})\,\frac{\Theta\left(k,\hat{k}\cdot\hat{p}\right)}{\delta(k)}\int d\Omega' Y^*_{lm}(\bar{p'})\,\frac{\Theta^*\left(k,\hat{k}\cdot\hat{p'}\right)}{\delta^*(k)} \tag{2.99}$$

so we can expand the anisotropy as in equation (2.53):

$$\Theta\left(k,\hat{k}\cdot\hat{p}\right) = \sum_l (-i)^l(2l+1)\,\mathcal{P}_l\left(\hat{k}\cdot\hat{p}\right)\Theta_l(k) \tag{2.100}$$

This leads to:

$$C_l = \int \frac{d^3k}{(2\pi)^3}P(k)\sum_{l'l''}(-i)^{l'}(-i)^{l''}(2l'+1)(2l''+1)\,\frac{\Theta_{l'}(k)\,\Theta^*_{l''}(k)}{|\delta(k)|^2} \tag{2.101}$$

$$\int d\Omega\mathcal{P}_{l'}\left(\hat{k}\cdot\hat{p}\right)Y^*_{lm}(\bar{p})\int d\Omega'\mathcal{P}_{l''}\left(\hat{k}\cdot\hat{p'}\right)Y_{lm}(\bar{p'}) \tag{2.102}$$

After some calculations ad considering the properties of spherical harmonics, we obtain at the end:

$$C_l = \frac{2}{\pi}\int_0^\infty dk k^2 P(k)\left|\frac{\Theta_l(k)}{\delta(k)}\right|^2 \tag{2.103}$$

The power spectrum represents the integral over all modes of the variance of $\Theta_l(k)$.

2.6 The anisotropy spectrum today

2.6.1 Sachs-Wolfe effect: large scales

As we said, the largest scales entered the horizon after recombination in a purely matter dominated era. We also mentioned that the balance between the gravitational action of dark matter and the expansion of universe kept the gravitational potential constant on all linear scales. For this reason going back to the equation we pulled for Sachs Wolfe:

$$[\Theta + \Phi](k, \eta_{rec}) \simeq \frac{1}{3}\Psi(k, \eta_{rec}) \tag{2.104}$$

we can substitute η_{rec} with η_0. By using the cosmological Poisson equation in Fourier space to relate the potential to the initial perturbation:

$$k^2\Phi(k, \eta) = -4\pi G a^2(\eta)\,\delta(k, \eta) \tag{2.105}$$

we can write:

$$\Theta(k, \eta_0) \simeq \frac{1}{3}\Psi(k, \eta_0) \propto \frac{1}{k^2}\delta(k, \eta) \rightarrow \Theta_l(k, \eta_0) \propto \frac{1}{k^2}\delta(k)\, j_l(k\eta_0) \tag{2.106}$$

$$\left|\frac{\Theta_l(k)}{\delta(k)}\right|^2 \propto \frac{1}{k^4} j_l^2(k\eta_0) \tag{2.107}$$

Using equation (2.103) we obtain the contribution to C_l due to SW effect:

$$C_l^{SW} \propto \int_0^\infty \frac{dk}{k^2} j_l^2[k(\eta_0 - \eta_{rec})] \tag{2.108}$$

This integral can be solved imposing a particular form of the initial power spectrum given by a particular inflationary model e.g. $P(k) \propto k^n$. Considering a scale invariant power spectrum (Harrison -Zel'dovich solution) the CMB power spectrum on large scales becomes:

$$l(l+1)\, C_l^{SW} \propto \delta_H^2 \tag{2.109}$$

Where δ_H represents the perturbation amplitude at the horizon crossing. This means that on large scales in the CMB power spectrum we are looking at very primordial features as the plateau present at those scales is the trace of the primordial potential generated by inflation. We can also consider in recent epochs the late - Integrated Sachs Wolfe, which has an effect very similar to SW and appears in the power spectrum as a slight lift of the Sachs-Wolfe plateau on very large scales.

2.6.2 Small scales

The small-scale anisotropy spectrum depends not only on the monopole but also on the dipole and the integrated Sachs - Wolfe effect as stated in equation (2.63). The *monopole* at recombination $(\Theta_0 + \Phi)(k, \eta_*)$ free-streams to us today, creating anisotropies on angular scales $l \sim k\eta_0$. We now can see two main effects: the first is that the 'zeroes' of the spectrum are smoothed because many modes contribute to anisotropy on a singular angular scale. This changes the zero in a trough in the C_l spectrum. The second effect concern a shift of the peak to $l < k\eta_0$ due to the particular properties of spherical Bessel functions. The *dipole* at recombination is smaller than the monopole but it is out of phase with it. For this reason the dipole contributes more to the anisotropy when the monopole contributes less and the effect of the dipole is to fill the troughs. The last contribution is that of the *integrated Sachs - Wolfe effect*. In this case we are referring to early - ISW given by the decay of the potential caused by residual radiation pressure during the recombination era. The early-ISW adds in phase with the monopole causing a slight shifting and increasing of the peaks.
In figure (2.12) is shown the power spectrum of CMB temperature anisotropies

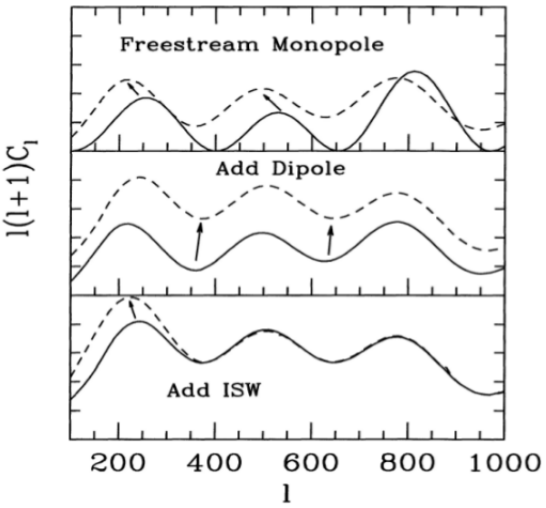

Figure 2.11: Anisotropies free-streaming seen in the power spectrum

as derived from Planck data.

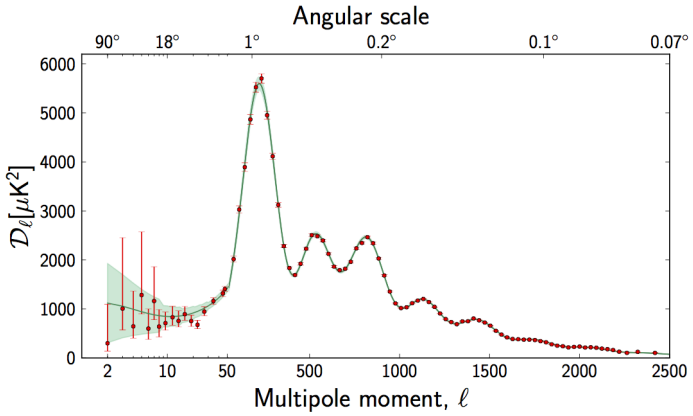

Figure 2.12: Planck CMB spectrum. The shaded regions on large scales represents cosmic variance. On the y axis there is the normalized quantity $D_l = l(l+1)C_l/2\pi$

2.6.3 Polarization spectrum and correlation with temperature

As we have seen, polarization is generated by the quadrupole moment. This moment is of order of $kv_\gamma/\dot{\tau}$ where v_γ is the dipole Θ_1. Since the dipole is out of phase with respect to the monopole the result is a power spectrum characterized by peaks shifted with respect to the temperature acoustic peaks. Moreover the quadrupole is subdominant during the recombination and this cause the polarization power spectrum to be ten time lower than the temperature power spectrum as shown in figure (2.13).

The temperature-polarization power spectrum is more complex. It shows a large angle anti-correlation between $(50 < l < 150)$. To roughly explain it we give here a further expression for the polarization signal which shows its dependence from the gradient of the peculiar velocity of the photon fluid Θ_1

$$\Delta_E \simeq -0.17(1-\mu^2)\Delta\eta_{dec} k\Theta_1(\eta_{dec}) \tag{2.110}$$

where Δ_E is the polarization fluctuation, η_{dec} is the conformal time at decouplig, $\Delta\eta_{dec}$ is the thickness of the surface of the last scattering in conformal time, and $\mu = \cos(\bar{k}\cdot\bar{n})$. The velocity gradient generates a quadrupole temperature anisotropy pattern around electrons which, in turn, produces the E-mode polarization. Bringing together the expression (2.110) and the expression of the CMB temperature perturbation already derived in (2.39) :

$$\Delta_T \simeq -\frac{1}{3}\Phi(\eta_{dec})\cos(kc_s\eta_{dec}) \tag{2.111}$$

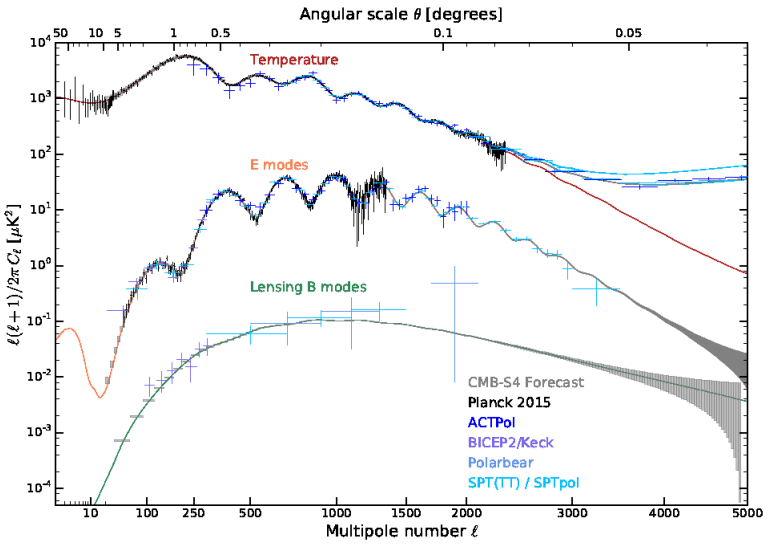

Figure 2.13: Comparison between the temperature anisotropy power spectrum and the polarization power spectrum for different experiments. From the picture it is clear the phase shift between the peaks of the two power spectrum

We obtain:

$$\langle \Delta_T \Delta_E \rangle \simeq -0.03(1-\mu^2)(kc_s\Delta_{dec})P_\Phi(k)\sin(2kc_s\eta_{dec}) \tag{2.112}$$

where $P_\Phi(k)$ is the power spectrum of $\Phi(\eta_{dec})$. Clearly, there is an anti - correlation peak near $kc_s\eta_{dec} \sim 3\pi/4$ which correspond to $l \sim 150$ as shown in figure (2.14):

2.7 Cosmological parameters

The anisotropy power spectrum depends on cosmological parameters and for this reason CMB is considered one of the major probe of precision cosmology. For our purpose we just mention some of the cosmological parameters that strongly affect the position, the amplitude and the separation of the peaks. The parameter chosen are:

- curvature density, $\Omega_k \equiv 1 - \Omega_m - \Omega_\Lambda$
- Baryon density, $\Omega_b h^2$
- matter density, $\Omega_m h^2$

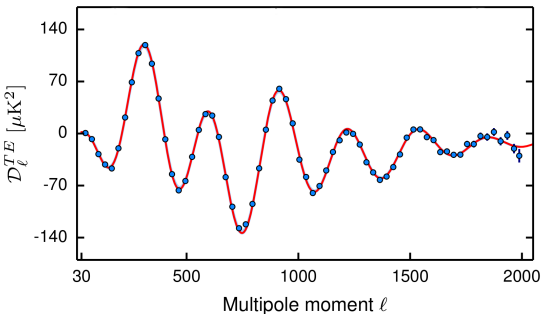

Figure 2.14: Planck temperature-polarization power spectrum. On the y axis there is the normalized quantity $D_l = l(l+1)C_l/2\pi$. It is clear the large angle anti-correlation with $l = [50; 150]$

- cosmological constant energy density, Ω_Λ

Curvature: if the universe was open rather than flat the geodesic of photons starting out from the last scattering surface wouldn't be parallel but slowly diverge. This cause the first peak to be moved to a smaller angular scale than in a flat universe, which means to higher l. This effect is related to the different comoving angular distance that is simply $\eta_0 - \eta_*$ in a flat universe while in a open universe is given by:

$$d_a = \frac{a}{H_0\sqrt{|\Omega_k|}} \sin\left(\sqrt{-\Omega_k} H_0 \chi\right) \tag{2.113}$$

where χ is the comoving distance. For example with $\Omega_k = 0.7$ the angular diameter distance is increased by a factor 1.7

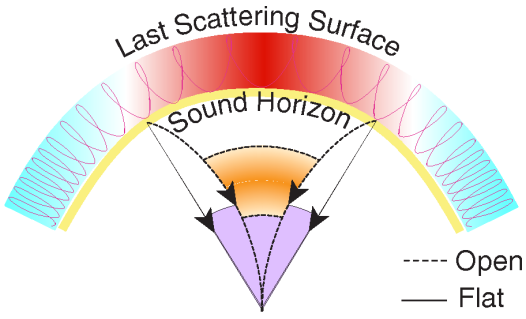

Figure 2.15: Last scattering surface as seen in a flat or open universe

The last three parameters induce a small shift in the location of peaks and troughs in the spectrum. Inhomogeneities on scale k show up at $l = k\eta_0$

in a flat universe. Consequently the peaks will be located at $l_p \simeq k_p\eta_0 \simeq n\pi\eta_0/r_s(\eta_*)$. This ratio is sensitive to matter and baryon densities as the spacing of the peaks increase if those densities go down. The introduction of a cosmological constant instead affect η_0 causing again a shift of the peaks.
Baryon density: in addition to the already mentioned shifting of the peaks due to the change of the sound horizon, variations in baryon density affect the heights of the peaks. As we saw in the paragraph concerning the baryon loading the presence of baryons increases the deepness of the peaks - adding extra force to the potential wells of dark matter - and breaks the symmetry between odd and even peaks. This feature makes the baryon density a contribute quite easy to individuate.
Matter density: if the matter density is low, the epoch of equality occurred closer to recombination, so that the radiation density must be taken into account in the formation of inhomogeneities at the decoupling. The decaying of the potential due to the photon pressure provides a strong driving force for the oscillations. Therefore $\Theta_0(\eta_*)$ is larger than in a purely matter dominated universe. Moreover, since the potential is not constant there is a increasing contribute due to the early-ISW increasing the small scale anisotropies.
Cosmological constant: this phenomena rises at $z \simeq 0.3$ so it can't have affected inhomogeneities during recombination. The only possible effects occur on the free-streaming on very large scales. The spectrum is slightly shifted to small scales and the spectrum is lower on small scales. This is due to a large angle ri-normalization: the late-ISW enhances the anisotropies on large scales. If we normalize on large l the small - scales anisotropies are correspondingly reduced.

2.8 Observations in CMB

To extract information from CMB, building for example the power spectrum, it is necessary to know how to deal with CMB data. The first step to do that is to know the base of data analysis.
The fundamental block of data analysis is the *likelihood function*. It is defined as the probability that a given experiment would get the data it did given a theory. Once we have the shape of the likelihood we can determine the parameter of the theory (best estimate is the place in parameter space where the likelihood function is largest) along with errors (determined by the width of the likelihoood function). Of course the definition of likelihood function is not directly usable in the context of CMB experiment. There we have the data d_i and we want to obtain the parameters of the theory, call them e.g.

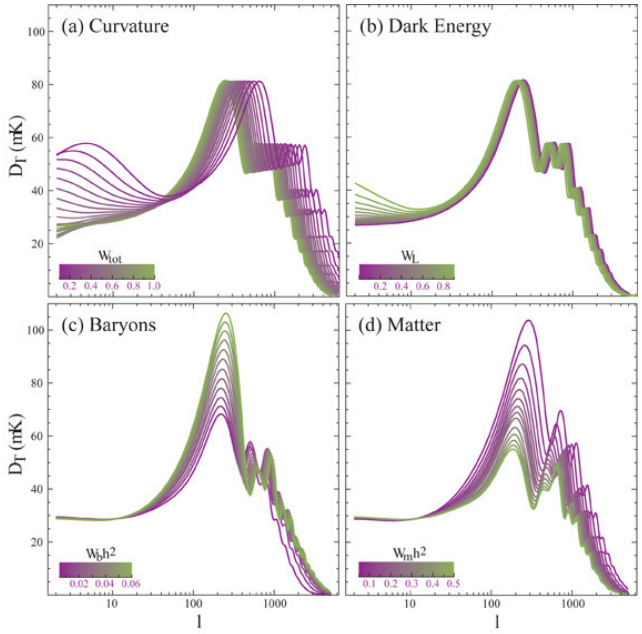

Figure 2.16: The effect of curvature, baryon and matter density and cosmological constant on the acoustic peaks

λ_i. We don't want $P[d_i|\lambda_i]$ (which is the likelihood) but rather $P[\lambda_i|d_i]$. To relate the two expression we use the probability relation:

$$P[B \cap A] = P[B|A]\,P[A] = P[A|B]\,P[B] \tag{2.114}$$

In this context $A = d_i$ and $B = (\lambda_i)$ and we get:

$$P[\lambda_i|d_i] = \frac{P[d_i|\lambda_i]\,P[\lambda_i]}{P[d_i]} \tag{2.115}$$

The denominator doesn't depend from λ_i so it doesn't effect the place in parameter space where the likelihood function peaks or its width. Hence we will ignore it. The term $P[\lambda_i]$ is called *prior probability*. It represents the information we already have about the experiment. In the case we don't have information or we don't want to make any assumptions we choose an uniform prior and we obtain:

$$P[\lambda_i|d_i] \propto \mathcal{L} \tag{2.116}$$

This proportionality guarantee that the parameters which maximize the posterior also maximize the likelihood. The estimators that we obtain maximizing the likelihood have the important property to be unbiased: their

average value coincides with the true value of the parameters. Moreover the error with which we determine these parameters are the smallest possible: we assume as a measurement of the precision of our estimated parameters the width of the Likelihood itself. The width is the *curvature* of the Likelihood calculated in its maximum. The curvature measures how rapidly the likelihood falls away from the maximum. If the curvature is small, then the likelihood changes slowly and the data are not very constraining: the resulting uncertainties will be large. Conversely, large curvature means small uncertainties. We can now consider the logarithm of the likelihood function and perform a Taylor expansion:

$$\ln \mathcal{L}(x,\lambda) = \ln \mathcal{L}(x,\hat{\lambda}) + \frac{1}{2}(\lambda_i - \hat{\lambda}_i)\frac{\partial^2 \ln \mathcal{L}}{\partial\lambda_i \partial\lambda_j}(\lambda_j - \hat{\lambda}_j) \tag{2.117}$$

The matrix $H_{i,j} = \frac{\partial^2 \ln \mathcal{L}}{\partial\lambda_i \partial\lambda_j}$ is the Hessian matrix which quantifies the curvature of the likelihood. This matrix also tells us if the estimates of the parameters λ_i, λ_j present some correlations. In the case in which the estimated parameters are uncorrelated the Hessian matrix is simply diagonal. If the parameters were uncorrelated the error on one of them is simply

$$\sigma_i = \frac{1}{\sqrt{H_{ii}}} \tag{2.118}$$

If we want to reproduce a more realistic case in which the estimated parameters are correlated with each other we have to compute the inverse of the Hessian matrix and we obtain:

$$\sigma_i = \sqrt{H_{ii}^{-1}} \tag{2.119}$$

The last step to obtain the errors on the parameters passes from the definition of the *Fisher Matrix*. It is the expectation value of the Hessian matrix:

$$F_{i,j} = \langle H_{i,j} \rangle = \langle \frac{\partial^2 \ln \mathcal{L}}{\partial\lambda_i \partial\lambda_j} \rangle \tag{2.120}$$

and the definitive expression for the *marginal error* is

$$\sigma_\lambda = \sqrt{F_{\lambda\lambda}^{-1}} \tag{2.121}$$

These error are hence related to the curvature of the likelihood and this means that no estimators can give error bars smaller than the *Maximum Likelihood estimate*.

2.8.1 CMB likelihood

Consider a CMB data set. The true value of temperature anisotropy in a given spot on the sky is called s. The estimated value of this temperature anisotropy is Δ and the variance of the estimator, which represent the spread of the measurement, is C_N. We want to compare the data Δ, C_N with the theory. The theory we are referring to is inflation, which predict that the true value of the anisotropy of a given spot is drawn from a Gaussian distribution with a variance C_s. So the probability that the sky temperature in a particular direction falls in a range between s and $s + ds$ is:

$$P(s)\, ds = \frac{1}{\sqrt{2\pi C_S}} \exp\left(\frac{-s^2}{2C_S}\right) ds \tag{2.122}$$

To obtain the likelihood function we have to integrate on the distribution of all possible values of s.

$$\mathcal{L} = \int_{-\infty}^{\infty} \frac{ds}{\sqrt{2\pi C_S}} \exp\left(\frac{-s^2}{2C_S}\right) \frac{1}{\sqrt{2\pi C_N}} \exp\left(\frac{-(\Delta - s)^2}{2C_N}\right) \tag{2.123}$$

We define

$$C \equiv C_S + C_N \tag{2.124}$$

and change variables $x = s - C_S\Delta/C$. Through some calculations we get the final expression of the likelihood

$$\mathcal{L} = \sqrt{\frac{1}{2\pi C}} \exp\left(\frac{-\Delta^2}{2C}\right) \tag{2.125}$$

This is the definitive expression of likelihood for a one pixel experiment: the measured temperature should be distributed like a Gaussian with a variance given by the sum of the variance of noise and signal. The expression (2.125) can be generalized to the case of many pixel N_p:

$$\mathcal{L} = \frac{1}{(2\pi)^{N_p/2} (\det C)^{1/2}} \exp\left(-\frac{1}{2}\Delta C^{-1}\Delta\right) \tag{2.126}$$

where Δ is the data vector consisting of all N_p measurements and C is the full covariance matrix. The matrix C is typically not diagonal. However to our purpose we can consider the special case in which C is diagonal and proportional to the identity matrix. We can find the expected variance of the signal by differentiating the likelihood function with respect to C_S and set it to zero.

$$\frac{\partial \mathcal{L}}{\partial C_S} = 0 \rightarrow C_S = \frac{1}{N_p} \sum_{i=1}^{N_p} \Delta_i^2 - C_N \tag{2.127}$$

The signal covariance is the difference between the variance of the data points and average noise per pixel. We can also derive the error in this determination of C_S. The error is proportional to the width of the likelihood function. A simple way to approximate the width is to assume that $\mathcal{L}$ is Gaussian in the parameters, or equivalently that $\ln(\mathcal{L})$ is quadratic in the parameters. The variance of a Gaussian distribution is twice the inverse of the coefficient of the quadratic term, so we can simply identify the variance (the square of the errors) by computing this coefficient.

$$\sigma_{C_s} = \left(\frac{-\partial^2 \ln \mathcal{L}}{\partial C_s^2} \right)^{-1/2} \rightarrow \sigma_{C_s} = \sqrt{\frac{2}{N_p}} \left(C_S + C_N \right) \tag{2.128}$$

2.8.2 CMB window function

We have now to address the question of how the expected variance in a given experiment is related to the underlying power spectrum. To do that it is necessary to relate the predicted C_l's to the expected covariance matrix C_S. Consider for simplicity the diagonal element of the covariance matrix:

$$C_{S,ii} \equiv \langle s_i s_i \rangle \tag{2.129}$$

This average is over many realizations of the theoretical distribution and the subscript i labels the pixels. The anisotropy expected in each pixel is:

$$s_i = \int d\hat{n} \Theta \left(\hat{n} \right) B_i \left(\hat{n} \right) \tag{2.130}$$

where B_i is the beam pattern at the ith pixel and Θ is the underlying temperature. To find C_S we square the previous equation and expand Θ in spherical harmonics:

$$\frac{C_{S,ii}}{T^2} = \int d\hat{n} \int d\hat{n}' B_i \left(\hat{n} \right) B_i(\hat{n}') \sum_{lm} Y_{lm} \left(\hat{n} \right) \sum_{l'm'} Y^*_{l'm'}(\hat{n}') \langle a_{lm} a^*_{l'm'} \rangle \tag{2.131}$$

Using the definition of C_l it gives:

$$\frac{C_{S,ii}}{T^2} = \int d\hat{n} \int d\hat{n}' B_i \left(\hat{n} \right) B_i(\hat{n}') \sum_{l} C_l \sum_{m} Y_{lm} \left(\hat{n} \right) Y^*_{lm}(\hat{n}') \tag{2.132}$$

But for the properties of spherical harmonics $\sum_m Y_{lm} \left(\hat{n} \right) Y^*_{lm}(\hat{n}') = (2l + 1) P_l(\hat{n} \cdot \hat{n}')/4\pi$ so we obtain:

$$\frac{C_{S,ii}}{T^2} = \sum_l \frac{2l+1}{4\pi} C_l W_{l,ii} \tag{2.133}$$

where the *window function* is defined as:

$$W_{l,ii} \equiv \int d\hat{n} \int d\hat{n}' B_i(\hat{n}) B_i(\hat{n}') P_l(\hat{n} \cdot \hat{n}') \tag{2.134}$$

If $\hat{n}'$ and $\hat{n}$ are close to each other we can use the flat space approximation. The three dimensional vectors can be approximated as two dimensional vectors $\bar{x}$, $\bar{x}'$. The distance between the spots individuated by $\bar{x}$ and $\bar{x}'$ is equal to the angle between $\hat{n}'$ and $\hat{n}$. The expression of the window function hence is:

$$W_{l,ii} \equiv \int dx \int dx' B_i(\bar{x}) B_i(\bar{x}') P_l(\cos(|\bar{x} - \bar{x}'|)) \tag{2.135}$$

Using a property of Legendre polynomials we can now write:

$$P_l(\cos(|\bar{x} - \bar{x}'|)) \to \mathcal{J}_0(l|\bar{x} - \bar{x}'|) = \frac{1}{2\pi} \int_0^{2\pi} d\phi e^{-il|\bar{x}-\bar{x}'|\cos\phi} \tag{2.136}$$

this approximation is valid in the large l limit, which is right the small angle limit that we use for the flat space approximation. If we assume that ϕ is the angle between $\bar{l}$ and $|\bar{x} - \bar{x}'|$ the integral becomes:

$$\int d^2x B_i(\bar{x}) e^{-i\bar{l}\cdot\bar{x}} \equiv B_i(\hat{l}) \tag{2.137}$$

where $B_i(\hat{l})$ is the Fourier transform of the beam pattern. The $\bar{x}'$ integral is the complex conjugate of this, so the window function simplifies to:

$$W_{l,ii} = \frac{1}{2\pi} \int_0^{2\pi} d\phi \left| B_i(\hat{l}) \right|^2 \tag{2.138}$$

The window function is at the end the angular average of the square of the *2D transform* of the beam pattern. A complete evaluation of the likelihood function requires the calculation of all the elements of the covariance matrix, which means $N_p(N_p + 1)/2$ calculation if N_p is the number of the pixels.

An example of window function is the one obtained from a *Gaussian beam*: this is an approximation used in CMB experiments. The beam pattern for the ith pixel is:

$$B_i(\bar{x}) = \frac{1}{2\pi\sigma^2} \exp\left(-\frac{(\bar{x} - \bar{x}_i)^2}{2\sigma^2}\right) \tag{2.139}$$

For this computation we can put x_i to zero. The Fourier transform of the beam is also a Gaussian

$$B_i(\bar{l}) = \frac{1}{2\pi\sigma^2} \int d^2x e^{-i\bar{l}\cdot\bar{x}} \exp\left(-\frac{x^2}{2\sigma^2}\right) = e^{-l^2\sigma^2/2} \tag{2.140}$$

In this example B does not depend on the direction of $\bar{l}$, so there is no need to take the angular average. The window function is simply the square of the Fourier transform:

$$W_{l,ii} = e^{-l^2\sigma^2} \tag{2.141}$$

2.8.3 Masked sky

In the previous section we learned how to relate the covariance matrix with the underling power spectrum. From section 2.5 we know that the best unbiased estimator for C_l in the case of a noiseless experiment covering the full sky is

$$C_l = \frac{1}{2l+1}\sum_m |a_{lm}|^2 \tag{2.142}$$

Now we can ask how our estimator changes if we are in a more real situation with the presence of noise and a partial sky covering. This case is complicated because the mask used to cover the CMB map along the galactic plane introduces not negligible correlations between different C_l and their distribution is no longer a simple χ^2. In order to solve the problem we present here the treatment proposed for the first time in by B. D. Wandelt, E. Hivon and K.M. Gorski in 2000 and in [53] which gives a framework for studying the sampling statistic of the C_l for incomplete sky coverage in presence of non uniform noise. As we have already seen in equation (2.88) we can expand the temperature anisotropy in spherical harmonics:

$$\Theta\left(\bar{x},\bar{p},\eta\right) = \sum_{l=0}^{\infty}\sum_{m=-l}^{l} a_{lm}Y_l^m\left(\bar{p}\right) \tag{2.143}$$

In this case the a_{lm} are independent, Gaussian distributed with zero mean and variance $C_l^{theory} \equiv \langle |a_{lm}|^2 \rangle$. Consider now the case in which the instrumental set-up introduces a Gaussian noise with zero mean $W_N(\theta,\phi)$ and the sky is partially covered so both signal and noise are modulated by a window function with varying amplitude $W(\theta,\phi)$. The temperature anisotropy map will be:

$$\tilde{\Theta}(\theta,\phi) = W(\theta,\phi)[\Theta(\theta,\phi) + W_N(\theta,\phi)\Theta(\theta,\phi)] \tag{2.144}$$

where $W(\theta,\phi)$ is unity in the observed region and zero elsewhere. The coefficients of the spherical harmonic expansion are then:

$$\tilde{a}_{lm} = \int_{\mathcal{O}} d\Omega Y^*_{l'm'}(\theta,\phi)\Theta(\theta,\phi) = \sum_{lm} a_{lm}\int_{\mathcal{O}} d\Omega Y^*_{l'm'}(\theta,\phi)Y_{lm}(\theta,\phi) \tag{2.145}$$

The notation $\int_{\mathcal{O}}$ denotes the integral over the observed regions. The property of orthogonality of the Y_{lm} is no longer valid because we are not integrating over all solid angle. Let's define the *geometric coupling matrix*:

$$W_{l'm'lm} = \int_{\mathcal{O}} d\Omega Y^*_{l'm'}(\theta,\phi) Y_{lm}(\theta,\phi) \tag{2.146}$$

$W_{l'm'lm}$ is just the element of the window matrix in spherical harmonics. Now we can write:

$$\tilde{a}_{l'm'} = \sum_{lm} W_{l'm'lm} a_{lm} \tag{2.147}$$

This means that expanding $\Theta(\theta,\phi)$ produces a set of correlated Gaussian variables $\tilde{a}_{lm}$ for the signal and $\tilde{a}_{Nlm}$ for the noise. These combine into the power spectrum coefficients that becomes:

$$\tilde{C}_l = \frac{1}{2l+1} \sum_m |\tilde{a}_{lm} + \tilde{a}_{Nlm}|^2 \tag{2.148}$$

When we are working with masked sky we usually wish to correct for the effects induced by the mask. A very simple solution is to divide the power spectrum obtained from the masked map for the fraction of the sky unmasked. This procedure can be used only if the fraction of the sky covered is small. Instead, if the value of f_{sky} is far from the unity, the correlations induced by the mask between different C_l are not negligible and we need a more sophisticated procedure, which involve the calculation of a kernel to be applied to the pseudo-cl obtained from the mask sky to correct them. This calculation is done through a code named Master that will be explained in section 3.4

2.8.4 Fisher matrix for CMB

We want now to associate the error bars to the C_l. We try to determine the full fisher matrix for CMB. To do that it is necessary to decide what parameters we are interested in and what pixelization scheme we want to use. We choose as parameters the C_l themselves. The pixelization scheme chosen in the case of the CMB is based on the a_{lm}. That is, instead of using the pixelized temperatures $\Theta(\hat{n})$, use

$$a_{lm} = \int d\Omega Y^*_{lm}(\hat{n}) \Theta(\hat{n}) \tag{2.149}$$

as the data values. Each pixel then is labeled by l and m, so a given row (or column) in the covariance matrix corresponds to a fixed valued of l and

m. The covariance matrix is the sum of signal and noise covariance matrix. The signal covariance matrix would be $\delta_{ll'}\delta_{mm'}C_l$ if the window function were unity. Let's assume that the experiment measures the anisotropy with a beam size σ. Then the signal covariance matrix must be multiplied by $e^{-l^2\sigma^2}$. In the case of uncorrelated uniform noise the noise covariance matrix is $\delta_{ll'}\delta_{mm'}w^{-1}$. We use w to indicate the *weight* defined as:

$$w = [(\Delta\Omega)\sigma_n^2]^{-1} \tag{2.150}$$

where $\Delta\Omega$ is the size in radians of the real space pixel and σ_n is the noise per pixel. Putting this two together we have the expression for the covariance matrix:

$$C_{lm,l'm'} = \delta_{ll'}\delta_{mm'}[C_l e^{-l^2\sigma^2} + w^{-1}] \tag{2.151}$$

Through some calculations we can now compute the Fisher matrix, which in *all sky limit* results:

$$F_{ll'} = \frac{2l+1}{2}\delta_{ll'}e^{-2l^2\sigma^2}[C_l e^{-l^2\sigma^2} + w^{-1}]^{-2} \tag{2.152}$$

In all sky surveys the Fisher matrix for the C_l is diagonal. There are no correlations between adjacent C_l. The errors on a given C_l expected in all-sky experiment, as we saw in equation (2.121), are equal to $\sqrt{F^{-1}}$ so:

$$\delta C_l = \sqrt{\frac{2}{2l+1}}[C_l + w^{-1}e^{-l^2\sigma^2}] \tag{2.153}$$

There are mainly two sources of error: i) cosmic variance, proportional to the signal itself and ii) noise -atmospheric or instrumental - given by the weight w and the smoothing determined by the beam width σ.We give here also an approximated formula that describe an experiment also in the case of *partial sky*. It can be obtained recalling that the factor $2l+1$ in the denominator of (2.153) counts the number of independent samples. So, if the experiment cover a fraction of the sky $f_{sky} < 1$, the error on the C_l will be:

$$\delta C_l = \sqrt{\frac{2}{(2l+1)f_{sky}}}[C_l + w^{-1}e^{-l^2\sigma^2}] \tag{2.154}$$

This approximation is good in the limit of f_{sky} near to one, but as the fraction of sky covered increase this simple formula needs further corrections.

2.8.5 CMB surveys

When CMB was discovered in 1965 many ground based and high altitude balloon experiments tried to obtain its spectrum. The road for the study of the anisotropies was opened by NASA space missions. The first space mission dedicated to the study of CMB was launched in 1989: it was the Cosmic Background Explorer (COBE). For the first time it was possible to provide a detailed measurement of the CMB spectrum from the millimetre to the infrared region. The Far Infrared Absolute Spectrophotometer (FIRAS) covered the wavelength range from 0.1 to 10 mm in two spectral channels. COBE measured a nearly perfect blackbody spectrum, corresponding to a temperature of 2.726 ± 0.010K, with deviations from the blackbody form smaller than 0.03%. Beside the measurement of the spectrum, the objectives of COBE were to provide a full-sky map of infrared dust emission, and to map the deviations from isotropy over the sky. The instrument dedicated to the study of anisotropies was the Differential Microwave Radiometer (DMR), which operated in three band in the Rayleigh-Jeans region (31.5, 53 and 90 GHz) reaching an angular resolution of 7°, corresponding to l max $\sim$ 30. With this instrument, COBE measured the dipolar anisotropy due to our motion with respect to the cosmological reference frame, and achieved to detect anisotropies in the Sachs-Wolfe region of the power spectrum. The first complete map of small scale anisotropies on CMB sky was provided by the NASA WMAP mission (Wilkinson Microwave Anisotropy Probe). WMAP angular resolution was twenty times higher than COBE (12 arcmin, corresponding to l max $\sim$ 1000), it observed in five different frequencies (23, 33, 41, 61 and 94 GHz). It performed analysis of temperature and polarization distributions power spectrum, playing the key role in establishing the current Standard Model of Cosmology. The ESA Planck mission went beyond WMAP improving the angular resolution to 5 arcmin, corresponding to l max $\sim$ 3000. Its instrumentation worked in 9 different bands (30, 44, 70, 100, 143, 217, 353, 545, 857 GHz), allowing an unprecedented estimation of the sky brightness in these frequencies. Planck also used two different types of detectors. Radiometers at low frequencies (30-70 GHz) formed the so called Low Frequencies Instrument (LFI). The High Frequencies Instruments (HFI) covered instead the range 100-857 GHz. This combination of different detector technologies allowed for a tight control of instrumental systematics.

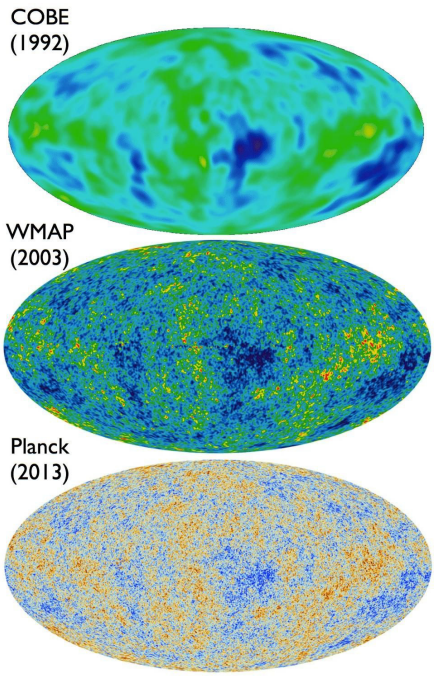

Figure 2.17: Comparison between the maps obtained with COBE, WMAP and Planck shows the increase of the resolution achieved in the last twenty years

2.9 CMB Anomalies

2.9.1 Introduction

Several unexpected features have been observed in the microwave sky at large angular scales, both by WMAP and by Planck. Those features in the CMB temperature anisotropies are individually observed as $2-3\sigma$ anomalies when testing the cosmological standard model [7]. Their detection opened a debate in the scientific community about their possible origin, their statistical relevance and their consequent impact on our cosmological scenario. One of the main assumption of our standard scenario is statistical isotropy. An analysis of the CMB anisotropies allows us not only to fit all free parameters of our cosmological model but also to test its underlying assumptions. Of course, the more fundamental the assumption, the harder it appears to test. The attention around the features individuated by WMAP and Planck is connected with the fact that they apparently violate statistical isotropy on the largest angular scales. Since this seems to happen only at the largest angular scales, it also amounts to a violation of scale invariance. It is worth noting that these anomalies can appear in the two point angular correlation

function and not in the power spectrum o viceversa but it doesn't affect their significance. From one side because the perfect equivalence between the information carried by these two statistical tools stands only if statistical isotropy is true and this is right the assumption that needs a test. On the other side because we know that changing between real and harmonic space can hide or reveal a real feature. In this case the two point angular correlation function assumes a new relevance: as opposed to the C_l of the power spectrum that are uncorrelated, $C(\theta)$ is dependent from $C(\theta')$ even for $\theta \neq \theta'$. Thus if a feature is attached to a certain region of the sky, or otherwise violates statistical isotropy, it may be much easier to spot it in the angular space than in harmonic space. In the table below the is a summary of the main anomalous feature revealed by WMAP and Planck [47].

features in angular space	p-value	data
low 2-pt correlation $S_{1/2}$	$\leq 0.5\%$	Planck 15
low 2-pt correlation $S_{1/2}$	$\leq 0.3\%$	Planck 13-wmap9
hemispherical variance asymmetry	$\leq 0.1\%$	Planck 15
cold spot	$\leq 1.0\%$	Planck 15
features in harmonic space	p-value	data
quadrupole-octopole alignment	$\leq 0.5\%$	Planck 13
l = 1, 2, 3 alignment	$\leq 0.2\%$	Planck 13
odd parity preference $l_{max} = 28$	< 0.3 %	Planck 15
dipolar modulation for $l = 2 - 67$	< 1 %	Planck 15

Lack of correlation

One of the discoveries of the first release of WMAP was that the two point angular correlation function at angular scales ≥ 60 degrees is unexpectedly close to zero, where a non-zero correlation signal was expected. The WMAP team suggested a simple statistic estimator to measure the vanishing correlation function:

$$S_\mu \equiv \int_{-1}^{\mu} d(\cos\theta)[C(\theta)]^2 \tag{2.155}$$

with $\mu \equiv \cos\theta = 1/2$. This measures the deviation from zero at $\theta \geq 60°$ Depending on the details of the analysis, p-values consistently below 0.5% have been obtained, some times even below 0.01%. Undoubtedly $S = 1/2$ is an *ad hoc* statistic but we will enter in the details of this problematic in the next chapter.

2.9.2 Alignments of the low multipole

In the standard ΛCDM model temperature (and other) anisotropies have random phases. In harmonic space this means that the orientations and shapes of the multipole moments are uncorrelated. In the first WMAP data release it was discovered that the octupole ($l = 3$) is nearly planar i.e dominated by $m = \pm l$ with a p-value of about 5%. The normal to the plane was found to be well aligned with the normal to the quadrupole plane (a quadrupole is always planar) at a p-value of about 1.5% [48]. Interestingly this plane is perpendicular to the Ecliptic and aligned with CMB dipole. Moreover these alignments are found to be exacerbated by proper removal of the kinematic quadrupole and no systematics or foregrounds have been identified to explain them.

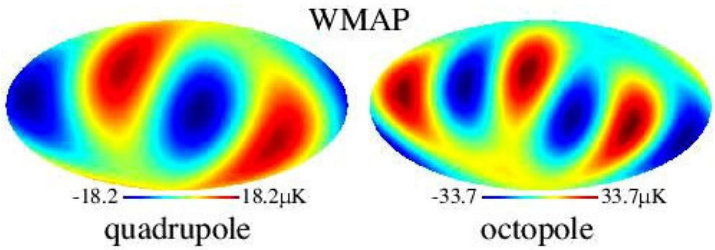

Figure 2.18: Alignment of quadrupole and octupole as seen in WMAP data

2.9.3 Hemispherical Asymmetry

Evidence for hemispherical power asymmetry first emerged in the analysis of WMAP first-year data [17]: it was found that the power in discs on the sky of radius $\sim 10° - \sim 20°$ evaluated in several multipole bins, is larger in one hemisphere on the sky than the other. The plane that maximizes the asymmetry is approximately the Ecliptic. The hemispherical power asymmetry is often interpreted as a dipolar modulation of the temperature field.

$$T(\hat{e}) = T_0(\hat{e})[1 + A\hat{e} \cdot \hat{d}] \tag{2.156}$$

where $T(\hat{e})$ and $T_0(\hat{e})$ are the modulated and unmodulated temperature field, $\bar{e}$ is an arbitrary direction on the sky, and A and $\bar{d}$ are the dipolar modulation amplitude and direction. The earlier analyses have found that $A \sim 0.1$ and direction $\hat{d}$ roughly points in the ecliptic pole direction. Planck also found that the modulation has most signal at relatively low multipoles, $l \in [2, 67]$ where it has a p-value of 1%.

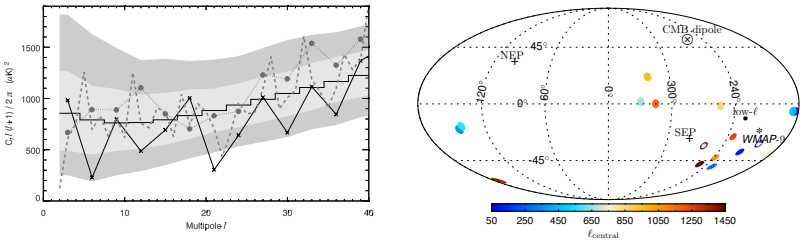

Figure 2.19: Hemispherical power asymmetry. Left panel: the three jagged lines show the binned angular spectrum over the whole unmasked sky (dashed), northern hemisphere (solid line), southern hemisphere (dotted line with circles). Northern and southern era defined with respect to the best fit axes for WMAP1 data. Right panel: best fit directions from the dipolar modulation model, applied to Planck 2015 maps, evaluated in multipole bins centered at 50 to 1450

2.9.4 Parity asymmetry

One question is whether the CMB sky is symmetric with respect to the reflections around the origin, $\hat{e} \to -\hat{e}$. The standard theory doesn't predict any particular behaviour with respect to point-parity symmetry. Because $Y_{lm}(\hat{e}) = (-1)^l Y_{lm}(\hat{e})$, even (odd) multipoles have an even (odd) symmetry. The point-parity symmetry analysis can be performed defining the two quantities [2]:

$$T^+(\hat{e}) = \frac{T(\hat{e}) + T(-\hat{e})}{2} \qquad T^-(\hat{e}) = \frac{T(\hat{e}) - T(-\hat{e})}{2} \tag{2.157}$$

and taking their ratio. This study found a 99.7% evidence for the violation of parity in WMAP7 data in the multipole range $2 \leq l \leq 22$. The analysis was confirmed by Planck which found that the significance peaks for $l_{max} \simeq 20 - 30$. The direction that maximizes this parity asymmetry is close to the direction of hemispherical asymmetry opening the question of a possible connection between the two anomalies. In figure (2.20) it is shown the parity asymmetry as function of the multipoles. The estimators used for this analysis are $P = P^+/P^-$ and Q:

$$P^+ = \sum_{l=2}^{l_{max}} [1 + (-1)^l] C_l/2 \qquad P^- = \sum_{l=2}^{l_{max}} [1 - (-1)^l] C_l/2 \tag{2.158}$$

$$Q(l_{odd}) = \frac{2}{l_{odd} - 1} \sum_{l=3}^{l_{odd}} \frac{C_{l-1}}{C_l} \tag{2.159}$$

Where $D_l = l(l+1)C_l/2\pi$

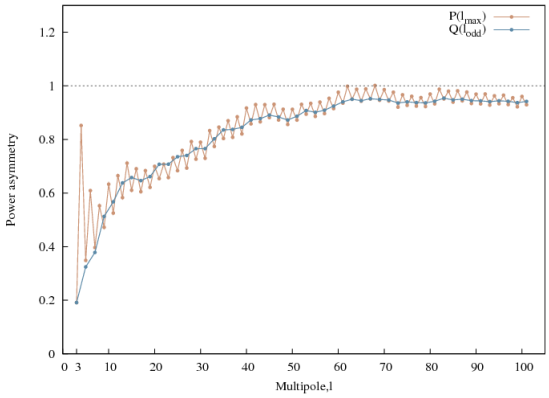

Figure 2.20: The even-odd multipole power asymmetry in the WMAP's seven year best fitting power spectrum in the multipole range $l = [2, 101]$ with P and Q estimators

2.9.5 Cold spot

In the WMAP first year data another anomaly was present which, opposite to the features described before, is localized. It is a large cold spot in the southern hemisphere of the CMB map, centered on angular coordinates $(l, b) = (207°, -57°)$ [13]. It has a radius of approximately five degrees, is roughly circular and the evidence for its existence is frequency independent. The intermediate size of the cold spot, combined to its frequency independence, seem to rule out the simplest systematic and foreground explanations. The size of the cold spot ($\sim 10°$) makes it too large to be a point source but too small to be a diffuse foregrounds. Moreover the frequency independence of the cold spot excludes the Sunyaev-Zeldovich effect. An alternative way to study this anomaly is to look for a connection between the cold spot and under-densities in the galaxy distribution [21]. A general way to do that is to cross-correlate the CMB temperature with the galaxy over-densities over the whole sky but those tests haven't yet been definitive.

2.9.6 Statistical relevance of CMB anomalies and possible explanations

Although most of the anomalous feature described in the previous chapter show p-values in the per cento or per mille level, none of them individually reaches the 5σ detection level that is adopted in some field of physics. To

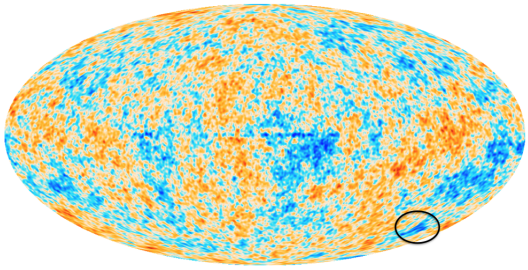

Figure 2.21: The cold spot in the southern hemisphere indicated with a black circle in Planck CMB map

address more in detail the issue of their statistical significance, it is worth asking whether features can have a common origin: of course their statistical independence would increase their significance within our cosmological scenario. Some studies [45][44] identify at least three independent anomalies: the lack of correlation on large scales (which can cause a low quadrupole and a low variance), the alignment of quadrupole and octupole, the dipolar modulations. Being their individual statistical relevance low, if just one of these three independent features had been observed it could have been classified as an unlikely event inside the framework of ΛCDM model, but their combined presence makes this hypothesis less strong even if still possible. A further treatment of the problem is given in the next chapter, for the moment we just want to mention some possible explanation for the presence of these anomalies in the case in which we state their existence has some kind of relevant cosmological consequences.

Foregrounds

In this section are presented some effects of local physics that can be suggested as an explanation of all or part of CMB anomalies. We mention:

- *Solar system*: sources of microwave radiation can be the dust grains or the Kuiper Belt[14][23].

- *Milky Way*: along the galactic plane thermal dust is dominant and molecular lines from CO transitions contribute in various frequency bands [40].

- *Sunyaev Zeld'ovich* and *supernovae remnants* can play a role in the formation of localized features in CMB but only on small scales which are not of interest [37].

The major argument against a foreground related explanation of these anomalous features is the frequency independence of the observed anomalies [28]. Moreover explanations connected to errors in the foregrounds removal or systematic bias are unlikely because the anomalies have been revealed by at least two different missions with different instrumental set up and ways of acquisition and reduction of data.

Cosmology

Another possibility is that some or all of the anomalies have a cosmological origin. The possibilities are several:

- *kinetic effects*: Earth's motion through the rest frame of the CMB leads to higher-order effects on the observed anisotropy, which could in principle affect conclusions about the observed anomalies [28]. As already discussed above, these so-called kinetic effects have been studied for low multipole moments as well as for the highest multipole moments and both contribute to the final significance of the anomalies.

- *Local Large Scale Structure*: local structures, that translate into over/underdensities in the dark matter distribution within tens or few hundreds of megaparsecs, could in principle be responsible for some of the alignments. This class of explanations has the nice feature of producing large-scale effects since the small distance to us implies a large angle on the sky. One possibility is the late-time integrated Sachs-Wolfe effect, or, in the non-linear regime, the Rees-Sciama effect. The idea of an unusually large void in our vicinity has been proposed to explain the cold spot anomaly through ISW even if it is not confirmed yet [16] [18].

- *Primordial power spectrum.* This argument can be treated in two ways: breaking scale invariance or breaking isotropy. For the first we just mention the studies around inflationary models with the minimal period of slow roll that can cause breaking of the scale invariance at observational accessible scales [43], [9], [10]. The latter is connected to multifield theories of inflation. In alternative, to break the power spectrum isotropy some authors considered anisotropic inflationary models [1] or primordial non gaussianity [35] [26].

- *Topology*: a non-trivial topology of the Universe might in principal both lead to a lack of correlation at large angular scale and introduce alignments and/or asymmetries, while preserving a locally isotropic and homogeneous geometry [5], [3].

Even if all these cosmological explanations for CMB anomalies are interesting it is important to mention that the debate on their statistical significance is still open. In the next chapter we will deepen this subject relatively to one of these anomalies (the lack of power on large scales) to build a method aimed at making a definitive statement on the statistical relevance of one of these anomalies.

Chapter 3

Test implementation and results

3.1 Lack of magnitude on large scales

The main focus of this work is to build a test for the statistical significance of one of the large angle CMB anomalies: the lack of power on large scales. First it is better to introduce this anomaly setting some points about the evidences revealed by Plank and WMAP and about the statistical estimators used to measure this anomaly. The Cosmic Background Explorer Differential Microwave Radiometer (COBE-DMR) [49]first reported a lack of large-angle correlations in the two-point angular-correlation function, $C(\theta)$, of the cosmic microwave background (CMB). This discovery has been confirmed with different statistical relevance both by WMAP and Planck data. The angular two-point function at the largest angular scales is our most direct probe of the primordial seeds of structure formation. We expect the large angular scales to be a direct probe of cosmological inflation, which predicts statistically isotropic CMB temperature fluctuations generated by a scale-invariant power spectrum of primordial quantum fluctuations [34], [51], [22]. More precisely, the post-inflation particle horizon subtends $\theta > 60^\circ$ at $z < 4$ in the standard ΛCDM model. For this reason an anomalous behaviour of $C(\theta)$ on large scales can in principle be related to violation of statistical isotropy i.e. $\langle a^*_{lm} a_{l'm'} \rangle \neq \delta_{ll'}\delta_{mm'}C_l$. It means that in the analysis of this feature we can no longer consider perfect equivalence between the two point correlation function and the power spectrum as we will see in the development of the procedure to build our test. To explore the main evidences of anomaly in the two point correlation function we focus on figure (3.1). Two important observations can be made about $C(\theta)$ even from a qualitative point of view:

- None of the observational angular correlation functions visually match

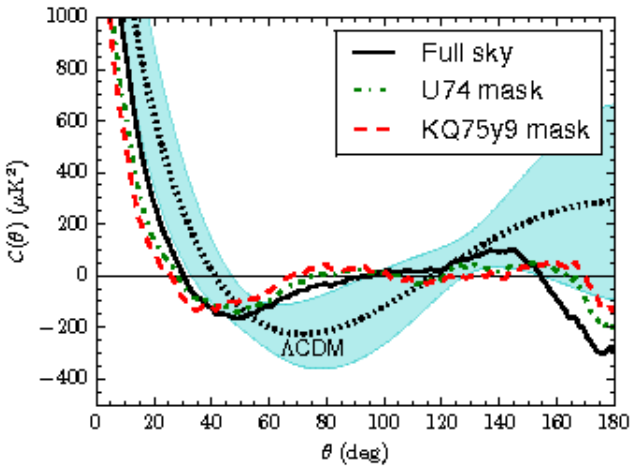

Figure 3.1: Two-point angular correlation function from Planck data. The black, dotted line shows the Planck best-fitting ΛCDM model. The shaded, cyan region is the one-sigma cosmic variance interval. The black, solid line is the $C(\theta)$ and two cut skies are obtained using the U74 mask (green, dash-dotted line) and the KQ75y9 mask (red, dashed line)

the expectations from the theoretical model.

- The most striking feature is that all the curves are very near to zero above about 60° , except for some anti-correlation near 180° .

Before we address these two questions, an important issue to consider is whether the extremely low large-angle correlations in the cut-sky WMAP maps are a general result of cutting the maps or is specific to the orientation of the cut. That is, we wonder if we should expect a loss of large-angle correlations in a cut-sky map or is the alignment of the cut with the Galaxy important. To address this question, in [11] Copi et al. performed an analysis based on five year WMAP results. It consisted in taking the full sky map and rotating it a very large number of times. On every rotated realization they applied the Galactic KQ75 mask, which was therefore randomly rotated relative to the original map. From their results it seems that the observed absence of large-angle correlations outside the KQ75 cut is due to the alignment of the Galaxy with the regions on the sky where such correlations are maximized. The little correlation above 60° stems from two specific regions within the Galactic cut covering just 9 per cent of the sky. It appears that our microwave background sky has anomalously low angular correlations everywhere outside the Galactic mask, but not within. If the region outside the cut is a reliable representation of the CMB, then we should focus on the

angular correlation for cut skies. The value of the large angle correlation there has a p-value of 0.025 per cent for the standard ΛCDM model.

Let us go back now to the first two questions: the discrepancy of the measured C_θ from the prediction of ΛCDM and its nearly null value on large scales. At least four explanations can be advanced to interpret these results:

- we don't live in a standard ΛCDM Universe with a standard inflationary early history;
- we live in an extremely anomalous realization of that cosmology;
- there are important errors in the observations of COBE, WMAP and also Planck;
- there are important errors in the reduction of COBE, WMAP and also Planck maps.

We don't enter in details with respect to a possible error in acquisition or reduction of data just because it is very unlikely that at least three experiments, with different systematics and different data processing can give us the same wrong result. Of course this consideration isn't enough to exclude these explanations but makes more justifiable for us to focus on the first two hypothesis. To deal with this problematic we first have to introduce some statistical estimators used to give a quantitative measurement of the anomaly.

3.1.1 Statistical estimators

We introduce here two main kind of statistical estimators: one is aimed at determining the discrepancy of the observed $C(\theta)$ with respect to ΛCDM, the other is suitable to measure the consistency of the two point angular function with zero. The distinction is important because while the discrepancy with our cosmological model may be an indication of statistical isotropy violation, a zero $C(\theta)$ implies that scales over 60° , which crossed the horizon below a redshift $z \sim 1.5$ are uncorrelated. For the first type one option is to compare the $C(\theta)$ inferred from the observed map to the $C(\theta)$ one expects from the theory. Thus one defines:

$$C^{th}(\theta) \equiv \frac{1}{4\pi} \sum_{l=0}^{\infty} (2l+1) C_l^{th} P_l(\cos(\theta)) \tag{3.1}$$

for the best fit values of the standard model, and compare it with the observed two point angular function observed:

$$N^{obs-\Lambda CDM} \equiv ||C(\theta) - C^{th}(\theta)|| \tag{3.2}$$

For the second type of statistical estimators we can propose a simple modification of the above formula:

$$N^{obs-\Lambda CDM} \equiv ||C(\theta) - 0|| \tag{3.3}$$

A variation of this simple estimator first proposed by WMAP team is called $S_{1/2}$. It is defined as an integral over the square norm of $C(\theta)$:

$$S_{1/2} = \int_{-1}^{1/2} [C(\theta)]^2 d(\cos(\theta)) \tag{3.4}$$

$S_{1/2}$ is a very simple statistic that can test the total amount of correlation at large angles. The last release of Planck collaboration calculated the value for $S_{1/2}$ and the associated p-value= 99.5. In this case the p-value is defined as the probabilities of obtaining values for the $S_{1/2}$ estimator on the Planck fiducial ΛCDM model at least as large as the observed values of $S_{1/2}$ on Planck 2015 temperature CMB maps.

3.2 A priori estimators

In the previous chapter we presented some of the most common estimators for the lack of power on large scales. These estimators allow for a quantitative measurement of the two point correlation function but they make a definitive statement on its statistical significance problematic. This because they are defined *a posteriori*. They actually have been defined after the first detection of COBE. Some authors argue that these estimators might have been a posteriori for COBE but the re-identification of the anomaly in WMAP and Planck raises them form the doubt to be *ad hoc* estimators. Nevertheless even Planck collaboration admits that the problem is only partially solved.
To go beyond we have to better define the question. When we try to make an assessment of the statistical significance of the lack of correlation on large scales we are actually doing an *hypothesis test*. The ΛCDM scenario, as every cosmological model, can't predict the precise universe that we observe, but a distribution of possible universes (intended as the value of every parameter is associated to its probability of happening predicted by the cosmological model). The presence of the anomalies may indicate that our universe is a rare realization of our standard cosmological paradigm or, in other words, it

represents a statistical fluctuation within the framework of the ΛCDM scenario. Hence the hypothesis we want to test is that we live in a rare statistical 'fluke' of ΛCDM model that casually presents those particular features in the CMB temperature correlation on large scales.
Once we have chosen the statement we want to prove we have to build the test. We have already seen that the measurement of the anomaly in the temperature correlation function is not useful for this purpose, since it is defined a posteriori. We need an *a priori* estimator that, calculated on data, enables us to make a definitive statement on the relevance of the anomaly. We now need to introduce in the analysis a new observable, correlated with temperature. The correlation allows us to predict statistically its behaviour and build an a priori test for the hypothesis.
The question is now how to create *correlated variables*. Of course the correlation is established by a physical mechanism inside the cosmological scenario. An example that will be useful later is that of CMB photon temperature and polarization: they are correlated because E-modes of polarization arise from quadrupole anisotropy in temperature. They are both random field so the matter is how to generate a correlated variable (i.e. polarization) from a Gaussian distributed variable (i.e. temperature anisotropy).

3.2.1 Correlated variables

If we want to generate n correlated Gaussian distributed random variables:

$$\mathbf{Y} \sim \mathcal{N}(\mu, \mathcal{M}) \tag{3.5}$$

where $Y = (Y_1 ... Y_n)$ is the correlated vector we want to obtain, $\mu = (\mu_1, ... \mu_n)$ the vector of the means and $\mathcal{M}$ the covariance matrix.

- first we need to simulate a vector of uncorrelated Gaussian random variables, $\mathbf{Z}$
- then we find the square root of $\mathcal{M}$ i.e. a matrix $\mathbf{C}$ such that $\mathbf{C}\mathbf{C}^T = \mathcal{M}$

The vector we look for is then

$$\mathbf{Y} = \mu + \mathbf{C}\mathbf{Z} \tag{3.6}$$

A common choice to calculate $\mathbf{C}$ is the *Cholesky decomposition* [24]. This kind of decomposition can always be applied to positive definite matrix. Symmetric $n \times n$ matrix A is a positive definite if the quadratic form $x^T A x$ is positive for all non-zero vectors x or, equivalently, if all the eigenvalues of A are positive. Positive definite matrices have many important properties,

not least that they can be expressed in the form $A = X^T X$ for a non-singular matrix X. The Cholesky factorization is a particular form of this factorization in which X is upper triangular with positive diagonal elements; it is usually written as $A = LL^T$ and it is unique. A variant of Cholesky factorization is the factorization $A = LDL^T$, where L is unit lower triangular (i.e., has unit diagonal) and D is diagonal. This factorization exists and is unique for positive definite matrices.

3.3 Healpix

Before we go into detail of the test we have built it is worth to describe the two libraries we use in our analysis: Healpix [20] and Master. Healpix was devised by Gòrski et al. to treat with those data sets that accumulate measurements distributed on the entire sky, or a considerable fraction thereof. Typical examples include radio, cosmic microwave background (CMB), sub-millimeter, infrared, X-ray, and gamma-ray sky maps of diffuse emission, and full-sky or wide-area surveys of extragalactic objects. In the CMB field science extraction from these data sets involves harmonic decomposition, estimation of the power spectrum, and higher order measures of spatial correlations.
The main difficulties of the treatment of this data sets consist in the analysis of function on a spherical domain. The numerical analysis of functions on the sphere involves

- a class of mathematical operations(i.e. Fourier analysis with spherical harmonics and power spectrum estimation) whose objects are discretized maps. A pixelized sky map is an intermediate, and often highly compressed, stage in the processing of data between the raw form acquired by instrumental detectors and the final stage of analysis resulting in estimates of typically a few values for the physical parameters of interest.

- the maps i.e., quantizations of arbitrary functions according to a chosen tessellation (an exhaustive partition of the sphere into finite area elements) A full-sky map provided by a CMB experiment contains:
  - signals coming from the sky, which are bandwidth-limited by the instrument's angular response function;
  - a projection into the elements of a discrete map, or pixels, of the observing instrument's noise; this pixel noise should ideally be random, and white, with a bandwidth significantly exceeding that of all the signals.

Starting from these points there are three main requirements for the mathematical structure of discrete full-sky maps:
-*Hierarchical structure of the database*. This is essential for very large databases. A simple argument in favor of this states that the data elements that are nearby in a multidimensional configuration space (here, on the surface of a sphere) should also be nearby in the structure of the database: this property facilitates various topological methods of analysis.
-*Equal areas* for the discrete elements of the partition. This is advantageous because white noise at the sampling frequency of the instrument gets integrated exactly into white noise in the pixel space, and sky signals are sampled without regional dependence (although care must be taken to choose a pixel size sufficiently small compared to the instrumental resolution to avoid pixel shape–dependent signal smoothing).
-*Isolatitude distribution* for the discrete area elements on the sphere. This property is essential for computational speed in all operations involving evaluations of spherical harmonics.

All these requirements are satisfied by the spherical tessellations structured as follows.

3.3.1 Pixel position

The sphere is initially partitioned into a number of curvilinear quadrilaterals, which constitute the base-level tessellation. Each element of partition is mapped onto a square so that a nested $n \times n$ subdivision of the square into sub-elements can be obtained trivially, and a hierarchical tree structure for the resulting database follows (which satisfies the first requirement). See figure (3.2)

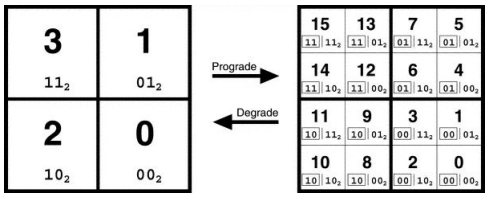

Figure 3.2: The coarsely pixelized coordinate patch on the left consists of 4 pixels. Two bits suffice to label the pixels. To increase the resolution, every pixel splits into 4 daughter pixels, shown on the right. These daughters inherit the pixel index of their parent (boxed) and acquire two new bits to form the new pixel index

Now analyze the base-level spherical tessellation. This construction is characterized by two parameters: N_θ is the number of base-resolution pixel layers between the north and south poles and N_ϕ the multiplicity of the meridional cuts. Obviously, the total number of base-resolution pixels is equal to $N_{pix} = N_\theta N_\phi$; the area of each one of them is equal to $\Omega_{pix} = 4\pi/(N_\theta N_\phi)$. this tessellation is shown in figure (3.3)

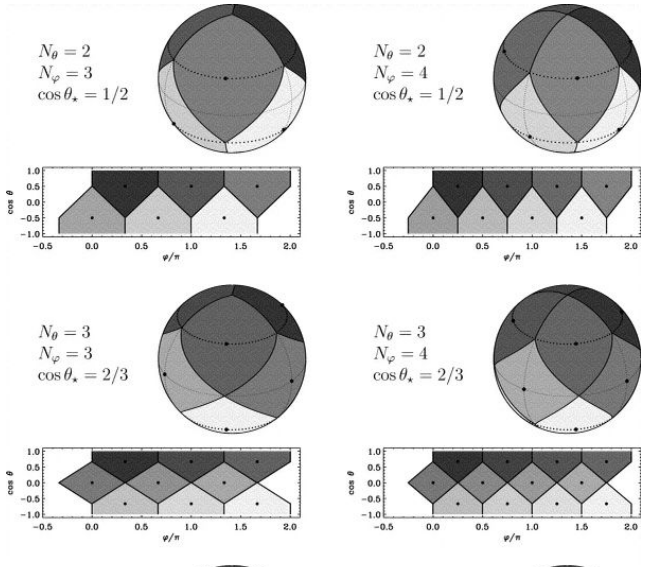

Figure 3.3: Several possible equal-area isolatitude tessellations of the sphere, which can support a hierarchical tree for the further subdivision of each large base-resolution pixel.

The HEALPix implementation is described by $N_\theta = 3$ and $N_\phi = 4$. The base resolution comprises 12 pixels in three rings around the poles and equator. The resolution of the grid is expressed by the parameter *Nside*, which defines the number of divisions along the side of a base-resolution pixel that is needed to reach a desired high-resolution partition. All pixel centers are placed on rings of constant latitude, and are equidistant in azimuth (on each ring). Orthogonal projections with different N_{side} era shown in figure (3.4)

3.3.2 Pixel indexing

HEALPix is allowed to support two different numbering schemes for the pixels.

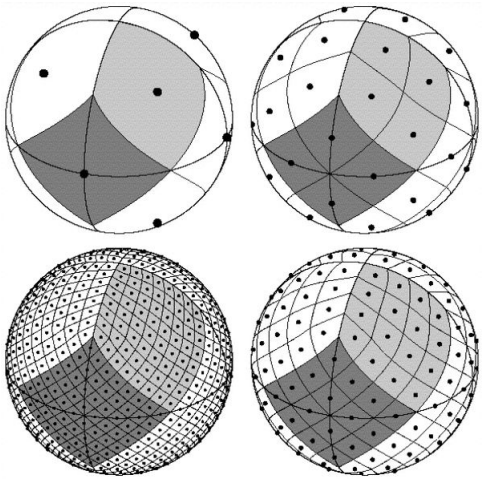

Figure 3.4: Moving clockwise from the top left panel, the grid is hierarchically subdivided with the grid resolution parameter equal to $N_{side} = 1$, 2, 4, 8, and the corresponding total number of pixels equal to $N_{pix} = 12 \times N_{side} = 12$, 48, 192, 768

- *ring scheme*: the pixels lie in isolatitude rings and one can simply count the pixels moving down from the north to the south pole on each ring. It is in this scheme that Fourier transforms with spherical harmonics are easy to implement.

- *nested scheme*: it is a tree structure of pixel numbering: it allows one to implement efficiently all applications involving nearest-neighbor searches

For a useful representation of the two pixel scheme see figure (3.5)

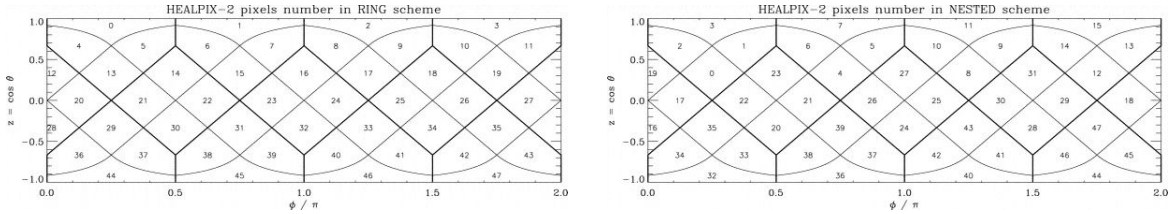

Figure 3.5: Layout of the HEALPix pixels on the sphere in a cylindrical projection and a demonstration of two possible pixel indexations: one running on isolatitude rings, the other arranged hierarchically or in a nested tree fashion.

3.3.3 Spherical projections

In this subsection we want to describe the law of HEALPix for mapping the surface of the sphere on a flat domain, and its inverse transformation. Consider coordinates (x_s, y_s), where x_s runs along the longitude and y_s runs along the latitude. We won't derive the mapping formulas but just mention them to show how HEALPix works. Then (x_s, y_s) are related to HEALPix ring number $i \in [1, 4Nside - 1]$ and pixel index j (on ring i) in the following way:

$$x_s = \left(j - \frac{s}{2}\right) \frac{\pi}{2N_{side}} \tag{3.7}$$

$$y_s = (2N_{side} - 1)\frac{\pi}{4N_{side}} \tag{3.8}$$

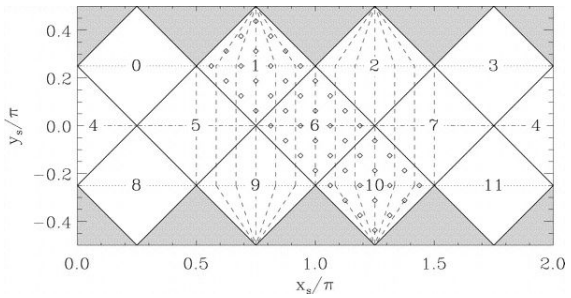

Figure 3.6: Spherical HEALPix projection onto the plane. Base-resolution HEALPix pixels (indexed here from 0 to 11, as in the HEALPix software) project into 12 identical square pixels in the plane. Hierarchical subdivision of the HEALPix grid generates identical square pixel images over the entire planar image of the HEALPix tessellation. Constant-latitude lines map into horizontal lines on the plane (dashed lines), and the HEALPix spherical projection mapping of meridians on one hemisphere is shown by the dashed lines.

3.3.4 Spherical harmonic transform

The requirement of an isolatitude distribution for all pixel centers was built into HEALPix in order for the grid to support fast discrete spherical harmonic transforms. The reason for the fast computational time of the harmonic transform (scaling as $\sim N_{pix}^{3/2}$) is geometrical: the associated Legendre function components of spherical harmonics, which can only be generated via slow recursions, have to be evaluated only once for each pixel ring. For

other grids that are not constrained to be isolatitude, extra computing time is wasted on the non optimal generation of the associated Legendre functions. This geometrical aspect is illustrate in figure(3.7)

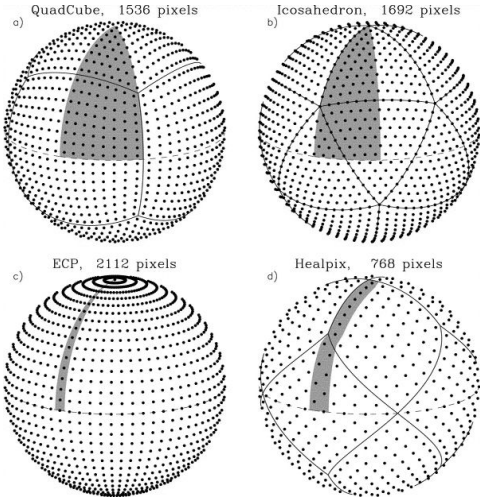

Figure 3.7: Comparison of HEALPix with other tessellations, including the QuadCube, icosahedral tessellation of the sphere, and ECP or "geographic grid." The shaded areas illustrate the subsets of all pixels on the sky for which the associated Legendre functions have to be computed in order to perform the spherical harmonic transforms.

3.4 Master

The second main numerical tool that we used is Master. It is necessary when we are working with a masked sky. We already saw in chapter 2.8.5 that the introduction of the mask complicates the analysis of the CMB maps because it introduces correlations between a_{lm} with different l and the Fisher matrix is no longer diagonal. From a computational point of view the problem is treated trough five steps that we will describe below. First it is necessary to apply the mask on the CMB map. The mask is a simple matrix whose entries can have only two values: 1 for the pixels that are observed, 0 for the pixels that are excluded. There are mainly two type of masks: the ones that cover localized sources as far galaxies and clusters, or galactic masks that cover all the Milky Way plane on the sky. The galactic masks are characterized by the fraction of the sky that remains observable.

Before applying the mask we must perform an operation called *apodization*. This is a kind of smoothing of the value of pixels around the discon-

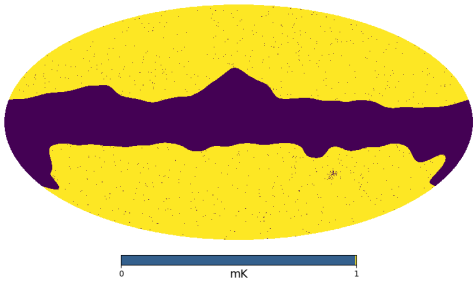

Figure 3.8: Mask of both the galaxy plane and the point sources. The fraction of the sky observable out of the galaxy cut is $f_{sky} = 0.7$

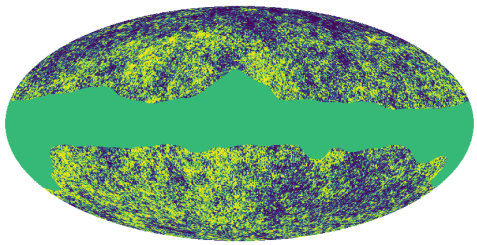

Figure 3.9: The CMB map is masked both for the galactic plane and the point sources. The resolution of the map is $N_{side} = 512$

tinuity among masked and non masked regions. It is necessary because the sharp transition between null and unitary values can cause calculation errors. There are essentially three types of apodization:

- apotype = C1: all pixels are multiplied by a factor f given by

$$f = \begin{cases} x - \sin(2\pi x)/2\pi & x < 1 \\ 1 & \text{otherwise} \end{cases} \tag{3.9}$$

  where $x \equiv \sqrt{(1-\cos\theta)/(1-\cos\theta_*)}$ and θ is the angular separation between the pixel and its closest masked pixel and θ_* is the apodization scale.

- apotype = C2: all pixels are multiplied by a factor f given by

$$f = \begin{cases} \frac{1}{2}[1 - \cos(\pi x)] & x < 1 \\ 1 & \text{otherwise} \end{cases} \tag{3.10}$$

  with x defined as in the previous case.

- apotype = Smooth. This type of apodization includes three steps: *i*) all pixel within a disc of radius $2.5\theta_*$ of a masked pixel are set to zero; *ii*)

the resulting map is smoothed with a Gaussian window function with a standard deviation $\sigma = \theta_*$; *iii*) the final step is to ensure that all pixels that were originally masked remain masked after the smoothing operation.

Once we have masked our CMB map, Master gives the opportunity to bin the initial power spectrum. In practice it performs this operation:

$$B_k = \sum_{l \in l_k} w_l C_l \tag{3.11}$$

Here the power spectrum is converted in a set of band powers B_k where w_l and l_k are the weights and the multipole ranges defining the binning scheme. For our purpose, as we will see later, we need all the power spectrum so we will set the bin range equal to unity. Once decided the binning scheme master corrects for the error introduced by the mask through the following operations:

- applying the mask on the CMB map
- compute the coupling matrix of the mask as defined in equation (2.146)
- compute the decoupled and de-biased band powers

$$B_k = \sum_{k'} (\mathcal{M})^{-1}_{kk'} \sum_{l \in l_{k'}} w_{l'} [\tilde{C}_{l'} - \tilde{C}^{cont}_{l'} - \tilde{C}^{noise}_{l'}] \tag{3.12}$$

where $\tilde{C}_l$ are the pseudo-cl to correct. $\tilde{C}^{cont}_{l'}$ and $\tilde{C}^{noise}_{l'}$ are referred to any contaminants and noise to subtract to the pseudo-cl. $\mathcal{M}$ is the binned decoupling matrix:

$$\mathcal{M}_{kk'} = \sum_{l \in l_k} \sum_{l \in l_{k'}} w_l M_{ll'} \tag{3.13}$$

It is important to mention that the application of the mask introduces nonphysical monopole and dipole in the spectrum and master removes them automatically. An alternative way to correct for the mask is to divide the power spectrum obtained for the fraction of the sky unmasked. The steps can be summed up in this way:

- 1) apply the mask to the temperature/polarization maps;
- 2) remove the nonphysical monopole and dipole generated by the application of the mask and mask again;
- 3) obtain the power spectrum

- 4) divide it for the fraction of the sky (in our case 0.75)

We present a preliminary comparison between these two methods. We considered WMAP best fit C_l and we created an ensemble of realizations of universe starting from this power spectrum, extracting a_{lm} and obtaining the relative maps. We then masked the maps and extract the power spectrum again correcting it before with master and then by dividing for fraction of the sky. The masked map needs to be apodized. This operations isn't as trivial as it seems: it causes a reduction of the effective fraction of the unmasked sky which has to be taken into account. Since the simulations are obtained considering until $l = 1000$ in the power spectrum the corresponding map is forced to have a quite high resolution ($N_{side} = 512$). At that N_{side} also point sources have to be masked. For this reason we used a mask which was the sum of a galactic mask and a point sources map. To explore the affects of apodization we tried two strategies: the first was to impose the apodization on all the masked regions (both the galactic and the point sources one), the second was to apodize only the galactic plane. In the first case the scale of apodization had to be very small (we have chosen the lower limit of Master, 0.08) otherwise it would cover a region too large of the sky, in the second case we can choose a larger scale and we fixed 1°.
We compared the resulting power spectrum in three different configurations:

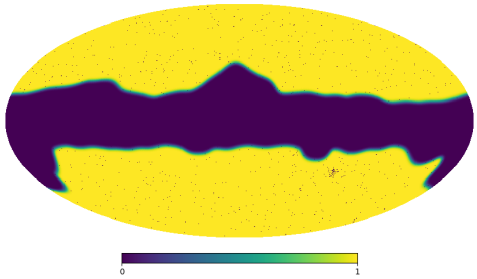

Figure 3.10: The CMB map is masked both for the galactic plane and the point sources with an apodization scale on the galactic plane of 1° The resolution of the map is $N_{side} = 512$

- figure (3.11) represents the absolute error between the pseudo-cl treated with master and f_{sky} with respect to the pseudo-cl full sky. It is simply calculated as the modulus of the difference between the mean value of the two on all the simulations

- figure (3.12) shows the ratio between the pseudo-cl corrected for the mask (both with Master and f_{sky}) and the uncorrected masked cl.

- figure (3.13) is the ratio between the pseudo-cl corrected for the mask (both with Master and f_{sky}) and the full sky pseudo-cl.

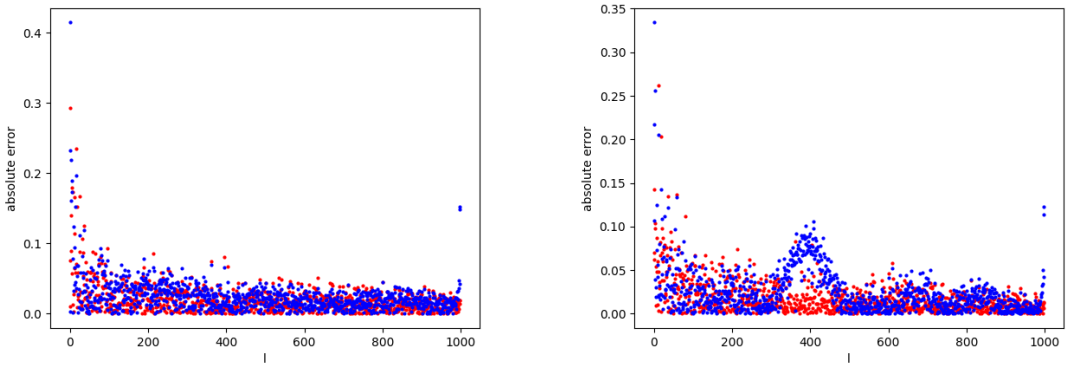

Figure 3.11: Absolute error for f_{sky} (blue) and Master (red) pseudo-cl with respect to full sky pseudo-cl. The left plot is obtained with an apodization scale of 1° only on the galactic plane, while the right one is obtained with an apodization scale of 0.08° on all the masked region

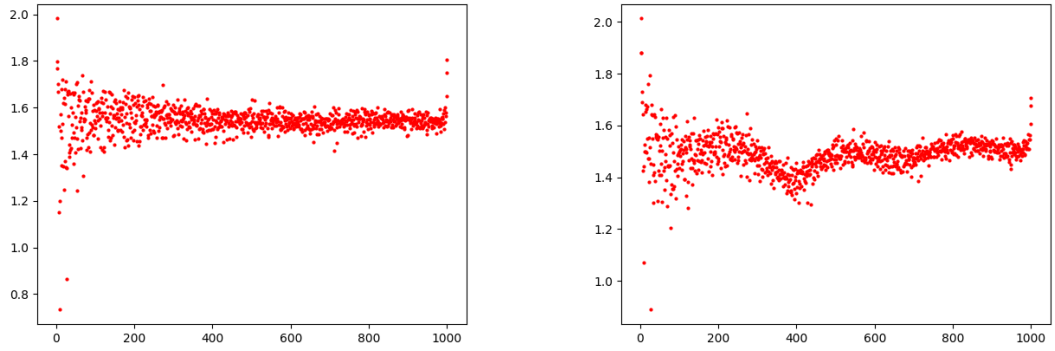

Figure 3.12: Ratio of f_{sky} (blue) and Master (red) corrected pseudo-cl with respect to uncorrected masked pseudo-cl.The left plot is obtained with an apodization scale of 1° only on the galactic plane, while the right one is obtained with an apodization scale of 0.08° on all the masked region

From the right panel of figure (3.12) we can see that apodizing the mask out of the galactic plane requires a more complicated correction to be applied to the pseudo-cl. While master is able to apply this correction, the simple division for f_{sky} isn't enough and this reflects in the pattern of errors we

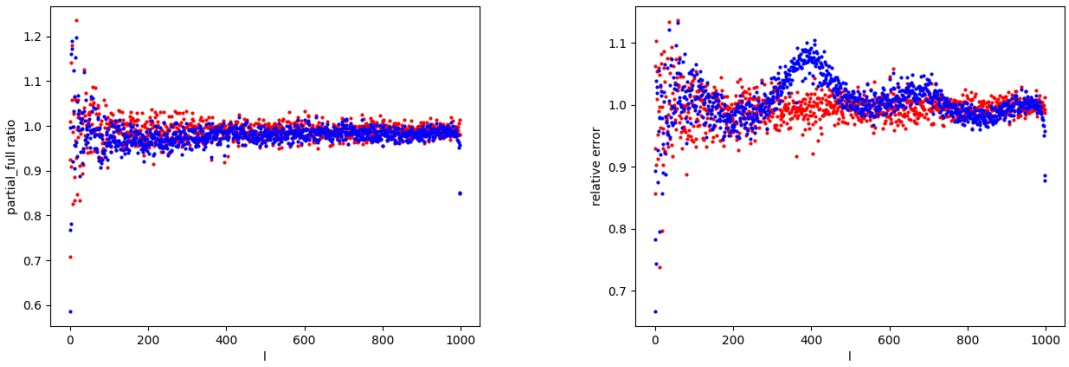

Figure 3.13: Ratio of f_{sky} (blue) and Master (red) corrected pseudo-cl with respect to full sky pseudo-cl.The left plot is obtained with an apodization scale of 1° only on the galactic plane, while the right one is obtained with an apodization scale of 0.08° on all the masked region

can see from the right panel of figure (3.11). In the following steps of our work we always used the galactic plane apodization of 1°. In this case even if master remains more reliable we can still use also the f_{sky} correction and see the effects it has on the result of our test, stressing that different methods of masking the sky have not negligible effects on the process of determination of the statistical relevance of a particular anomaly.

3.5 Constrained realizations

As already mentioned, the main target of this work is to build an a priori test of the hypothesis that we live in a ΛCDM universe that casually present an unlikely low value of the correlation function on large scales i.e. our universe is a rare statistical realization of the standard cosmology. We started from the paper "Large-angle CMB suppression and Polarization Predictions" [12] and followed the procedure proposed by Copi et al.. They have chosen as correlated observable the E-modes of CMB photons polarization and built their test on WMAP 7-years C_l. In our work we extended the procedure to WMAP 9-years and Planck's C_l. In this section we describe the procedure followed to build the test.

(i) In the standard ΛCDM model our Universe is a realization drawn from an ensemble. The width of this distribution is the cosmic variance, which represents the theoretical error associated to our cosmological model. However

once measured our realization is precisely determined. To test our hypothesis we are not interesting in realization of the *full* ΛCDM model, which means realization randomly extracted by an ensemble built around the best fit C_l. Rather than we are interested in realizations of the universe we observe i.e. forced to have the property of the two point angular correlation function measured by Planck and WMAP: these are called *constrained realizations*. To do that at the moment we can focus on the power spectrum: in a following step we will introduce also a condition on the two point correlation function. We generate an ensemble of realization of universe Gaussian distributed around the C_l of WMAP and Planck. The variance of the distribution of values obtained is made only by the part of the error associated to the noise and not the cosmic variance: this because the coefficients of the power spectrum we want are not randomly drawn from a χ^2 distribution but are constrained to reproduce the power spectrum that we observe.

ii) The C_l generated in the previous step contain the statistical information about the power in each mode consistent with the WMAP observations. To proceed with the analysis we need a map i.e an ensemble of a_{lm}. We remember that the expression for the pseudo-cl estimator is:

$$\frac{1}{2l+1}\sum_{l=-m}^{m}|a_{lm}^{T}|^2 = C_l^{TT} \tag{3.14}$$

In this case the C_l^{TT} in the expression are *exactly* the values generated from the previous step. As the C_l we generate are precisely what we observe and are not drawn from a chi-square distribution, the a_{lm} will not be randomly drawn from a Gaussian distribution: their values will be instead constrained by the expression (3.14).

iii) We have already mentioned that we have to impose a condition also on the two point angular correlation function: if this procedure is aimed to test the ΛCDM hypothesis we can't assume statistical isotropy and, as a consequence, we can't consider the information held by the power spectrum to be completely equivalent to that of the two point angular correlation function. For this purpose we use an a prior information that we already have: the value of the correlation on large angular scales has to be small and, as a consequence, the value of the statistical estimator $S_{1/2}$ has to be low. If we calculate the value of the estimator on all our constrained simulations we obtain a distribution of values. Being the lack of power a $2-3\sigma$ anomaly we can decide to save only the simulations that have a value of $S_{1/2}$ under the 2 or 3σ of such distribution. To reproduce a realistic case we consider the

value of the statistic calculated on the cut sky.

iv) Having now the constrained map in temperature (T) we need to build the correlated map in polarization, which means a set of correlated variable a^E_{lm} for every complete realization in T. The standard procedure to obtain a correlated variable, adapted to the specific case of temperature and polarization, gives:

$$a^T_j = \sqrt{C^{TT}_l}\zeta_1 \tag{3.15}$$

$$a^E_j = \frac{C^{TE}_l}{\sqrt{C^{TT}_l}}\zeta_1 + \sqrt{C^{EE}_l - \frac{(C^{TE}_l)^2}{C^{TT}_l}}\zeta_2 \tag{3.16}$$

where ζ_1 and ζ_2 are random variables and C^{TT}_l, C^{TE}_l, C^{EE}_l are the one of the best fitting ΛCDM model.
This procedure needs an adjustment in the case of constrained variables. The a^T_j can no longer be considered a random variable as in the case of equation (3.15) but they have to be right the $a^{T_{const}}_{lm}$ calculated from equation (3.14). Equation (3.16) then become:

$$a^E_j = \frac{C^{TE}_l}{C^{TT}_l}a^{T_{const}}_{lm} + \sqrt{C^{EE}_l - \frac{(C^{TE}_l)^2}{C^{TT}_l}}\zeta_2 \tag{3.17}$$

with ζ_2 still a Gaussian random variable.

v)The final step is to build the a priori estimator. This is now possible because we can forecast the behaviour of the CMB photon polarization, thanks to the correlation with the temperature anisotropies. The estimator chosen is very similar to the simple $S_{1/2}$.

$$S^{TQ}(\theta_1, \theta_2) \equiv \int_{\cos\theta_1}^{\cos\theta_2} [C^{TQ}(\theta)]^2 d(\cos\theta) \tag{3.18}$$

We can write the two point angular correlation function $C^{TQ}(\theta)$ in terms of the power spectrum C^{TE}_l characterized by the rotationally invariant modes E.

$$C^{TQ}(\theta) = \sum_2^\infty \frac{2l+1}{4\pi}\sqrt{\frac{(l-2)!}{(l+2)!}}C^{TE}_l P^2_l \cos\theta \tag{3.19}$$

The estimator can be written as:

$$S^{TQ}(\theta_1, \theta_2) = \sum_{ll'} C^{TE}_l I_{ll'}(\theta_1, \theta_2) C^{TE}_{l'} \tag{3.20}$$

where the expression for the matrix $I_{ll'}$ is calculated recursively as shown in appendix B of [12]. This procedure has been followed in four cases: for 20000 and 100000 initial realizations both for WMAP 9-year and Planck C_l. Every case includes the comparison between the results in the case of full and masked sky. In the case of masked sky, once obtained the polarization constrained map, we used Master to mask the sky and calculate the new pseudo-cl on which we calculated the value of the estimator.

3.6 WMAP 9-years

The first analysis that we present has been built on 20000 and 100000 realizations based on WMAP 9-year C_l. WMAP team made available the error bars on the C_l dividing the cosmic variance and the noise contributes. Thus we generated 20000 (and then 100000) simulated power spectra Gaussian distributed around the value of WMAP using for each C_l a variance of the distribution equal to the noise measured by the survey. Then we want to obtained the constrained map of a_{lm}^T. We generate them as random complex number Gaussian distributed with zero mean and unitary variance. Then we apply the condition (3.14) for the C_l of all the simulations. In this way we obtain a set of temperature maps each of them uniquely linked to the power spectrum of one of the constrained realizations. Having the maps we can apply the mask to cover the galaxy plane. The mask chosen has a $f_{sky} = 0.70$. Through Master then we can extract the pseudo-cl from that cut sky maps. On this simulated power spectrum we calculated the $S_{1/2}$ estimator and plot the distribution of the values obtained. We also calculated the value of the estimator on an equal ensemble of simulations of universe obtained from the the best-fit ΛCDM C_l. Unlike before these realizations are simply generated trough a Healpix function that allows to pass from the power spectrum to the a_{lm} map. In this way we take into account cosmic variance obtaining a simulation *full* ΛCDM. The result is in figure (3.14). It is clear that the constrained simulation distribution is far more sharp, being the correlation function forced to have low values. Now we have to impose the condition on $C(\theta)$ as we explained in the point *iii*) of the previous section. We find the 2σ of the constrained distributions and keep the simulations with a value of the estimator lower than this. The 2σ values (in unit of μK^4) for the calculated distributions are:

20000 realizations	100000 realizations
2330.852	2272.1905

Of course the condition on the correlation function would be more sig-

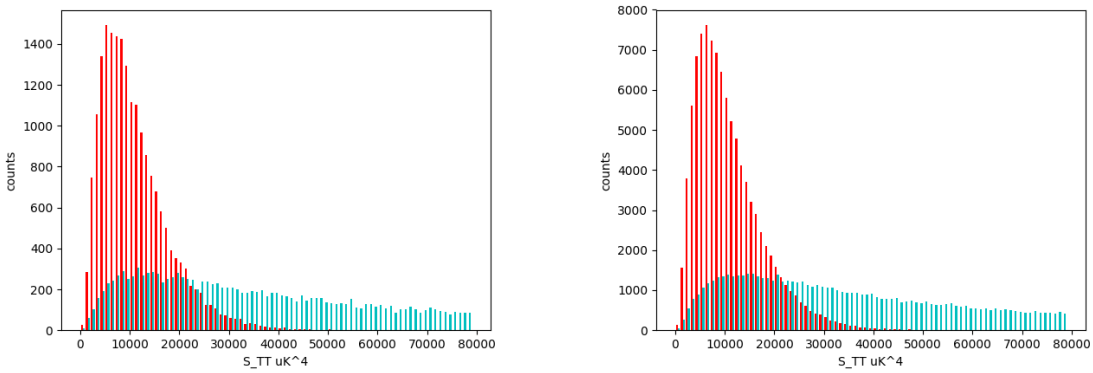

Figure 3.14: Estimator $S_{1/2}$ calculated on constrained simulation (red) and on full ΛCDM (cyan). The picture on the left contains 20000 simulation and the one on the right 100000

nificant if imposed on 3σ. In that case however we should have had a much higher number of initial simulations to make sure that realizations remaining after the cut are enough to go through with our statistical analysis (remember that the lower tail of 3σ represents the 0.15% of the total ensemble while 2σ the 2.5%). We limited the number of initial simulations for computational reasons. An optimization of the calculation time as well as the use of more performing computers are possible developments of the present work.

Having the constrained simulations we can calculate the correlation function (using equation (2.95)) for the pseudo-cl full sky and those obtained with Master and the f_{sky} correction. We matched them with the $C(\theta)$ of a comparable ensemble of realizations full ΛCDM. The result is plotted in figure (3.15). The full sky and partial sky curves for constrained realization are in good agreement and, contrary to the best fit ΛCDM simulations, the constrained realizations show a nearly zero correlation on large scales. It can be compared with the result of the literature [11] in figure (3.16)

The next step to build the test is to follow the procedure presented in point *iv*) of section (3.5) to extract the correlated maps in polarization. Their number is 500 in the case of 20000 initial simulations and 2500 in the case of 100000 initial simulations. Here we included a check on the a^E_{lm} obtained. It consists in a comparison between the standard deviation error bars and the error on the standard deviation itself. For every multipole l,m we calculated the standard deviation (trough a python function) among the simulations. We also calculate the standard deviation on the a^T_{lm} among the simulation and

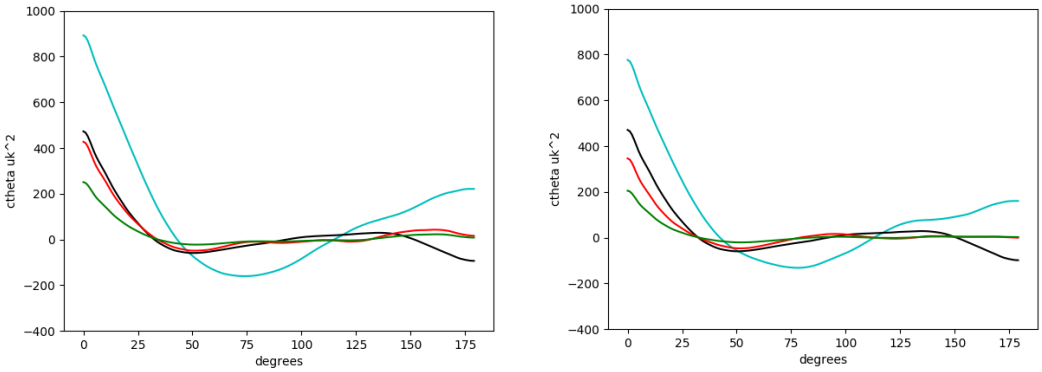

Figure 3.15: In the figure we see full ΛCDM correlation function (cyan), $C(\theta)$ from constrained realizations full sky (black) and $C(\theta)$ from constrained realizations masked sky treated with Master (red) and f_{sky} correction (green) for 20000 (left) and 100000 (right).

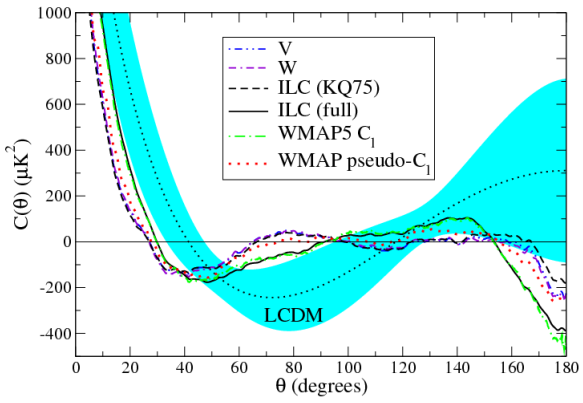

Figure 3.16: In the figure we can see the expected curve of the two point angular correlation function given by simulations best fit standard model and the one obtained from the measurements of the correlation function in the sky both for full sky and for cut sky. The shaded region corresponds roughly to the cosmic variance.

propagate the error. The difference between these two quantity represents the error bar and it has to be compared with the error on the standard deviation of a_{lm}^E itself. Call the standard deviation obtained with Healpix

stdv we have:

$$\text{error bar} = stdv(a^E_{lm}) - \sqrt{\left(\frac{C^{TE}_l}{C^{TT}_l}\text{stdv }(a^T_{lm})\right)^2 + \left(C^{EE}_l - \frac{(C^{TE}_l)^2}{C^{TT}_l}\right)\text{stdv}(\zeta_2)^2} \tag{3.21}$$

while the error on the standard deviation is:

$$\text{error stdv} = \frac{stdv(a^E_{lm})}{\sqrt{(2 * (\text{Nsim}) - 1)}} \tag{3.22}$$

and Nsim is the total number of simulations for both the cases. See figure (3.17)

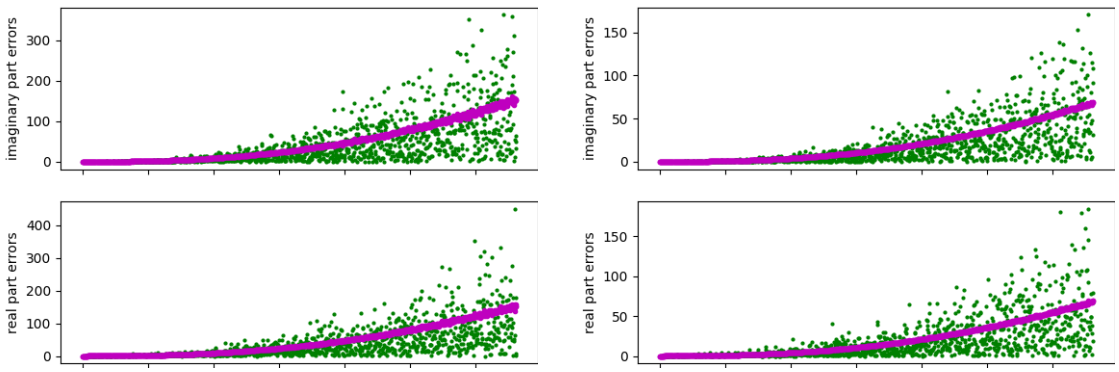

Figure 3.17: The figure represents the comparison between the error bars (magenta) and the standard deviation error(green). On the x axes the multipoles l,m are in succession for simplicity while the y values are multiplied for $l(l+1)/2$. The left panels are referred to the case with 20000 simulations and the right panels to that with 10000. Top panels refers to the imaginary part of the a^E_{lm} while bottom panels to the real part. All the figures shows that the at list the 68% of the errors are within the error bars, confirming that the values we are obtaining are consistent.

Once we have our maps in polarization we have to mask them. We proceeded in the two ways described in the section 'Master'. We apply Master choosing an apodization scale of 1° and apodization type *Smooth*. The correction for f_{sky} kept into account that the apodization reduced the effective fraction of the sky unmasked. We approximate the effective fraction of the sky calculating the ratio between the sum of the non zero value of the mask and its length: it resulted to be $f^{(eff)}_{sky} = 0.63$.
The comparison between the two methods is in figure (3.18). We plotted

the mean difference between the pseudo-cl full sky and those obtained with master and the difference between the pseudo-cl full sky and those obtained dividing by the fraction of the sky.

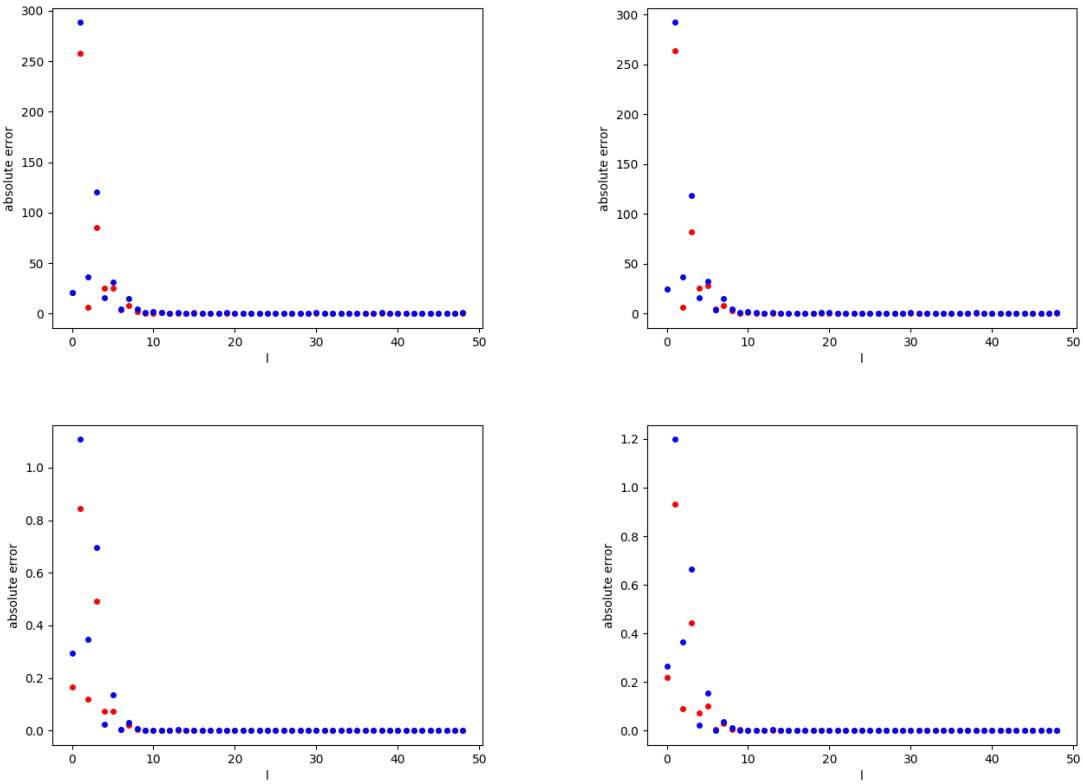

Figure 3.18: The top panels represent the absolute errors on the temperature pseudo-cl obtained with Master (red) and through the division for f_{sky} (blue) for 20000 (left) and 100000 (right). The bottom panels represent the same quantities but for the temperature-polarization pseudo-cl

Figure (3.18) clearly shows two main evidences:

- both the methods have large error on low l i.e. large angular scales;
- the use of the simple division for the fraction of the sky is much less precise than Master.

We were now ready to implement the a priori statistical estimator on our simulations. As it is clear from equation (3.20) the estimator is flexible, allowing to change the integration extreme i.e. to change the scales on which

to test the lack of power. We have applied it both for the usual extreme $60° - 180°$, that were first used in the definition of $S(1/2)$, and for another ranges of angles $48° - 120°$, suggested by the article from which we started for this work. The reason will be better explain later and have to deal with the *constraining power* of the statistic. As we have done at the beginning with temperature realizations, we plotted the distribution of the value of the estimator calculated on the constrained realizations and on a comparable ensemble of simulations obtained from the best fit ΛCDM C_l.

In figure (3.19) and (3.20) the panels show the distribution of the value of the estimator calculated on the constrained realizations (red) and on a comparable ensemble of simulations (green) obtained from the best fit ΛCDM C_l respectively for full sky, cut sky (pseudo-cl divided for f_{sky}) and cut sky (pseudo-cl treated with Master).

From these plots we can draw some considerations:

- every panel shows that the two distributions peak nearly in the same value but the best fit ΛCDM C_l distribution is much more broaden and present a long tail with higher values than the constrained statistic. Between the three cases we can make a distinction. The statistic calculated on full sky pseudo-cl and Master pseudo-cl are in good agreement one with the other. The distribution of the estimators on pseudo-cl divided for f_{sky} is instead a little bit sharper with respect to the others.

- For both 20000 and 100000 simulations the constrained distributions are sharper for the angle range $48° - 120°$ than for the usual range $60° - 180°$.

The comparison of the shape of the estimators distribution between the constrained simulations and the best fit ΛCDM C_l realizations has a key role in this test. To understand why we should explain how an hypothesis test works. Such a kind of procedure allows us to exclude or confirm an hypothesis to a certain "level of confidence" that is chosen a priori. In our case the test can't confirm the hypothesis that we live in a rare fluctuation of the standard cosmological scenario but just exclude this statement at some confidence level. Let's say that we chose as confidence level 3σ. We can calculate the value of three sigma on the distribution of the estimator for the constrained realizations. Of course some of the best fit ΛCDM simulations will fall beyond the 3σ of the constrained distribution, since their distribution is broader. For these simulations the value of the estimator is not compatible

with the range of values that we expect given the observed temperature power spectrum and the temperature and polarization correlation: in these cases the hypothesis of the statistical fluctuation of ΛCDM is excluded. We can now simply define the *constraining power* of the statistic as the percentage of cases in which the standard cosmological scenario is excluded. It is important to note that, as opposite, this test says nothing about the simulations within the confidence level: in those case we can't exclude the hypothesis of the statistical fluctuation but we can't even confirm it. Now we will expose the procedure followed for Planck C_l and then we will compare the constraining power obtained for Planck and WMAP trying to understand the effect of the mask and the choice of the angles range.

3.7 Planck

The procedure followed on Planck power spectrum is very similar to that of WMAP. We just mention some slight differences. First: when we generated the constrained simulations in temperature we needed the noise. This has been obtained averaging the noise power spectrum extracted from 100 simulations of noise maps that Planck team made available. We have chosen to use the band of 143 GHz cause it is quite clean from contaminant. In the plot (3.22) and (3.23) we show the power spectrum of the noise and its effect when summed to that of the temperature anisotropies.

Having the noise we could generate the constrained realizations in temperature. Again we generate the maps of a_{lm} and apply the condition (3.14). Once obtained in this way the constrained maps we have to mask them and extract again the power spectrum with Master. The next step, as already seen, is to calculate the value of the estimator $S_{1/2}$ on the constrained power spectrum of all the simulation. Indeed we need the value of the 2σ of the estimator distribution to impose a condition on $C(\theta)$. The value of the 2σ in μK^4 is in these cases:

20000 realizations	100000 realizations
2529.647	2502.71

We selected the constrained simulations with a value of $S_{1/2}^{cut}$ lower than that of the two sigma.
Also in the case of Planck we calculated the two point angular correlation function for an ensemble of simulations best fit ΛCDM and for a constrained ensemble both full sky and partial sky. The result is shown in figure (3.25) and shows the same behaviour described for WMAP .

To proceed with the test we have to pass from the maps in temperature to the correlated maps in polarization calculating the a^E_{lm}. In this case too we did the check described in the previous section, obtaining the plots (3.26).

Now we had the full sky maps in temperature and polarization and we wanted to cover the galactic plane (both for the 20000 and 100000 initial simulations). We followed the same procedure of the previous section obtaining the pseudo-cl both with Master and by dividing the masked pseudo-cl for the fraction of the sky covered. We then calculated the relative error of these pseudo-cl with respect to the full sky pseudo-cl both in the case of temperature and polarization. With plots (3.27) we showed again that the errors on the pseudo-cl got through the division for f_{sky} are higher that the one treated with Master.

At that point we were ready to implement the a priori statistical estimator on our simulations. Again we have applied the estimator both for the extremes $60° - 180°$ and for the couple of angles $48° - 120°$ suggested by the article from which we started for this work. We plotted the distribution of the value of the estimator calculated on the constrained realizations and on a comparable ensemble of simulations obtained from the best fit ΛCDM C_l. We also plotted the comparison between the distribution of the estimator on constrained cut and full sky to underlying the effect of applying a mask on the pseudo-cl.

From a qualitative point of view the considerations that can be done on the distributions of the estimator values on the simulations generated from Planck C_l are very similar to those already exposed for WMAP. The comparison between the distribution of the estimator on the constrained full sky and on the cut sky pseudo-cl as shown in the first panel of figure (3.29) confirms the result of the literature that the application of the mask makes the statistic more sharp. In [11] is reported the result that more conservative is the mask more significant is the anomaly. In our plots the statistic is more sharp in the case in which we corrected the pseudo-cl dividing for f_{sky}. We interpreted this fact assuming that the effective fraction of the sky we used is maybe an overestimation of the real one. Another possible explanation is that the simple correction for f_{sky} reflects in errors in the calculation of the power spectrum that affect the final shape of the statistic.

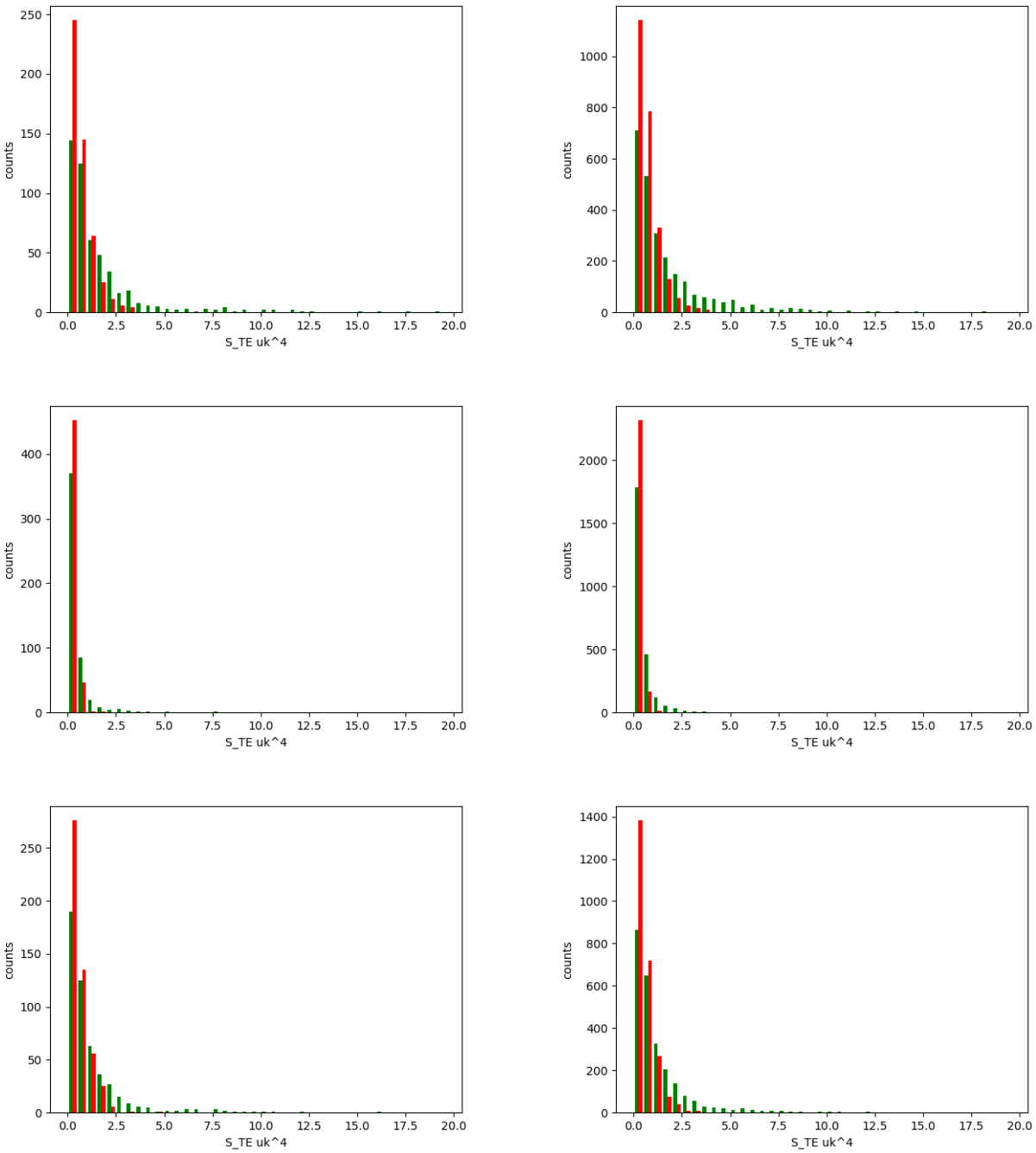

Figure 3.19: The plots are for 20000 simulations (left) and 100000 (right).These plots are obtained calculating the estimator between the usual extreme $60° - 180°$ on WMAP power spectrum.

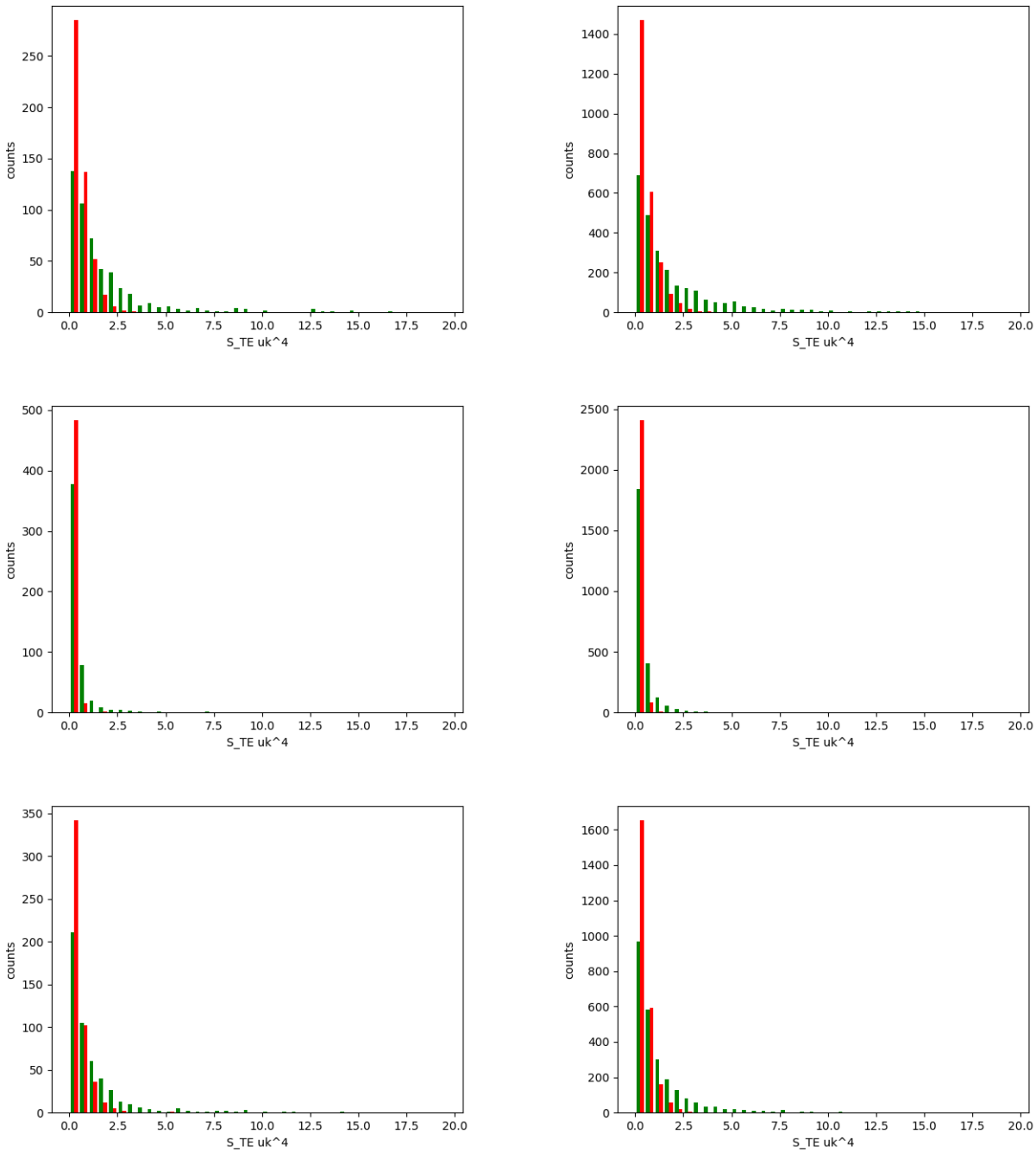

Figure 3.20: The plots are for 20000 simulations (left) and 100000 (right).These plots are obtained calculating the estimator between the extreme $48° - 120°$ on WMAP power spectrum.

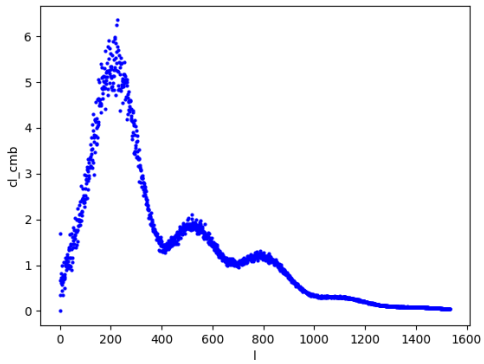

Figure 3.21: This plot shows the Planck power spectrum of CMB temperature anisotropies in unit of μK^2. The power spectrum is normalized with the factor $l(l+1)/2\pi$

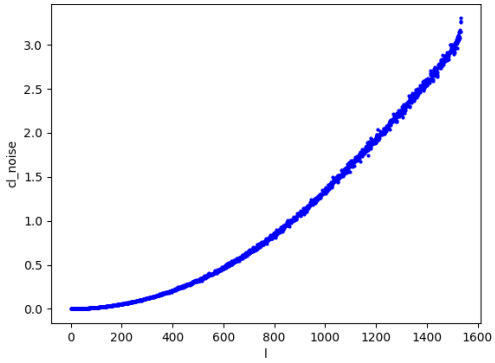

Figure 3.22: This plot shows the averaged noise power spectrum. The quantities on the y axis are multiplied by a factor 10^{-10}. We can see that, opposite to cosmic variance, noise tends to be more important for high l. Here too the power spectrum is normalized with the factor $l(l+1)/2\pi$

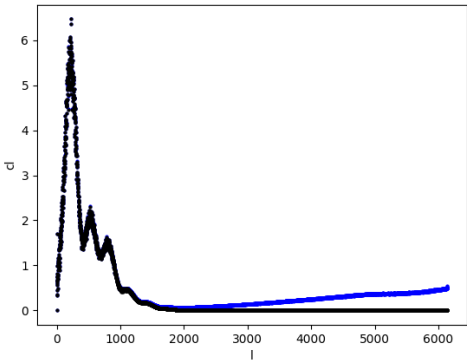

Figure 3.23: In this picture we see the effect of summing the CMB and noise power spectrum. Both are in unit of μK^2

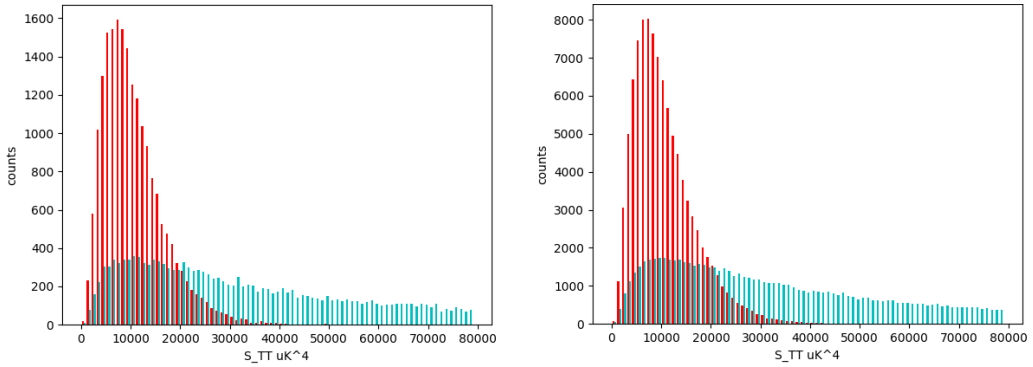

Figure 3.24: In the figure the distributions of the estimator $S_{1/2}$ calculated both on the constrained realization and on an equal ensemble of simulation of the full ΛCDM universe starting from Planck observed and best fit power spectrum.

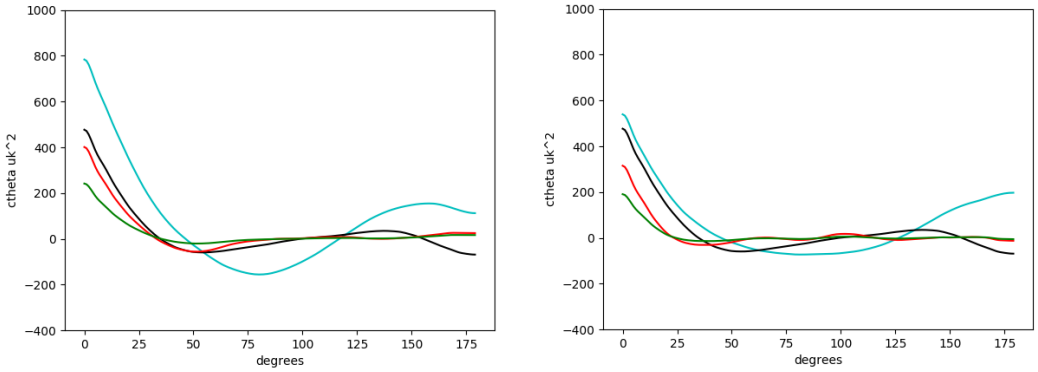

Figure 3.25: In the figure we see full ΛCDM correlation function (cyan), $C(\theta)$ from constrained realizations full sky (black) and $C(\theta)$ from constrained realizations masked sky treated with Master (red) and corrected for f_{sky} (green) for 20000 (left) and 100000 (right) simulations.

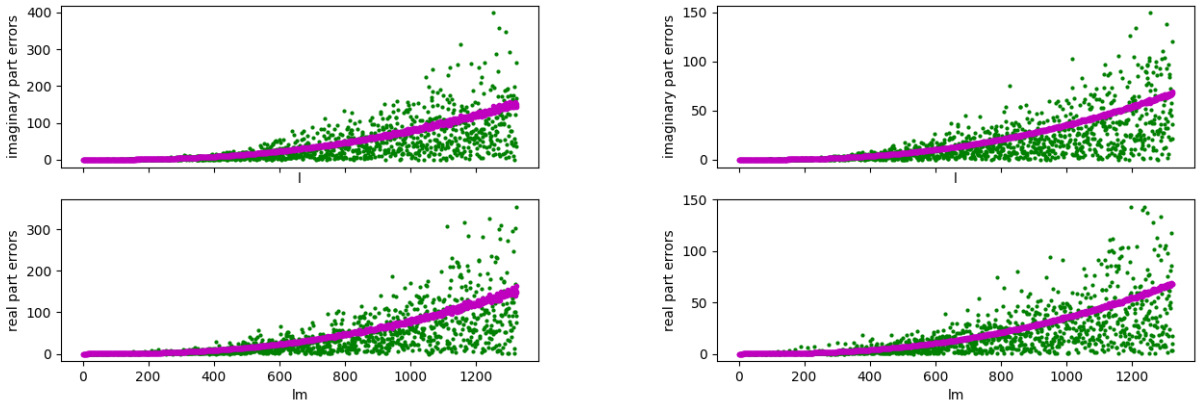

Figure 3.26: The figure represents the comparison between the error bars (magenta) and the standard deviation error (green). On the x axes the multipoles l,m are in succession for simplicity while the y values are multiplied for $l(l+1)/2$. The left panels are referred to the case with 20000 simulations and the right panel to that with 10000. Top panels refers to the imaginary part of the a^E_{lm} while the bottom panels to the real part. All the figures shows that the at list the 68% of the errors are within the error bars, confirming that the values we are obtaining are consistent.

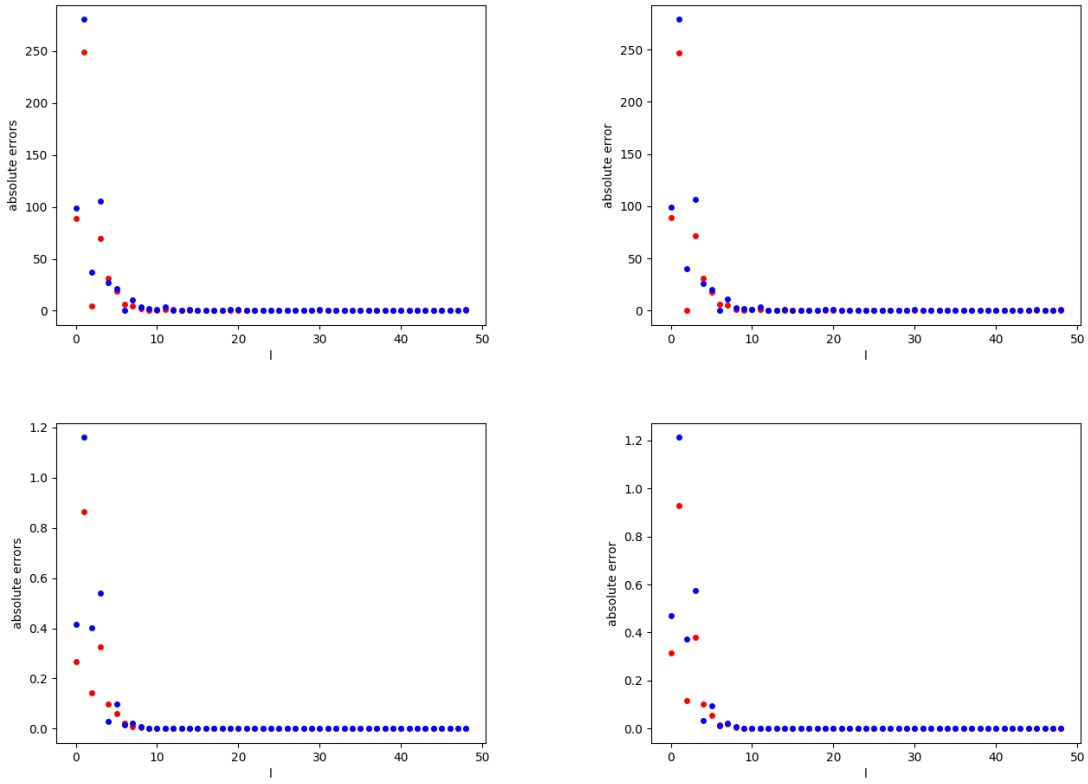

Figure 3.27: The top panels represent the absolute errors on the temperature pseudo-cl obtained with Master (red) and through the division for f_{sky} (blue) for 20000 (left) and 100000 (right). The bottom panels represent the same quantities but for the temperature-polarization pseudo-cl

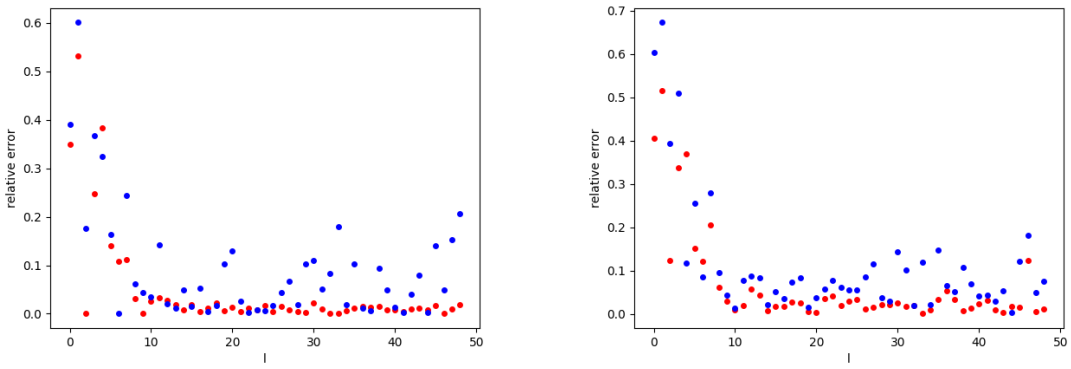

Figure 3.28: The top panels represent the relative errors on the temperature pseudo-cl obtained with Master (red) and through the division for f_{sky} (blue) for 20000 (left) and 100000 (right) simulations.

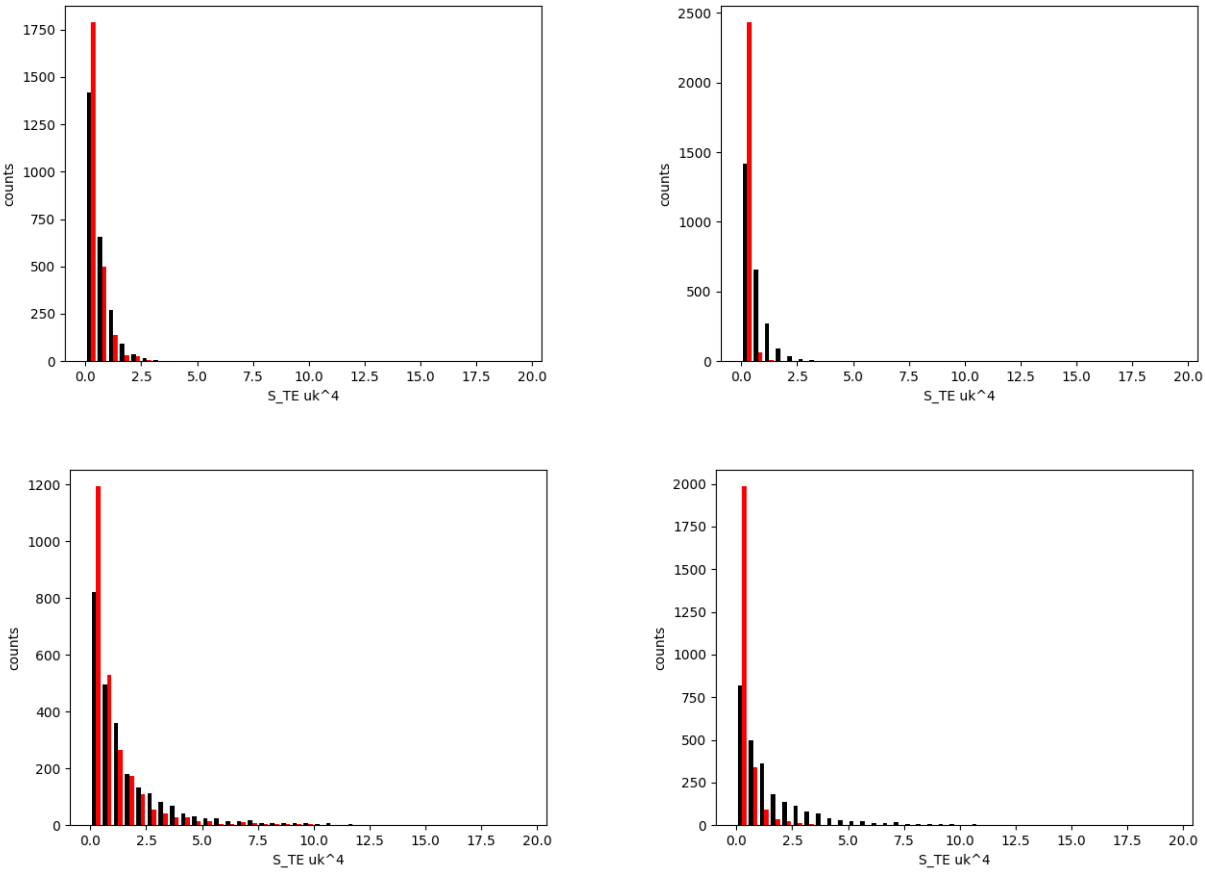

Figure 3.29: The left panels represent the comparison between the distribution of the estimator calculated on cut sky treated with Master (red) and full sky (black). The right ones represent the comparison between the distribution of the estimator on cut sky corrected for f_{sky} (red) and full sky (black). In the top panels the distributions are calculated on a constrained ensemble of simulations while in the bottom panels the distribution are those of an ensemble of full ΛCDM realizations. All the plots are for 100000 initial simulations from Planck power spectrum

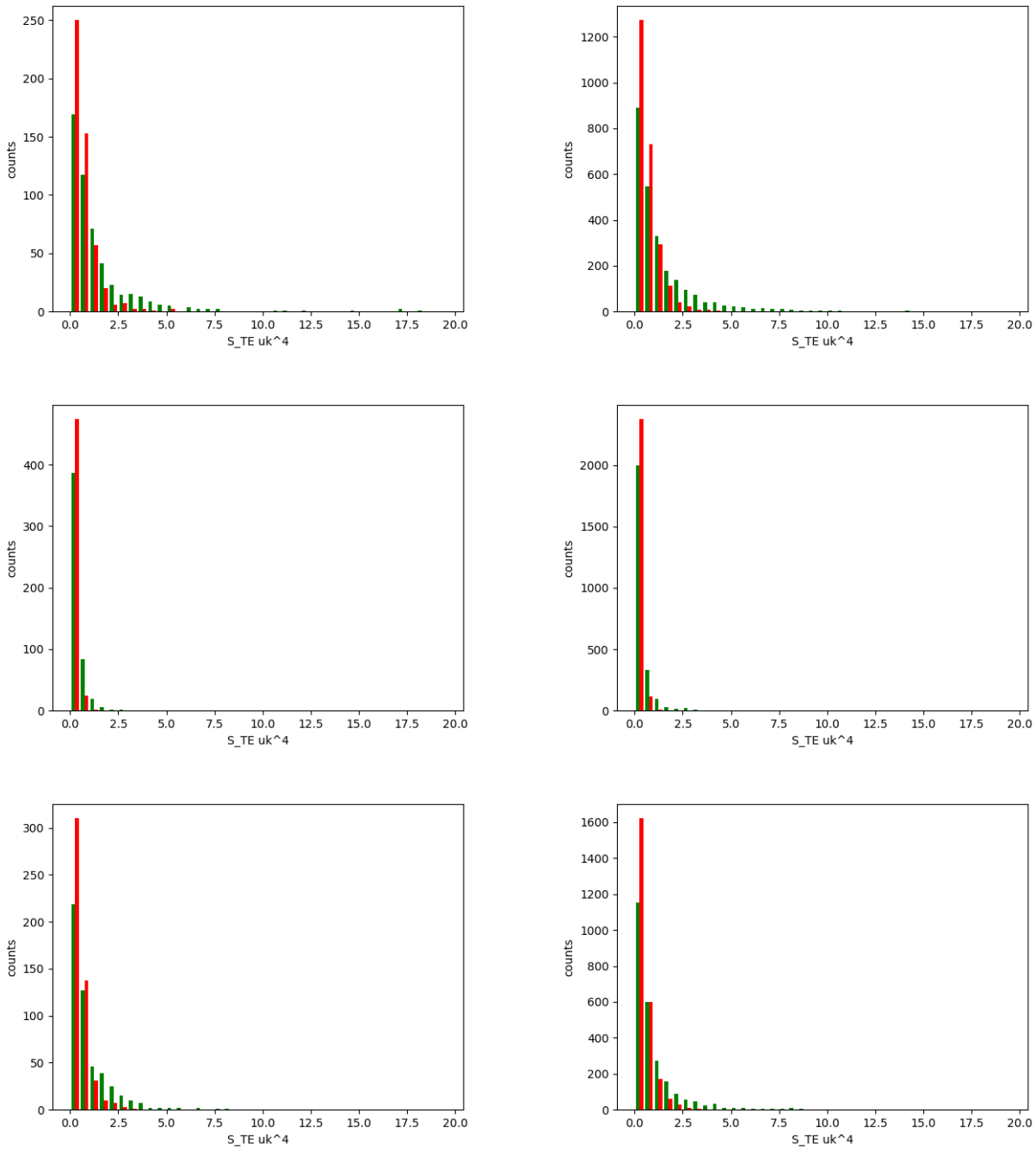

Figure 3.30: The plots are for 20000 simulations (left) and 100000 (right). These plots are obtained by calculating the estimator between the usual extreme $60° - 180°$. The panels shows the distributions of the value of the estimator calculated on the constrained realizations (red) and on a comparable ensemble of simulations (green) obtained from the best fit ΛCDM C_l respectively for full sky, cut sky (pseudo-cl divided for f_{sky}) and cut sky (pseudo-cl treated with Master) from Planck power spectrum.

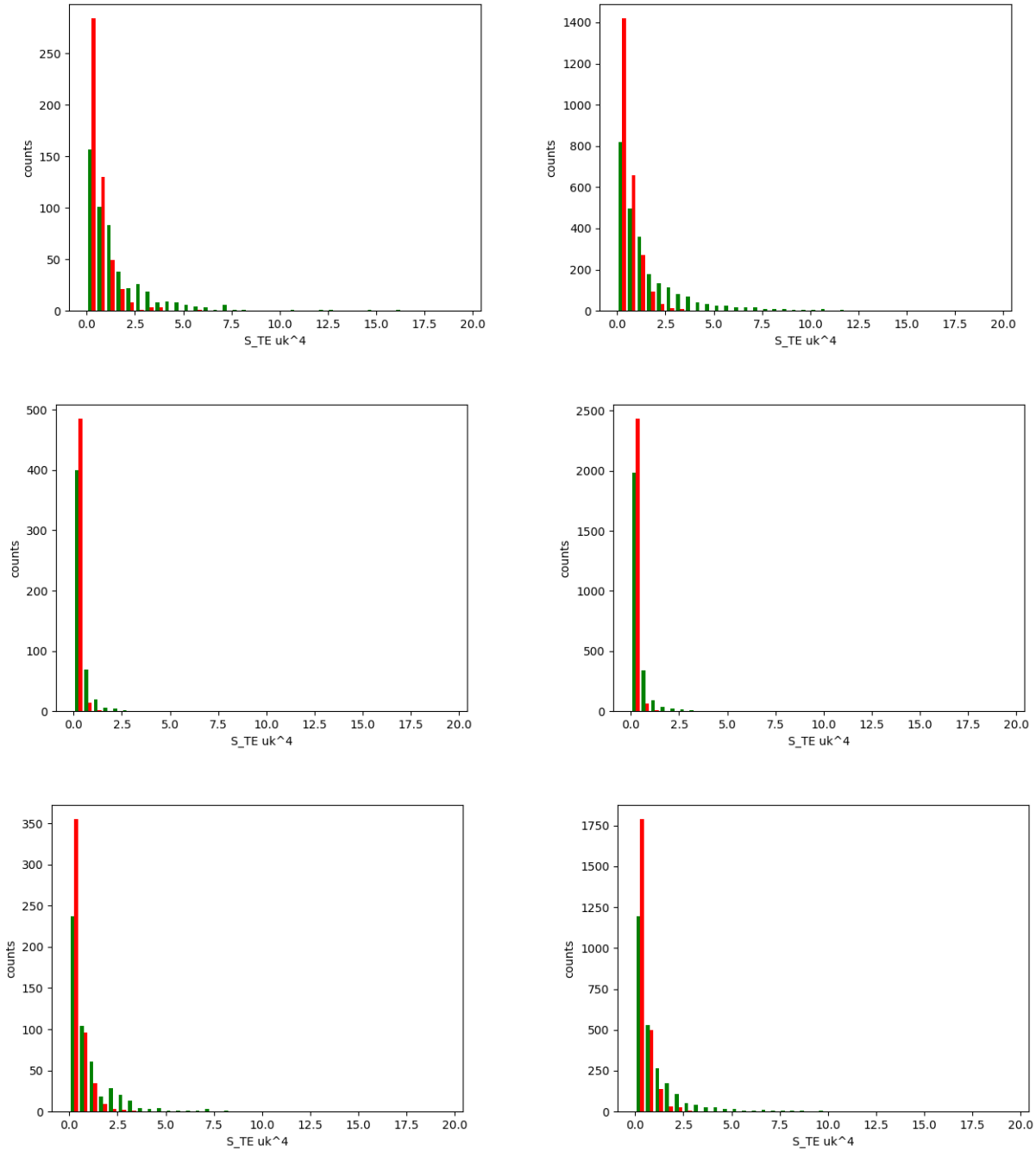

Figure 3.31: The plots are for 20000 simulations (left) and 100000 (right). These plots are obtained by calculating the estimator between the extreme $48° - 120°$. The panels show the distribution of the value of the estimator calculated on the constrained realizations (red) and on a comparable ensemble of simulations (green) obtained from the best fit ΛCDM C_l respectively for full sky, cut sky (pseudo-cl divided for f_{sky}) and cut sky (pseudo-cl treated with Master) from Planck power spectrum.

Chapter 4

Results and future perspectives

In the tables below we sum up the main results extracted directly from the distribution of the estimator calculated on the constrained realizations.

S_{Planck}(60°-180°) 100000 realizations	median μk^4	3σ μk^4	discriminating power %
full sky	0.488	4.272	7
Master	0.363	3.355	5
f_{sky}	0.136	1.198	4
S_{Planck}(48°-120°) 100000 realizations	median μk^4	3σ μk^4	discriminating power %
full sky	0.423	3.778	10
Master	0.287	3.128	6
f_{sky}	0.097	1.012	6
S_{Planck}(60°-180°) 20000 realizations	median μk^4	3σ μk^4	discriminating power %
full sky	0.501	5.247	3
Master	0.383	2.956	5
f_{sky}	0.147	1.089	4
S_{Planck}(48°-120°) 20000 realizations	median μk^4	3σ μk^4	discriminating power %
full sky	0.427	4.334	7
Master	0.321	2.785	7
f_{sky}	0.108	0.915	8

S_{WMAP9}(60°-180°) 100000 realizations	median μk^4	3σ μk^4	discriminating power %
full sky	0.557	4.444	11
Master	0.446	3.471	7
f_{sky}	0.169	1.187	7
S_{WMAP9}(48°-120°) 100000 realizations	median μk^4	3σ μk^4	discriminating power %
full sky	0.416	3.771	15
Master	0.344	3.676	7
f_{sky}	0.117	1.198	7
S_{WMAP9}(48°-180°) 20000 realizations	median μk^4	3σ μk^4	discriminating power %
full sky	0.518	3.171	13
Master	0.445	3.461	7
f_{sky}	0.167	1.165	8
S_{WMAP9}(48°-120°) 20000 realizations	median μk^4	3σ μk^4	discriminating power %
full sky	0.416	2.955	16
Master	0.330	3.485	7
f_{sky}	0.109	1.153	7

From the values reported in these tables we can draw some considerations:

- the median value for WMAP (mediated on the four cases treated) in μK^4 is 0.477 ± 0.071 (full sky) and 0.391 ± 0.058 (Master). For Planck 0.459 ± 0.039 (full sky) and 0.339 ± 0.048 (Master). Those values are compatible with each other.

- the median value in μK^4 of the pseudo cl divided for f_{sky} is 0.122 ± 0.025 for Planck and 0.141 ± 0.030 for WMAP. These values are lower than the previous one following what we said before about the distribution of the estimator which becomes far more sharp.

- the value of the three sigma for the Master pseudo-cl of WMAP9 (100000 simulations) is 3.461 (48°-120°) μK^4. Taking into account that in the article it results that the 99.9 % of the simulations have a value of the estimator below 2.195 μK^4, we can say that our statistic is much more broaden. Our explanation of this lies in the choice to use the simulations in temperature that had a value of $S_{1/2}$ below the two sigma of the distribution. This decision was imposed by computational limits but resulted to be not enough constraining affecting not only the value of 3σ but also the discriminating power of the statistic as written below.

- the discriminating power of the statistic for Master and full sky pseudo-cl on average is far below the one obtained by the author of the article we refer to (that obtained the 25.6% at 99.9% of confidence level). Moreover the constraining power we have calculated is referred to 3σ which is a quite mild confidence level. Nevertheless we can make some considerations. The power of the statistic to exclude the fluke hypothesis isn't influenced significantly by the number of simulations. It is instead affected by the range of angles between which the estimator is evaluated. We confirm the result of the authors that the power of the statistic increases in the angles range (48°-120°).

4.1 Future perspectives with Planck

To conclude we would give some more justifications about the choice to repeat the procedure used for WMAP also on Planck power spectrum. It derives from the consideration that this test can give definitive results only if it involves the use of data. Once calculated the value of the estimator on data, it can be compared with the distribution of the constrained simulations. If data will show a value of the estimator larger than the chosen confidence level, let's say at least 3σ, of the constrained distribution, we can say that this value isn't allowed from the prevision we can make using our observed temperature power spectrum and the correlation between temperature and polarization. It means that the initial hypothesis of being in a rare statistical fluctuation of ΛCDM model is contradicted by polarization data. But using data requires to keep into account of the error associated to the noise of the measurements. There are mainly two procedure to introduce the measurement error: the first is to add it in the constrained simulations and the second is to associate an error bar to the value of the estimator calculated on data. The first procedure is more correct if the purpose is to do an hypothesis test: the uncertainties are included in the distribution while the estimator on data result to be a pure number whose position with respect to the chosen confidence level of the distribution determines the result of the test. This procedure is complicated and we will leave it as a future development of the present work. We tried instead a hybrid approach which consisted in associating an error bar to the value of the estimator on data and compare it with the constrained distribution calculated on simulations free of errors. Of course the threshold for the detection of the anomaly has to take into account of the presence of the error bar: if the error bar is smaller we can eventually claim the existence of the anomaly at a higher confidence level. Our aim now is to derive the general formula for the error on the polarization-temperature cross-correlation power

spectrum and then propagate the error to calculate the uncertainty on the statistical estimator. We want to compare the value of the error bars for WMAP and Planck and predict how much the threshold of the anomaly detection increases due to the supposed reduction of the error bars from WMAP and Planck experiments. Below we obtained the expression for the error on our statistical estimator delivering all the necessary assumption done in this procedure.
We express the power spectrum in term of the sum of signal and noise power spectrum.

$$C_l^{TE} = C_l^{(S)TE} + C_l^{(N)TE} \tag{4.1}$$

To simplify the notation we write the coefficient of the harmonic expansion as:

$$a_{lm}^T = T_{lm} \tag{4.2}$$

$$a_{lm}^E = E_{lm} \tag{4.3}$$

we want to calculate the error bars on the coefficient of the power spectrum in the case of white noise. In this way we can consider just the diagonal terms of the covariance matrix and $l = l'$. The variance of the C_l estimator is:

$$\sigma^{2(TE)} = \langle C_l^{TE} C_l^{TE} \rangle - \langle C_l^{TE} \rangle \langle C_l^{TE} \rangle \tag{4.4}$$

Introducing the expression of the estimator in the previous formula we get:

$$\begin{aligned}\sigma^{2(TE)} = &\frac{1}{(2l+1)^2} \sum_{mm'} \langle (T_{lm}^{S*} + T_{lm}^{N*})(E_{lm}^S + E_{lm}^N)(T_{lm'}^{S*} + T_{lm'}^{N*})(E_{lm'}^S + E_{lm'}^N) \rangle \\ &\frac{-1}{(2l+1)^2} \sum_{mm'} \langle (T_{lm}^{S*} + T_{lm}^{N*})(E_{lm}^S + E_{lm}^N) \rangle \langle (T_{lm'}^{S*} + T_{lm'}^{N*})(E_{lm'}^S + E_{lm'}^N) \rangle\end{aligned} \tag{4.5}$$

Now using the Wick's formula:

$$\langle \phi_1 \phi_2 \phi_3 \phi_4 \rangle = \langle \phi_1 \phi_2 \rangle \langle \phi_3 \phi_4 \rangle + \langle \phi_1 \phi_3 \rangle \langle \phi_2 \phi_4 \rangle + \langle \phi_1 \phi_4 \rangle \langle \phi_2 \phi_3 \rangle \tag{4.6}$$

and the relation:

$$a_{l-m} = a_{lm}^* (-1)^m \tag{4.7}$$

We can split the first term of (4.5) and find:

$$\begin{aligned}\langle (T_{lm}^{S*} + T_{lm}^{N*})(E_{lm}^S + E_{lm}^N)(T_{lm'}^{S*} + T_{lm'}^{N*})(E_{lm'}^S + E_{lm'}^N) \rangle = \\ + \langle (T_{lm}^{S*} + T_{lm}^{N*})(E_{lm}^S + E_{lm}^N) \rangle \langle (T_{lm'}^{S*} + T_{lm'}^{N*})(E_{lm'}^S + E_{lm'}^N) \rangle \\ + \langle (T_{lm}^{S*} + T_{lm}^{N*})(T_{l-m'}^S + T_{l-m'}^N) \rangle \langle (E_{lm}^S + E_{lm}^N)(E_{l-m'}^{S*} + E_{l-m'}^{N*}) \rangle \\ + \langle (T_{lm}^{S*} + T_{lm}^{N*})(E_{lm'}^S + E_{lm'}^N) \rangle \langle (E_{lm}^S + E_{lm}^N)(T_{lm'}^{S*} + T_{lm'}^{N*}) \rangle\end{aligned} \tag{4.8}$$

When we insert this expression in (4.5) we see that the first term of the Wick's expansion and the second term of (4.5), which is the product on the expected value of C_l^{TE}, cancel each other. We remain with:

$$\sigma^{2(TE)} = \frac{1}{(2l+1)^2}\sum_{mm'}[\langle(T_{lm}^{S*}+T_{lm}^{N*})(E_{lm'}^{S}+E_{lm'}^{N})\rangle\langle(T_{lm'}^{S*}+T_{lm'}^{N*})(E_{lm}^{S}+E_{lm}^{N})\rangle + \langle(T_{lm}^{S*}+T_{lm}^{N*})(T_{l-m'}^{S}+T_{l-m'}^{N})\rangle\langle(E_{lm}^{S}+E_{lm}^{N})(E_{l-m'}^{S*}+E_{l-m'}^{N*})\rangle] \tag{4.9}$$

Now we proceed doing all the products inside the four brackets. We do the assumption that the temperature and polarization noise are uncorrelated and hence some terms are zero:

$$E_{lm}^{S}E_{lm}^{N} = T_{lm}^{S}T_{lm}^{N} = 0 \tag{4.10}$$

$$T_{lm}^{S}E_{lm}^{N} = T_{lm}^{S}E_{lm}^{N} = 0 \tag{4.11}$$

$$T_{lm}^{N}E_{lm}^{N} = 0 \tag{4.12}$$

We are left with the expression:

$$\sigma^{2(TE)} = \frac{1}{(2l+1)^2}\sum_{mm'}[\langle T_{lm}^{S*}T_{l-m'}^{S}+T_{lm}^{N*}T_{l-m'}^{N}\rangle\langle E_{lm}^{S*}E_{l-m'}^{S}+E_{lm}^{N}E_{l-m'}^{N*}\rangle + \langle T_{lm}^{S*}E_{lm'}^{S}\rangle\langle T_{lm'}^{S*}E_{lm}^{S}\rangle] \tag{4.13}$$

$$\sigma^{2(TE)} = \frac{1}{(2l+1)^2}\sum_{mm'}[\langle T_{lm}^{S*}T_{l-m'}^{S}\rangle\langle E_{lm}^{S*}E_{l-m'}^{S}\rangle + \langle T_{lm}^{N*}T_{l-m'}^{N}\rangle\langle E_{lm}^{S*}E_{l-m'}^{S}\rangle + \langle T_{lm}^{S*}T_{l-m'}^{S}\rangle\langle E_{lm}^{N}E_{l-m'}^{N*}\rangle + \langle T_{lm}^{N*}T_{l-m'}^{N}\rangle\langle E_{lm}^{N}E_{l-m'}^{N*}\rangle + \langle T_{lm}^{S*}E_{lm'}^{S}\rangle\langle E_{lm}^{S}T_{lm'}^{S*}\rangle] \tag{4.14}$$

$$\sigma^{2(TE)} = \frac{1}{(2l+1)}[C_l^{TT(S)}C_l^{EE(S)}]\sum_{m-m'}\frac{\delta_{m-m'}}{2l+1} + [C_l^{TT(N)}C_l^{EE(S)}+C_l^{TT(S)}C_l^{EE(N)}+C_l^{TT(N)}C_l^{EE(N)}]\sum_{m-m'}\frac{\delta_{m-m'}}{2l+1} + \frac{1}{(2l+1)}[C_l^{TE(S)}]^2\sum_{mm'}\frac{\delta_{mm'}}{2l+1} \tag{4.15}$$

It can be split up in the error due to the noise and that to the cosmic variance:

$$\sigma_{noise}^{2(TE)} = \frac{1}{(2l+1)}[C_l^{TT(N)}C_l^{EE(S)}+C_l^{TT(S)}C_l^{EE(N)}+C_l^{TT(N)}C_l^{EE(N)}] \tag{4.16}$$

$$\sigma_{CV}^{2(TE)} = \frac{1}{(2l+1)}[C_l^{TT(S)} C_l^{EE(S)} + (C_l^{TE(S)})^2] \tag{4.17}$$

We used that $\sum_{m-m'} \delta_{m-m'}/(2l+1) = \sum_{mm'} \delta_{mm'}/(2l+1) = 1$ Having the errors on the measurements given by the noise of the experiment in equation (4.16) we can propagate the error on the estimator 3.20:

$$\sigma_{S_{1/2}} = \sqrt{\sum_{l'} \left(\sum_{l} \frac{\partial S_{1/2}}{\partial C_l} \right)^2 \sigma_{C_{l'}}^2} \tag{4.18}$$

$$\sigma_{S_{1/2}} = \sqrt{\sum_{l'} \left(2 \sum_{l} I_{ll'} C_l^{TE} \right)^2 \sigma_{C_{l'}}^2} \tag{4.19}$$

This is the final error bar to be associated to the value of the estimator calculated on our data. We calculated the value of the error bar for WMAP nine years and Planck 2015 in order to predict the increasing of the testing power of our statistical estimator when it will be applied on Planck data. Applying (4.19) we found:

$\sigma_{S_{TE}}$ WMAP	$\sigma_{S_{TE}}$ Planck
0.971	0.020

It is immediately clear that the error bar on the estimator decrease of a factor almost 50 from WMAP to Planck. Consider now that the value of the 3σ is 3.676 μK^4 for WMAP (100000 simulations) and 3.128 μK^4 for Planck (100000 simulations). We impose now that the threshold for our detection is 3 times the error bar i.e. we claim the anomaly if the value of the estimator in data is higher than the 3σ of the constrained distribution plus three times its error bar. It means that the statistic on WMAP will find anomaly for value higher than 6.589 μK^4 while Planck will detect the anomaly for value higher than 3.188 μK^4. The constraining power of the statistic result to be increased showing as the higher accuracy of new data is going to represent a turning point for the enhancement of our capacity of testing our cosmological models.

4.2 Conclusions

Several anomalous features have been observed in the Cosmic Microwave Background (CMB) at large angular scales, both by the WMAP and the Planck satellites. Among those features there is a lack of correlation on the

largest angular scales, an alignment of quadrupole and octupole, a hemispherical power asymmetry and an even/odd parity asymmetry, with a preference for odd parity modes, and a cold spot in the southern hemisphere. All these features are individually observed as 2-3 σ anomalies, when testing the gaussian Lambda Cold Dark Matter (ΛCDM) hypothesis. Moreover it is proved that they are uncorrelated and this increases their statistical significance. As a matter of fact, we still lack a clear understanding of these large-scale features and the debate on their impact on our standard cosmological scenario is still open. One of the main assumptions of the inflationary ΛCDM model is the statistical isotropy of the universe. A good place to test statistical isotropy is at large angular scales in the CMB, because there we should find almost only primordial effects. It is exactly on these scales that we observe an anomalous behaviour of data compared to our expectations in ΛCDM. This work is focused on one of these anomalies, namely the observed lack of 2-point correlation on large angular scales($\sim 60°$) i.e. a low observed magnitude of the two point angular correlation function. When this anomaly has been detected in WMAP, several statistical estimators were proposed to analyze it. These quantities however make an assessment of the statistical significance of the effect, which is problematic, because they are defined a posteriori. Like the others, this anomaly may point to the need for modifications of the standard model of cosmology or may indicate that our Universe is a rare statistical fluctuation within that model. To investigate this problem, we need a new observable, correlated with CMB temperature: the correlation allows us to predict statistically its behaviour, starting from observed temperature anisotropies. In other words, if we assume that CMB temperature anomalies are a ΛCDM 'fluke', we can then build a priori statistics to test this hypothesis in the correlated observable. In this work we suppose to be in a rare statistical fluctuation of a ΛCDM universe. Since temperature and polarization of CMB photons are correlated, an anomalous small temperature auto-correlation should imply an anomalous small temperature-polarization cross-correlation. The prediction on temperature polarization correlation behaviour allows us to build an a priori estimator of this observable. We calculated the values of the estimator on two ensemble of simulations of universe: the first is generated starting from the observed power spectrum and they are called constrained realizations because they are forced to have the properties of the correlation that are observed while the second is generated starting from the ΛCDM best fit power spectrum. We obtain the two distributions for the values of the estimator in the two cases. Now we can say that all the simulations of ΛCDM universe that present a value of the estimator larger than a chosen confidence level, let's say 3σ, with respect to the distribution of constrained simulations aren't allowed by the

predictions we can make starting from the observed power spectrum and in those cases the hypothesis that our universe is a rare fluctuation of ΛCDM is excluded. We repeated the procedure starting from the WMAP 9 year and Planck power spectrum. We focused on the effect of masking the CMB sky on this procedure. We compared two methods: the simple division of the power spectrum extracted from the masked map for the fraction of the sky unmasked and the use of the program Master. Master is a library which is able to correct the pseudo-cl obtained from partial maps taking also into account the correlation among different l induced by the masking process. We showed that the analysis performed in this work requires the use of Master because the simple correction for f_{sky} isn't enough reliable. We also showed that the choice of the angles has remarkable impact on the shape of the estimator distribution. The constraining power of the statistic in our case is far less than that obtained by the authors in [12]. This is due to the initial number of simulations which is far smaller in our case, due to computational limitations. Nevertheless the comparison between the results obtained starting from the WMAP power spectrum and the Planck power spectrum don't show a remarkable increase of the constraining power of the statistic. A big difference is instead seen if we pass from a idealized situation to the one in which we take into account of the noise of the measurements in polarization. In our analysis we give the theoretical formula for the error bars that have to be associated to the value of the statistical estimator calculated on data. Planck data in polarization at large angular scales will soon be available. Once it will be possible we will calculate the value of the statistical estimator on Planck data and associate to it the error bar we found through the formula. We show that the value of the uncertainty strongly decrease from WMAP to Planck and consequently the constraining power of our statistical estimator is enhanced. This gives us the hope that Planck data in polarization, which are about to made public, will provide a definitive statement on the statistical relevance of this anomaly on our cosmological scenario.

The developments of this work can be several because the procedure that we explored is very flexible. Similar procedures can test the hypothesis that we live in a rare ΛCDM cosmology through the use of other observables and also it can be exploited to test hypothesis different from the standard cosmological scenario. The more interesting observables that can be studied in future developments of this work are mainly those linked to the Large Scale Structure of Universe (LSS). We mention some tracers of LSS. The first possibility consists of other background radiations even if not in CMB wave band: two examples are the 21 centimeter emission [46]and the Cosmic Infrared Background [27]. They are present until redshift of a few and on

very large scales (that is what we need to study the impact on large scale anomalies on the statistical isotropy assumption). Another possibility is the distribution of galaxies itself. In the future, a combination of the Dark Energy Survey [52], Dark Energy Spectroscopic Instrument [31], Euclid [30], Large Synoptic Survey Telescope [33] and Wide-Field Infrared Survey Telescope [50] will map out the galaxy distribution over the whole sky out to redshift beyond one, extending the data sets of the previous mission (such as the Sloan Digital Sky Survey). Other tracers, such as quasars and radio galaxies, are particularly useful since they are at redshifts of a few and probe an even larger volume. Regarding the possibility to test hypothesis other from the standard scenario we refer to the attempts to propose models that can explain at least in part the presence of anomalies in CMB sky. We can mention the model proposed in [19] of a dipolar modulation model that can explain the hemispherical asymmetry and a quadrupolar modulation model that can explain the quadrupole-octopole alignment or the work in [32] that try to explain the observed hemispherical power asymmetry as the result of non Gaussian primordial perturbations. These models must predict the behaviour of all the observables correlated with the temperature of CMB photons allowing us to test them with procedure similar to that explored in this work.

Ringraziamenti

Un sentito ringraziamento a Michele, Nicola e Sabino, per la disponibilità che mi hanno mostrato in questi mesi. Per avermi spinto a migliorare il mio lavoro e per avermi trasmesso l'entusiasmo per questa materia stupenda che è la Cosmologia. Grazie di cuore anche a Filippo, per avermi supportato con grande pazienza nell'affrontare tutte le inevitabili difficoltà che si incontrano quando si cerca di imparare qualcosa.

Ai miei genitori e alle mie sorelle, teneri opliti della nostra piccola falange. Ovunque io sia so che il vostro scudo mi protegge dal ginocchio alla spalla e la solida certezza del vostro affetto mi permette di affrontare con serenità i momenti più duri.

Ai miei amici astronomi, che hanno reso Padova una seconda casa. Grazie di tutti i momenti passati assieme, facendoci forza per affrontare le difficoltà che questi anni ci hanno riservato. In particolare ad Arianna, per la complicità, le risate e i pianti assieme. Per il sostegno di questi mesi: questo risultato è anche tuo, grazie di essermi stata vicina.

Ai miei compagni e alla mie compagne. Per avermi insegnato che l'unica parte che salviamo di noi è quella che diamo agli altri. Per avermi dimostrato che le persone possono fare delle cose bellissime se si dà loro fiducia. Perchè è impegnarsi per un mondo più giusto che ti dà uno scopo ed è farlo assieme che ti dà delle radici. Adelante.

Bibliography

[1] Ackerman, L., Carroll, S. M., and Wise, M. B. (2007). Imprints of a primordial preferred direction on the microwave background. *prd*, 75(8):083502.

[2] Aluri, P. K. and Jain, P. (2012). Parity asymmetry in the CMBR temperature power spectrum. *mnras*, 419:3378–3392.

[3] Aurich, R., Janzer, H. S., Lustig, S., and Steiner, F. (2008). Do we live in a 'small universe'? *Classical and Quantum Gravity*, 25(12):125006.

[4] Aurich, R. and Lustig, S. (2013). A search for cosmic topology in the final WMAP data. *mnras*, 433:2517–2528.

[5] Aurich, R., Lustig, S., Steiner, F., and Then, H. (2004). Hyperbolic universes with a horned topology and the cosmic microwave background anisotropy. *Classical and Quantum Gravity*, 21:4901–4925.

[6] Bennett, C. L., Halpern, M., Hinshaw, G., Jarosik, N., Kogut, A., Limon, M., Meyer, S. S., Page, L., Spergel, D. N., Tucker, G. S., Wollack, E., Wright, E. L., Barnes, C., Greason, M. R., Hill, R. S., Komatsu, E., Nolta, M. R., Odegard, N., Peiris, H. V., Verde, L., and Weiland, J. L. (2003). First-Year Wilkinson Microwave Anisotropy Probe (WMAP) Observations: Preliminary Maps and Basic Results. *apjs*, 148:1–27.

[7] Bennett, C. L., Hill, R. S., Hinshaw, G., Larson, D., Smith, K. M., Dunkley, J., Gold, B., Halpern, M., Jarosik, N., Kogut, A., Komatsu, E., Limon, M., Meyer, S. S., Nolta, M. R., Odegard, N., Page, L., Spergel, D. N., Tucker, G. S., Weiland, J. L., Wollack, E., and Wright, E. L. (2011). Seven-year Wilkinson Microwave Anisotropy Probe (WMAP) Observations: Are There Cosmic Microwave Background Anomalies? *apjs*, 192:17.

[8] Bennett, C. L., Larson, D., Weiland, J. L., Jarosik, N., Hinshaw, G., Odegard, N., Smith, K. M., Hill, R. S., Gold, B., Halpern, M., Komatsu, E., Nolta, M. R., Page, L., Spergel, D. N., Wollack, E., Dunkley, J., Kogut,

A., Limon, M., Meyer, S. S., Tucker, G. S., and Wright, E. L. (2013). Nine-year Wilkinson Microwave Anisotropy Probe (WMAP) Observations: Final Maps and Results. *apjs*, 208:20.

[9] Boyanovsky, D., de Vega, H. J., and Sanchez, N. G. (2006a). CMB quadrupole suppression. I. Initial conditions of inflationary perturbations. *prd*, 74(12):123006.

[10] Boyanovsky, D., de Vega, H. J., and Sanchez, N. G. (2006b). CMB quadrupole suppression. II. The early fast roll stage. *prd*, 74(12):123007.

[11] Copi, C. J., Huterer, D., Schwarz, D. J., and Starkman, G. D. (2009). No large-angle correlations on the non-Galactic microwave sky. *mnras*, 399:295–303.

[12] Copi, C. J., Huterer, D., Schwarz, D. J., and Starkman, G. D. (2013). Large-angle cosmic microwave background suppression and polarization predictions. *mnras*, 434:3590–3596.

[13] Cruz, M., Tucci, M., Martínez-González, E., and Vielva, P. (2006). The non-Gaussian cold spot in WilkinsonMicrowaveAnisotropyProbe: significance, morphology and foreground contribution. *mnras*, 369:57–67.

[14] Dikarev, V., Preuss, O., Solanki, S., Krüger, H., and Krivov, A. (2009). The Local Dust Foregrounds in the Microwave Sky. I. Thermal Emission Spectra. *apj*, 705:670–682.

[15] Dodelson, S. (2003). *Modern cosmology*.

[16] Dupé, F.-X., Rassat, A., Starck, J.-L., and Fadili, M. J. (2011). Measuring the integrated Sachs-Wolfe effect. *aap*, 534:A51.

[17] Eriksen, H. K., Hansen, F. K., Banday, A. J., Górski, K. M., and Lilje, P. B. (2004). Asymmetries in the Cosmic Microwave Background Anisotropy Field. *apj*, 605:14–20.

[18] Francis, C. L. and Peacock, J. A. (2010). An estimate of the local integrated Sachs-Wolfe signal and its impact on cosmic microwave background anomalies. *mnras*, 406:14–21.

[19] Gordon, C., Hu, W., Huterer, D., and Crawford, T. (2005). Spontaneous isotropy breaking: A mechanism for CMB multipole alignments. *prd*, 72(10):103002.

[20] Górski, K. M., Hivon, E., Banday, A. J., Wandelt, B. D., Hansen, F. K., Reinecke, M., and Bartelmann, M. (2005). HEALPix: A Framework for High-Resolution Discretization and Fast Analysis of Data Distributed on the Sphere. *apj*, 622:759–771.

[21] Granett, B. R., Neyrinck, M. C., and Szapudi, I. (2008). An Imprint of Superstructures on the Microwave Background due to the Integrated Sachs-Wolfe Effect. *apjl*, 683:L99.

[22] Guth, A. H. (1981). Inflationary universe: A possible solution to the horizon and flatness problems. *prd*, 23:347–356.

[23] Hansen, M., Kim, J., Frejsel, A. M., Ramazanov, S., Naselsky, P., Zhao, W., and Burigana, C. (2012). Can residuals of the solar system foreground explain low multipole anomalies of the CMB? *jcap*, 10:059.

[24] Higham, N. J. (2009). Cholesky Factorization. 1.

[25] Hu, W. and Dodelson, S. (2002). Cosmic Microwave Background Anisotropies. *araa*, 40:171–216.

[26] Huterer, D., Komatsu, E., and Shandera, S. (2010). Testing the Gaussianity and Statistical Isotropy of the Universe. *Advances in Astronomy*, 2010:697147.

[27] Ilić, S., Douspis, M., Langer, M., Pénin, A., and Lagache, G. (2011). Cross-correlation between the cosmic microwave and infrared backgrounds for integrated Sachs-Wolfe detection. *mnras*, 416:2688–2696.

[28] Kamionkowski, M. and Knox, L. (2003). Aspects of the cosmic microwave background dipole. *prd*, 67(6):063001.

[29] Komatsu, E., Dunkley, J., Nolta, M. R., Bennett, C. L., Gold, B., Hinshaw, G., Jarosik, N., Larson, D., Limon, M., Page, L., Spergel, D. N., Halpern, M., Hill, R. S., Kogut, A., Meyer, S. S., Tucker, G. S., Weiland, J. L., Wollack, E., and Wright, E. L. (2009). Five-Year Wilkinson Microwave Anisotropy Probe Observations: Cosmological Interpretation. *apjs*, 180:330–376.

[30] Laureijs, R., Gondoin, P., Duvet, L., Saavedra Criado, G., Hoar, J., Amiaux, J., Auguères, J.-L., Cole, R., Cropper, M., Ealet, A., Ferruit, P., Escudero Sanz, I., Jahnke, K., Kohley, R., Maciaszek, T., Mellier, Y., Oosterbroek, T., Pasian, F., Sauvage, M., Scaramella, R., Sirianni, M., and Valenziano, L. (2012). Euclid: ESA's mission to map the geometry of

the dark universe. In *Space Telescopes and Instrumentation 2012: Optical, Infrared, and Millimeter Wave*, volume 8442 of *procspie*, page 84420T.

[31] Levi, M., Bebek, C., Beers, T., Blum, R., Cahn, R., Eisenstein, D., Flaugher, B., Honscheid, K., Kron, R., Lahav, O., McDonald, P., Roe, N., Schlegel, D., and representing the DESI collaboration (2013). The DESI Experiment, a whitepaper for Snowmass 2013. *ArXiv e-prints*.

[32] LoVerde, M., Nelson, E., and Shandera, S. (2013). Non-gaussian mode coupling and the statistical cosmological principle. *jcap*, 6:024.

[33] LSST Science Collaboration, Abell, P. A., Allison, J., Anderson, S. F., Andrew, J. R., Angel, J. R. P., Armus, L., Arnett, D., Asztalos, S. J., Axelrod, T. S., and et al. (2009). LSST Science Book, Version 2.0. *ArXiv e-prints*.

[34] Mukhanov, V. F. and Chibisov, G. V. (1981). Quantum fluctuations and a nonsingular universe. *ZhETF Pisma Redaktsiiu*, 33:549–553.

[35] Nelson, E. and Shandera, S. (2013). Statistical Naturalness and Non-Gaussianity in a Finite Universe. *Physical Review Letters*, 110(13):131301.

[36] Peiris, H. V., Komatsu, E., Verde, L., Spergel, D. N., Bennett, C. L., Halpern, M., Hinshaw, G., Jarosik, N., Kogut, A., Limon, M., Meyer, S. S., Page, L., Tucker, G. S., Wollack, E., and Wright, E. L. (2003). First-Year Wilkinson Microwave Anisotropy Probe (WMAP) Observations: Implications For Inflation. *apjs*, 148:213–231.

[37] Peiris, H. V. and Smith, T. L. (2010). CMB isotropy anomalies and the local kinetic Sunyaev-Zel'dovich effect. *prd*, 81(12):123517.

[38] Penzias, A. A. and Wilson, R. W. (1965). A Measurement of Excess Antenna Temperature at 4080 Mc/s. *apj*, 142:419–421.

[39] Planck Collaboration, Ade, P. A. R., Aghanim, N., Akrami, Y., Aluri, P. K., Arnaud, M., Ashdown, M., Aumont, J., Baccigalupi, C., Banday, A. J., and et al. (2016a). Planck 2015 results. XVI. Isotropy and statistics of the CMB. *aap*, 594:A16.

[40] Planck Collaboration, Ade, P. A. R., Aghanim, N., Alves, M. I. R., Arnaud, M., Ashdown, M., Aumont, J., Baccigalupi, C., Banday, A. J., Barreiro, R. B., and et al. (2016b). Planck 2015 results. XXV. Diffuse low-frequency Galactic foregrounds. *aap*, 594:A25.

[41] Planck Collaboration, Ade, P. A. R., Aghanim, N., Arnaud, M., Arroja, F., Ashdown, M., Aumont, J., Baccigalupi, C., Ballardini, M., Banday, A. J., and et al. (2016c). Planck 2015 results. XVII. Constraints on primordial non-Gaussianity. *aap*, 594:A17.

[42] Planck Collaboration, Ade, P. A. R., Aghanim, N., Arnaud, M., Ashdown, M., Aumont, J., Baccigalupi, C., Banday, A. J., Barreiro, R. B., Bartlett, J. G., and et al. (2016d). Planck 2015 results. XIII. Cosmological parameters. *aap*, 594:A13.

[43] Powell, B. A. and Kinney, W. H. (2007). Pre-inflationary vacuum in the cosmic microwave background. *prd*, 76(6):063512.

[44] Rakić, A. and Schwarz, D. J. (2007). Correlating anomalies of the microwave sky. *prd*, 75(10):103002.

[45] Sarkar, D., Huterer, D., Copi, C. J., Starkman, G. D., and Schwarz, D. J. (2011). Missing power vs low-ell alignments in the cosmic microwave background: No correlation in the standard cosmological model. *Astroparticle Physics*, 34:591–594.

[46] Schwarz, D. J., Bacon, D., Chen, S., Clarkson, C., Huterer, D., Kunz, M., Maartens, R., Raccanelli, A., Rubart, M., and Starck, J. L. (2015). Testing foundations of modern cosmology with SKA all-sky surveys. *Advancing Astrophysics with the Square Kilometre Array (AASKA14)*, page 32.

[47] Schwarz, D. J., Copi, C. J., Huterer, D., and Starkman, G. D. (2016). CMB anomalies after Planck. *Classical and Quantum Gravity*, 33(18):184001.

[48] Schwarz, D. J., Starkman, G. D., Huterer, D., and Copi, C. J. (2004). Is the Low-ell Microwave Background Cosmic? *Physical Review Letters*, 93(22):221301.

[49] Smoot, G. F., Bennett, C. L., Kogut, A., Wright, E. L., Aymon, J., Boggess, N. W., Cheng, E. S., de Amici, G., Gulkis, S., Hauser, M. G., Hinshaw, G., Jackson, P. D., Janssen, M., Kaita, E., Kelsall, T., Keegstra, P., Lineweaver, C., Loewenstein, K., Lubin, P., Mather, J., Meyer, S. S., Moseley, S. H., Murdock, T., Rokke, L., Silverberg, R. F., Tenorio, L., Weiss, R., and Wilkinson, D. T. (1992). Structure in the COBE differential microwave radiometer first-year maps. *apjl*, 396:L1–L5.

[50] Spergel, D., Gehrels, N., Baltay, C., Bennett, D., Breckinridge, J., Donahue, M., Dressler, A., Gaudi, B. S., Greene, T., Guyon, O., Hirata, C., Kalirai, J., Kasdin, N. J., Macintosh, B., Moos, W., Perlmutter, S., Postman, M., Rauscher, B., Rhodes, J., Wang, Y., Weinberg, D., Benford, D., Hudson, M., Jeong, W.-S., Mellier, Y., Traub, W., Yamada, T., Capak, P., Colbert, J., Masters, D., Penny, M., Savransky, D., Stern, D., Zimmerman, N., Barry, R., Bartusek, L., Carpenter, K., Cheng, E., Content, D., Dekens, F., Demers, R., Grady, K., Jackson, C., Kuan, G., Kruk, J., Melton, M., Nemati, B., Parvin, B., Poberezhskiy, I., Peddie, C., Ruffa, J., Wallace, J. K., Whipple, A., Wollack, E., and Zhao, F. (2015). Wide-Field InfrarRed Survey Telescope-Astrophysics Focused Telescope Assets WFIRST-AFTA 2015 Report. *ArXiv e-prints*.

[51] Starobinsky, A. A. (1980). A new type of isotropic cosmological models without singularity. *Physics Letters B*, 91:99–102.

[52] The Dark Energy Survey Collaboration (2005). The Dark Energy Survey. *ArXiv Astrophysics e-prints*.

[53] Wandelt, B. D., Hivon, E., and Górski, K. M. (2001). Cosmic microwave background anisotropy power spectrum statistics for high precision cosmology. *prd*, 64(8):083003.